UNIVERSITÀ
DEGLI STUDI
DI PADOVA

Sede Amministrativa: Università degli Studi di Padova

Dipartimento di Principi e Impianti di Ingegneria Chimica “I. Sorgato”

SCUOLA DI DOTTORATO DI RICERCA IN INGEGNERIA INDUSTRIALE
INDIRIZZO: INGEGNERIA CHIMICA
CICLO XXIII

MULTISCALE MODELING OF THREE-DIMENSIONAL CELL CULTURES FOR TYPE 2 DIABETES STUDIES

Direttore della Scuola: Ch.mo Prof. Paolo Bariani
Coordinatore d’indirizzo: Ch.mo Prof. Alberto Bertucco
Supervisore: Dr. Nicola Elvassore

Dottorando: Enrico Magrofuoco

To my parents

Sommario

Le forti necessità legate allo sviluppo di farmaci e terapie per malattie quali il diabete di tipo 2, hanno portato alla crescente domanda di nuove tecnologie e protocolli. Modelli *in vitro* sono estremamente utili per studi fisiologici e screening farmacologici; tuttavia questi sono dispendiosi e richiedono molto tempo.

Un approccio teorico attraverso la modellazione matematica può facilitare lo studio della biologia del sistema e aiutare nella razionalizzazione degli esperimenti.

Lo scopo di questa tesi è stato lo sviluppo di un approccio multi-scala e multi-disciplinare per modellare colture tridimensionali cellulari e di tessuto.

L'applicazione finale ha previsto la razionalizzazione di un modello *ex vivo* di tessuto adiposo umano con lo scopo di caratterizzare le condizioni fisiopatologiche del diabete di tipo 2.

Modelli matematici sono stati sviluppati per descrivere colture cellulari in sistemi dinamici, al fine di analizzare l'effetto di variabili macroscopiche sulle proprietà del micro-ambiente e quindi sull'evoluzione cellulare.

Abbiamo investigato il ruolo delle condizioni sperimentali, come ad esempio la portata e la configurazione della camera di coltura, e testato l'efficienza di una gestione discontinua delle colture cellulari in piattaforme microfluidiche.

Inoltre, nel caso di un bioreattore a perfusione per colture cellulari tridimensionali, abbiamo studiato l'effetto di condizioni di coltura eterogenee nel micro-ambiente cellulare (a causa dello *scaffold* poroso) sulla crescita cellulare. Il modello relaziona le variabili macroscopiche alle proprietà del micro-ambiente cellulare predicendo la crescita in funzione delle condizioni sperimentali e della distribuzione della dimensione dei pori dello *scaffold*.

In aggiunta è stato analizzato l'effetto di fattori endogeni ed esogeni sui processi intra-cellulari. In particolare, abbiamo integrato il modello di trasporto di materia con il modello per il *signaling* dell'insulina, studiando l'influenza di questo ormone sul consumo cellulare di glucosio.

Infine, è stato proposto un modello matematico per descrivere la coltura *ex vivo* di tessuto adiposo umano in una piattaforma microfluidica per assistere nella fase di progettazione e realizzazione della piattaforma stessa. Questo sistema è stato utilizzato per studiare la risposta del tessuto sottoposto ad uno stimolo di insulina e le condizioni fisiopatologiche del diabete di tipo 2.

Questi risultati hanno interessanti risvolti applicativi per la progettazione di esperimenti e l'ottimizzazione delle condizioni di coltura, segnando un passo in avanti verso lo sviluppo di terapie e tests farmacologici.

Summary

The pressing needs related to the processes of drug and therapy development for diseases such as type 2 diabetes, have increased the demand for new technologies and protocols. *In vitro* models are extremely helpful for physiological and drug screening studies; however they are time consuming and expensive.

A theoretical approach through mathematical modeling could help in the understanding of the biology of the system and to rationalize these experiments.

The aim of this thesis has been the development of a multiscale and multidisciplinary approach to model three-dimensional cell and tissue culture.

The final application was the rationalization of an *ex vivo* model of human adipose tissue to characterize the pathophysiological conditions of type 2 diabetes mellitus.

Mathematical models were developed for describing cell culture in dynamic systems, aiming to analyze the effect of macroscopic variables on cell microenvironment properties and therefore on their fate.

We investigated the role of experimental conditions like the flow rate and the culture chamber configuration on cell proliferation, and we tested the efficiency of a discontinuous management of cell cultures in a microfluidic chip.

In addition, in a three-dimensional perfusion bioreactor, we studied the effect of heterogeneous culture conditions (within porous scaffolds) in the cell microenvironment on the cell growth. The model linked the macroscopic variables to the cell microenvironment properties predicting

cell growth as a function of the experimental conditions and the scaffold pore size distribution.

The effect of endogenous and exogenous factors on the intracellular processes was also investigated. In particular, we coupled the mass transport model to the insulin signaling pathways model, studying the influence of this hormone on the cell glucose metabolism.

We finally proposed a mathematical model for the *ex vivo* human adipose tissue culture in a microfluidic platform, supporting the design and realization of the device itself. This system has been used for studying the tissue response to an insulin stimulation and the pathophysiological conditions of type 2 diabetes.

These results show interesting applications for the experimental design and optimization of culture conditions, and they mark a step towards an efficient development of drug tests or therapies.

Foreword

The work of this PhD program was performed at "Dipartimento di Principi e Impianti di Ingegneria Chimica "I. Sorgato"" of Università degli Studi di Padova. Part of the computational section was carried out at the Department of Chemical Engineering of University of California, Santa Barbara (UCSB), under the supervision of Prof. F. J. Doyle III.

I would like to thank my supervisor, Prof. N. Elvassore, for giving me this chance and for his support in these years, and Prof. F. J. Doyle III for the great opportunity of working with his group at UCSB.

During this PhD program the following publications have been produced:

1. A Carraro, M Flaibani, U Cillo, L Michelotto, E Magrofuoco, M Buggio, G Abatangelo, R Cortivo, MB Herrera, C Tetta, N Elvassore, B Zavan. "A Combining Method to Enhance the *In Vitro* Differentiation of Hepatic Precursor Cells". Tissue Engineering: Part C. 2010, 16(6), 1543–1551.
2. M Flaibani, E Magrofuoco, N Elvassore. "Computational modeling of cell growth heterogeneity in a perfused 3D scaffold". Industrial & Engineering Chemistry Research. 2010, 49(2), 859–869.
3. E Magrofuoco, FJ Doyle, III, N Elvassore. "Theoretical analysis of insulin dependence glucose uptake heterogeneity in a 3D dynamic cell culture". To be submitted to Biotechnology & Bioengineering.
4. E Magrofuoco, L Prevedello, N Elvassore. "Optimal feeding strategy for cell culture in microfluidic platform". To be submitted to Biomedical Microdevices.

5. E Magrofuoco, M Flaibani, N Elvassore. “Modeling and experimental validation of cell growth heterogeneity in a perfused three-dimensional scaffold”. In writing.

Part of the work in this thesis was presented at international conferences during the PhD program, including: Biomedical Engineering Society (BMES), European Association for the Study of Diabetes (EASD).

Contents

1

Introduction

After introducing the basic concepts of the tissue engineering, this chapter will introduce the multiscale aspects of biology, and the mathematical models for the cell cultures will be reviewed. The clinical relevance and motivations for applying the modeling approach to type 2 diabetes study will be presented, at last the outline of this thesis is reported.

1.1 Tissue engineering

Tissue engineering has been defined as “an interdisciplinary field that applies the principles of engineering and the life sciences toward the development of biological substitutes that restore, maintain, or improve tissue function” [1].

The aim of the tissue engineering is to provide organ replacement, moreover it could be helpful in the process of the development of new drugs through the generation of *in vitro* model of tissue and organ [2]. Indeed tissue engineering plays a fundamental role for designing *in vitro* physiological models to study disease pathogenesis and for developing molecular therapeutics [2].

In all these applications, the requirements are to supply the cells with the appropriate cues, to control the conditions in the cell microenvironment, and to monitor cellular responses on multiple hierarchical levels [3].

The successful large–scale production of engineered tissue requires:

- a cell source;
- a scaffold;
- a bioreactor to mimic the *in vivo* environment.

The cell source is an important issue; it must be chosen based on the aim of the culture, taking into account ethical and safety issues, and efficiency.

Scaffolds are porous and degradable structures made from either natural materials (collagen, fibrin) or synthetic polymers (polylactide, polyglycolide). These three-dimensional structures are used to support cells during the culture and potentially for releasing of growth factors. Scaffold are necessary to overcome the constraint on the size of tissue engineered *in vitro*, that is the short distance over which oxygen can diffuse before being consumed (a few hundred micrometers) [4, 5].

Bioreactors are used to recreate the *in vivo* cell microenvironment conditions in order to provide the physical, mechanical, chemical, biological cues to guide cell differentiation or proliferation. The 3D cell structure obtained from these devices are results of cell–cell and cell–microenvironment interactions. A theoretical multiscale approaches, such as mathematical models [6], are essential tools for studying and for rationalizing the three-dimensional cell cultures.

1.2 Multiscale modeling of biological systems

Living organisms are organized in multiple, interrelated scales and no single scale can be considered in isolation from the others, they are influenced by information which moves both up and down through scales. The time scales range from seconds (i.e. cell signaling) to years (for organism development and life span), the spatial scales involved vary from nanometers (e.g. biomolecules) to meters (organisms).

Thanks to the advent of all new quantitative experimental technologies, in particular to the high-throughput "-omics" techniques (genomics, transcriptomics, proteomics, and metabolomics) the life sciences are becoming data rich and cover a wide range of length and time scales.

Biomedical and biological researches frequently involve experiments that link different scales of biological systems, for instance, the scales of intracellular molecular interactions to the scale of cellular behavior and beyond to the behavior of cell populations. Two examples of the multiscale modeling applications are the heart [7] and brain [8] research. Indeed modeling the heart means to describe quantities from the macroscopic scale such as blood flow, and active and passive changes in stress and strain, to the microscopic level, for instance chemical concentrations, and electric potentials.

The understanding of function and pathology of tissue requires modeling and coupling phenomena to link microscopic information to macroscale effects. Computational modeling aims to quantitatively explore such multiscale systems, simulations have to incorporate different modeling techniques because of the different time and space scales [9]. The "-omics" data can potentially be used to bridge between cellular and physiological states and fill the modeling gap between the microscopic and the macroscopic levels.

The development of in silico mathematical models has two main aims, understanding and prediction [10, 11]. When the fine details are not known, modeling is a tool for testing hypotheses, providing a mathematical representation of the experimentally observed phenomena; in this case, the modeling enhances understanding of the system. On the other hand, when biological details of a system are known, a mathematical model can be used in place of the biological system, making predictions about the results of virtual experiments. In this scenario the model does not add to our understanding, it simply replicates the system. This may be used to conduct experiments which are too difficult or costly to carry out directly guiding the experimental research.

The development of any integrated multiscale theoretical framework includes the selection of an appropriate modeling scale [11, 12]. This first step is usually guided by the experimental data available, in addition the sub–models, that compose the main framework, must be linked together. Furthermore the complexity of the model must be chosen, indeed the more detailed a model is, the more parameters are involved and thus the higher the computational cost of running the algorithm. It is clear that a compromise between the biological complexity to be represented and the computational resources is required.

1.3 State of the art of biological models

In this section we will review some of the mathematical models in literature which focus on the modeling of tissue growth within a dynamic culture environment.

The development of a mathematical model for describing the behavior of a cell population, it must be decided whether to formulate a model considering the interactions between single cells in the population (discrete models) or to consider such system as a continuum (continuum models). In addition, stochastic modeling in biological system have been extensively used, e.g. for understanding phenomena ranging from molecular-level fluctuations to cellular movement, or for introducing stochastic “noise” [13].

Discrete models are based on the interactions of individual cells in space and time and can easily incorporate biological phenomena. However, these models can study a relatively small numbers of cell system due to the high computational costs. Hence a typical discrete model is usually designed with a sub–millimeter or even lower domain size [14]. Simplest discrete models describe cells as point–wise objects and it has been applied for studying process like the cell signaling [15–19]. Other models have been used to describe cell–cell interactions [20] or for studying cell populations [21–23].

In contrast, continuum models describe system such as a whole tissue as a continuum domain rather than at the resolution of individual cells. These models are usually expressed in terms of a system of partial differential equations (PDEs).

Over the last years, several mathematical models have been developed for describing the cell growth in a dynamic culture environment, in particular on three-dimensional construct. Many studies have focused on the development of models to predict the steady state distribution of key nutrients (such as oxygen and glucose) inside bioartificial tissues [5, 24–29]. They are able to associate the mass transport and consumption of nutrients in tissues, however they cannot provide the dynamic process of tissue development inside biomaterial scaffolds.

Other authors have studied the mass transport of oxygen: in static conditions [30–33], rotating bioreactors [34–38], spinner flask bioreactors [27, 39], concentric cylinder bioreactors [24], a vascularising scaffold implanted *in vivo* [40], perfusion bioreactor [41–44]. These models are generally based on classical diffusion–convection equations, coupled with momentum transport equations if necessary.

The quantification of shear stress acting on tissue, especially cartilage, has been analyzed by several authors to model the hydrodynamic environment in a spinner flask bioreactor [45], in a wavy walled bioreactor [46] or within cultured porous implants [47, 48].

Biological phenomena, such as cell proliferation and/or tissue growth, have also been modeled based on the nutrient spatial distribution [34, 36, 40, 41, 49–52] and/or the mechanical loading [35, 53, 54].

1.4 Application of mathematical modeling to type 2 diabetes mellitus

In healthy individuals, glucose homeostasis control the blood sugar concentration. High glucose level triggers the secretion of insulin from the pancreas which increases the glucose uptake and reduces the glucose production from the liver. Low glucose concentration leads to glucagon release for enhancing the glucose production. Type 1 diabetes occurs when pancreatic cells are destroyed by the body's own immune system. In contrast, people with type 2 diabetes produce insulin, but the target cells (muscle and adipose) are insulin resistant, that is the insulin cannot raise the glucose uptake.

Type 2 diabetes constitutes about 85 to 95 % of all diabetes in developed countries, it means that the global number of people with this disease is about 246 million people in the age group 20-79 and the worldwide estimate is expected to increase to 380 million of the adult population by 2025. Compare to the other causes of death, the percentage of death attributed to diabetes is about 10 of the total. In addition type 2 diabetes is associated with several complications like:

- cardiovascular disease;
- nephropathy;
- neuropathy;

- amputation;
- retinopathy.

Because of its relevance, type 2 diabetes has become so important that the annual global health expenditure for diabetes in 2007 was estimated between USD 230 and 420 billion [55].

Although the prevention and early detection are the best ways for curing diseases, a widely applicable and cost-effective screening strategy is difficult to develop because of the marked differences between ethnic groups in the development of type 2 diabetes [56].

Nowadays there are many drugs which lower blood sugar concentration in different way and acting on various tissue, especially muscle and fat cells. Therefore it is crucial to perform selective drug screening to determine which is the best combination of drug for the specific patient.

An *in vitro* model could be an important step towards the treatment of the disease. To this end we applied the mathematical model for supporting the development of an *ex vivo* model for studying the pathophysiological condition of type 2 diabetes.

1.5 Thesis objectives and structure

The aim of this thesis is to rationalize three-dimensional cell and tissue culture for supporting the design of bioreactors and to interpret the biological outcomes; a multiscale and multidisciplinary approach was necessary to achieve such objective. Mathematical modeling was applied to develop *ex vivo* human adipose tissue culture for studying the pathophysiological condition of type 2 diabetes mellitus.

In chapter 2 the experimental approach to the dynamic cell culture is presented. *Ad hoc* analysis techniques and experiments were setup to collect physical and biophysical data.

In chapter 3 a theoretical study of cell niche properties, and its temporal evolution under perfusion in a microfluidc platform is described. The analysis considers the effect of operative parameters on the cell fate, in particular on the cell growth.

In chapter 4 the variability of a three-dimensional dynamic cell culture is considered. The system is analyzed by means of microscopic mathematical model to study the effect of extrinsic heterogeneities on the cell microenvironment properties and therefore on the cell growth.

In chapter 5 the influence of endogenous factors on the intracellular activities in a three-dimensional cell culture is presented. A rational understanding of a specific signaling cascade process is analyzed in order to coupled this phenomenon with the mass transport phenomena in a bioreactor system.

In chapter 6 all the theoretical and experimental developed skills have been coupled for supporting the design of a microfluidic platform for *ex vivo* human adipose tissue culture. The device has been applied for studying the pathophysiology of a metabolic disorder such as type 2 diabetes mellitus.

1.6 Thesis outline and experimental plan

Figure 1.1 shows the timeline of the PhD project schedule in these three years. The modeling of the biological systems developed during the three years has been coupled with an experimental approach to the dynamic cell culture to support and validate the theoretical analysis.

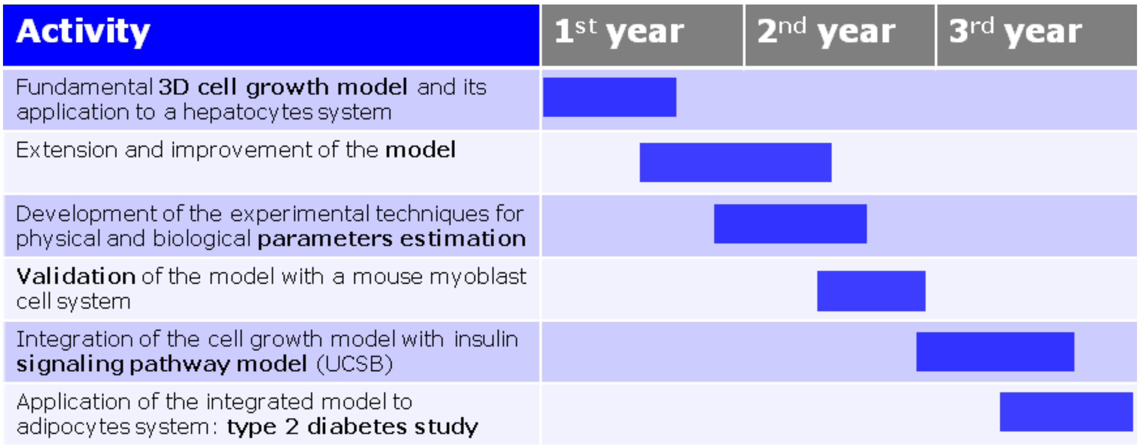

Figure 1.1: Time line of the PhD project schedule during the three years of program.

2

Experimental techniques

This chapter is aimed to describe the experimental and theoretical techniques used to determine the physical and biological parameters required for the mathematical models described in chapter 4. In particular, the evaluation of the glucose consumption rate of murine skeletal muscle cell line C2C12 and the porous scaffold morphology characterization will be presented.

2.1 Introduction

The behavior of a biological system is the result of the complex interactions of phenomena which occur at different spatial and time scale [10]. Integrating the biological information into models, mathematical tools have enhanced the understanding of life system [6, 57].

Having a model able to describe the response of a specific biological system such as a cell culture, requires biological and physical data. Indeed a cell culture system is defined by a kinetic (i.e. cell growth rate, specific oxygen consumption rate) and physical parameters (e.g. mass transport properties or 3D configuration). These values depend on the cell type, moreover, within each cell type the range of variation can cover several orders of magnitude [58].

Thus, it is clear that all the physical and biological parameters are essential to obtain a model for describing a cell culture system, and when these information are not available in literature, *ad hoc* experiments must be set up for their determination.

2.2 Bioreactors in tissue engineering

Tissue engineering aims to obtain tissue clinically valuable to be used as *in vitro* model for physiological studies and for generating of graft for transplantation in order to replace, repair, or facilitate the regeneration of damaged or diseased tissue. Engineered tissues are typically composed of cellular and non cellular components, with at least a few mm in size to serve as grafts for tissue replacement [59].

The *in vitro* formation of engineered tissue requires the 3D organization of cells via biomaterial scaffolds. A first generation of three-dimensional cell culture was the static loading of cells onto a scaffold, but several studies reported low seeding efficiencies [60–64] and non-uniform cell distribution within constructs [60, 61, 63, 65, 66].

In vivo, the blood capillaries network provides the nutrients to the cells, whereas *in vitro* static cell cultures are subjected to the diffusion mass transfer limitations [4, 5]. Because of this limitation, 3D cell culture must be coupled with a device that enhances the mass transport to and from the cells, bioreactors have been developed and applied to overcome such problem.

Bioreactors are generally defined “as devices in which biological and/or biochemical processes develop under closely monitored and tightly controlled environmental and operating conditions (e.g. pH, temperature, pressure, nutrient supply and waste removal)” [59]. The main objective in the design of a bioreactor is the achieving of a high cell density and uniformly distributed throughout the scaffold volume.

Therefore all bioreactors designed for tissue growth require a porous structure (scaffold) where cells are seeded and the enhancement of the mass transport. Usually it is considered mass transport limited relatively to oxygen [67, 68], but also the shear stress applied on the cells plays an important role on their fate [45, 46, 48]. In this section the most common bioreactors configurations used for tissue engineering applications [59, 69] will be presented:

- spinner-flask;
- rotating wall;

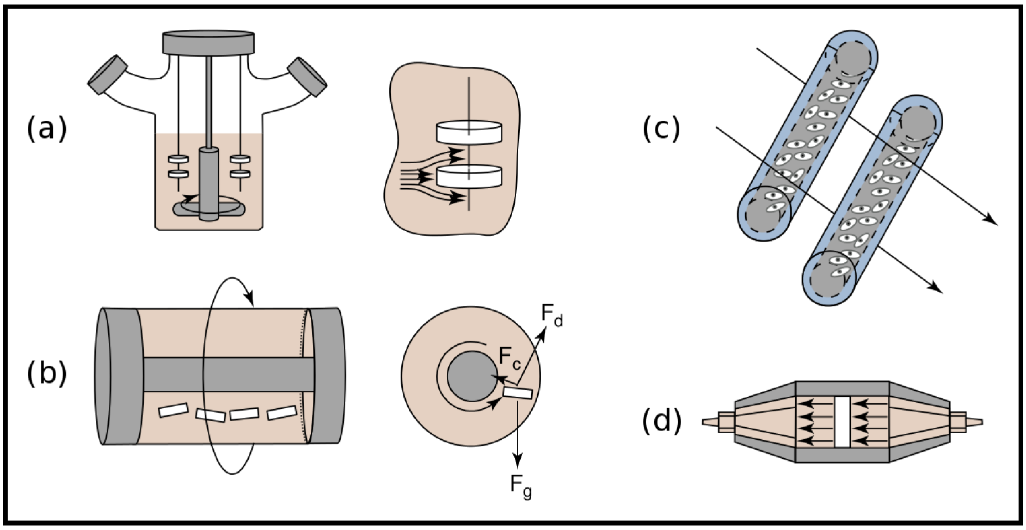

Figure 2.1: Representative bioreactors for tissue engineering applications. (a) Spinner-flask, (b) rotating-wall, (c) hollow fiber, (d) direct perfusion. Figure reprinted from Martin et al. [59]

- hollow fiber;
- direct perfusion.

The spinner-flask bioreactor (Fig. 2.1a) induces mixing of nutrients and oxygen in the cell media reducing the boundary layer at the construct surface [59], nonetheless it yields low seeding efficiencies [61, 70] and non-uniform distributions of cells [65], with a higher cell density at the scaffold surface [71].

Rotating wall vessel (Fig. 2.1b) [72–74] provides dynamic culture environment to the construct, with low shear stresses and high mass transfer rates, but the growth rate could be non-uniform [35]. Finally, it needs control systems to modify the rotation speed of the vessel in function of the tissue size for maintaining the growing tissue in a state of free-fall.

Hollow fiber bioreactor (Fig. 2.1c) mimics *in vivo* blood vessels, it increases the mass transport of nutrients and oxygen to the center of the growing tissue through a semi-permeable hollow fiber. This configuration could generates gradients of both nutrients and waste products resulting in a heterogeneous cell distribution [68].

In the direct perfusion bioreactor (Fig. 2.1d), medium flows through the pores of the scaffold. It can be used both for seeding [75] to have a high uniform cell distribution and for 3D cell culture [76–78]; medium flowing through the construct enhances mass transport at the periphery and also within the internal pores.

2.2.1 Murine skeletal muscle cell line C2C12

The mathematical model of a 3D cell growth in a perfusion bioreactor system (Fig. 2.2) developed in chapter 4 has a general form and it can be adapted to any type of cell once the biological parameters are known. We studied the murine skeletal muscle cell line C2C12. These cells were originally obtained by Yaffe and Saxel [79] through selective serial passage of myoblasts cultured from the thigh muscle of C3H mice 70 h after a crush injury. These cells were shown to be capable of differentiation in functional myotubes. C2C12 cells are a useful model to study the differentiation of myogenic cells to skeletal muscle cells and express muscle proteins and the androgen receptor (AR).

2.2.2 Three-dimensional perfusion bioreactor system

The perfusion bioreactor system for three-dimensional cell culture was designed and developed in our laboratory [76] (Fig. 2.2). It is composed of four units: a peristaltic pump, a gas exchanger, a medium reservoir, and eight independent culture

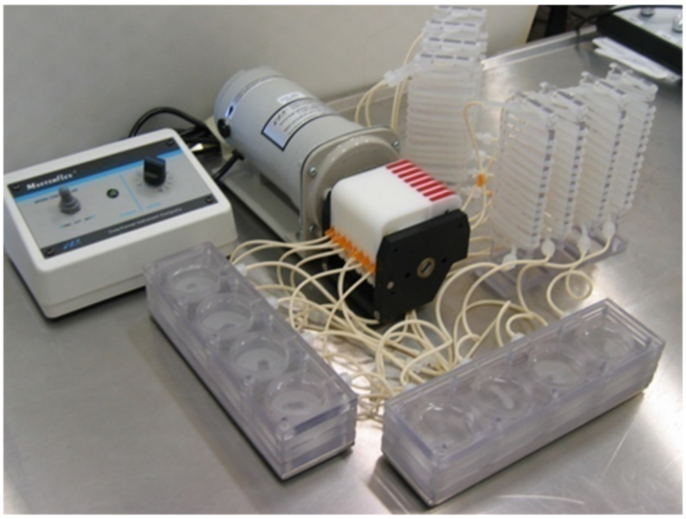

Figure 2.2: Perfusion bioreactor system composed of the peristaltic pump, the gas exchanger, and eight independent culture chambers.

chambers. The former is a volumetric pump that control the medium flow rate through the scaffold independently from the pressure drop. The gas exchanger is required to control the oxygen concentration and the pH, according to the carbon dioxide concentration in the medium. The medium reservoir provides all the nutrients and metabolites necessary for length of the experiment, it can be a separated unit or the hold-up volume of the bioreactor itself could be this reservoir. The scaffold used for the 3D cell culture is allocated in the culture chamber. In this three-dimensional configuration, cells are seeded onto the scaffold surface and the medium is constrained to flow through the construct. It is a porous materials with a defined porosity, pore size distribution, and tortuosity; usually these pores are interconnected to form channels with different size and length.

The bioreactor can work both in a closed configuration (with recirculation - Fig. 2.3A) and in a open one (without recirculation - Fig. 2.3B). Once the bioreactor is setup, in the closed configuration the scaffold is perfused by the same medium introduced into the system at the beginning of the experiment; by contrast, in the open configuration, fresh cell media continuously flows through the scaffold.

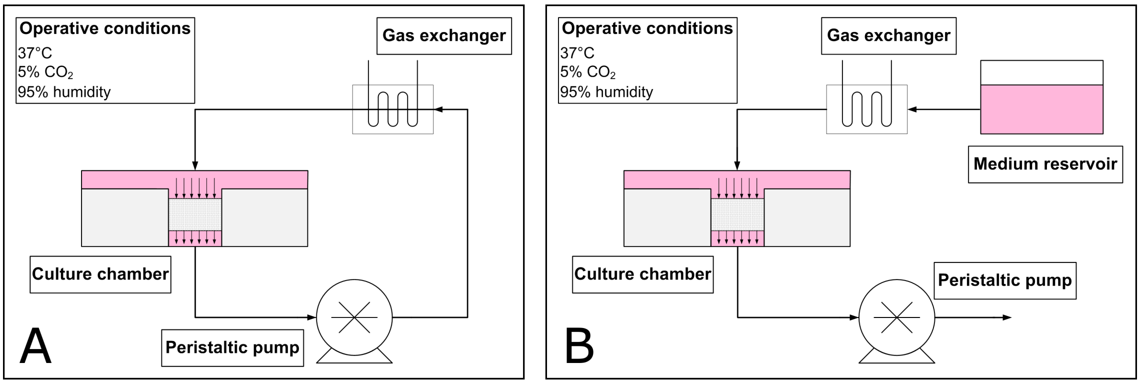

Figure 2.3: Scheme of a perfusion bioreactor. (A) Configuration with recirculation of cell media. (B) Configuration without recirculation of cell media.

2.3 Analysis of a three-dimensional porous collagen scaffold

All the cell culture experiments with the perfusion bioreactor were carried out using a collagen scaffold. To describe the cell growth in a porous material, all the scaffold properties must be known. Because in chapter 4 we are interested in describing the microscopical properties of a cell culture we determined the pores scaffold distribution sorting the equivalent diameter distribution.

2.3.1 Scaffold morphology

The scaffold morphology, i.e. the channel diameter distribution and the mean channel diameter, was determined by means of a fluorescence microscope (Leica CTR6000). The collagen construct is a cylinder with diameter and height of 5 and 3 mm, respectively, and it was immersed in a 0.1 g /L solution of fluorescein sodium salt for 10 hours to allow the molecule adsorption onto the collagen. After dyeing, the scaffold was embedded in OCT (Optimal Cutting Temperature) and immediately snap-frozen in liquid nitrogen. Cross sections of the frozen scaffold were cryosectioned at 20 µm thickness on a cryostat (Leica CM1950) at −22 °C and mounted on Superfrost Plus glass slides (Fig. 2.4A). Cross sections were analyzed using the fluorescence microscope in order to collect RGB images (Fig. 2.4B) of the scaffold.

2.3.1.1 Morphological scaffold processing and reconstruction

Since the images were subjected to noises due to the analysis process, it was impossible to obtain a scaffold image without discontinuities. Therefore the digitized fluorescent images were processed using the image toolbox of MATLAB (The Mathworks, Natick, MA). Images were enhanced to separate the scaffold from the background and the noise; each frame were subject to the following processes:

- brightness-contrast;
- basic global thresholding;

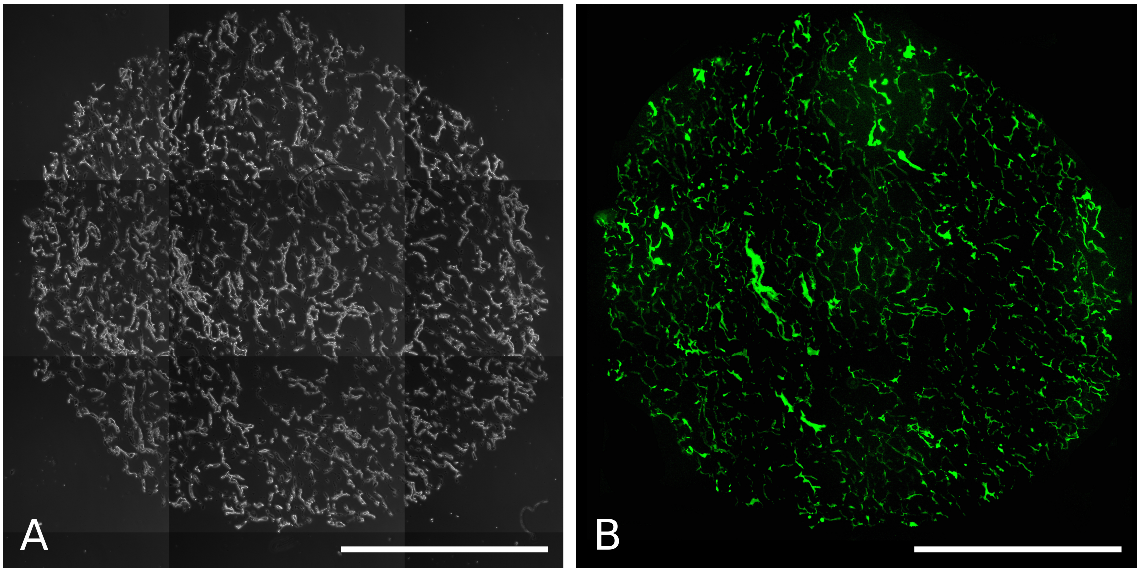

Figure 2.4: Cross sections of a collagen scaffold. (A) Phase contrast image. (B) Fluorescence image. Scale bars 2.5 mm.

- median filter;
- segmentation by morphological watershed.

The first two operations produce an indexed (black and white) image where the background is separated by the scaffold, nevertheless its morphology can be recognize only qualitatively. Hence images were processed with a median filter for removing the presence of *impulse noise*, also called *salt-and-pepper noise* because of its appearance as white and black dots superimposed on the image. Finally images were analyzed by means of segmentation by morphological watershed to quantitatively identify the frame of the scaffold (Fig. 2.5). At the end of the process, manual inspection was performed to find out all the scaffold discontinuities missed by the segmentation algorithm.

2.3.1.2 Channel distribution

After the scaffold reconstruction, each pore was identified and classified by the equivalent diameter, that is the diameter of a circle with the same area of the pore. A specific algorithm was developed and implemented in MATLAB to detect and analyze the scaffold morphology, obtaining the channel diameter distribution. After-

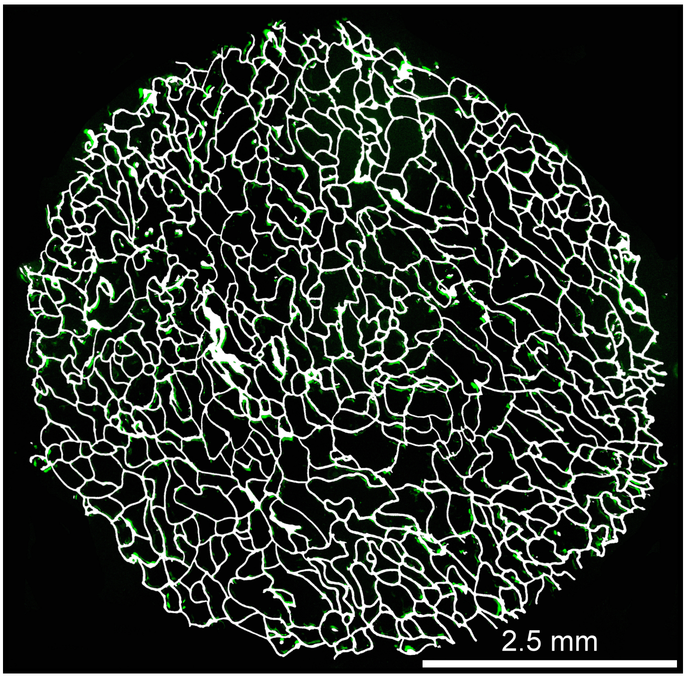

Figure 2.5: Merge of the fluorescence scaffold image (Fig. 2.4B) and scaffold reconstruction.

wards, it was fitted using the fitting toolbox of MATLAB obtaining an analytical expression of this distribution (Fig. 2.6). The Rayleigh distribution (Eq. (2.1)) was chosen as fitting function because it well describes the channel distribution and because of its simple expression defined by a single parameter, b:

$$f\left(x\right)=\frac{x}{b^2}\exp\left(-\frac{x^2}{2b^2}\right), \tag{2.1}$$

$$b=148.26\ \mu m.$$

The mean and variance of the Rayleigh distribution may be expressed as:

$$\mu\left(x\right)=b\sqrt{\frac{\pi}{2}}=185.82\ \mu m, \tag{2.2}$$

$$\sigma^2\left(x\right)=\frac{4-\pi}{2}b^2=9435\ \mu m^2. \tag{2.3}$$

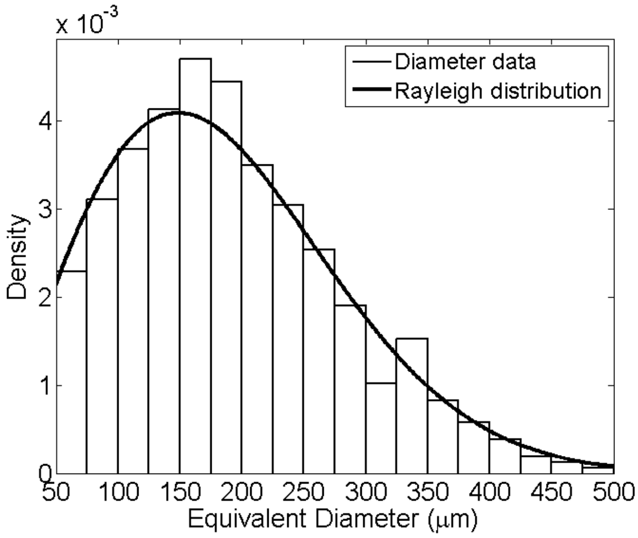

Figure 2.6: Channel equivalent diameter distribution obtained from image analysis and its fitting with the Rayleigh function.

2.3.2 Cell counting and distribution

The scaffold morphology technique previously described was applied for the cell growth distribution analysis as well. It has been a fundamental step in the model validation as explain in chapter 4.

After the cell culture in the perfusion bioreactor, the scaffold was treated as reported in section 2.3.1, but sections were cryosectioned at 15 µm thickness instead. After this process, cell nuclei were dyed with Hoechst 33342 in order to detect cells in each pore (Fig. 2.7). After the image acquisition the number of cells in each pore were determine to obtain their distribution in a single section. Three different areas were analyzed, the top, the middle and the bottom section of the scaffold in order to have a cell growth profile along its height.

2.4 Parameter estimation of cell culture

Besides the physical system properties, the mathematical model requires an expression for all the kinetics which describe the cell behavior, such as the oxygen and glucose consumption rate. The former can be found in the literature since it is a very important nutrient for the cell culture and it has been studied by various au-

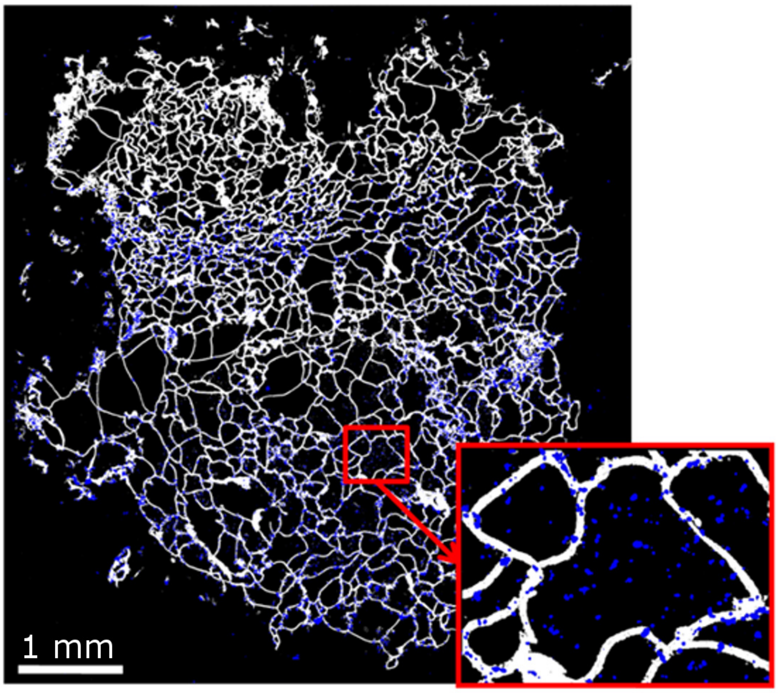

Figure 2.7: Middle cross section of scaffold with Hoechst staining, the magnification shows two pores with cells inside.

thors for different cell type [27, 28, 80]; nevertheless glucose has not been studied as well as oxygen, hence the glucose consumption rate expression for murine skeletal muscle cell line C2C12 must be experimentally determined.

2.4.1 Glucose measurement

The glucose consumption rate was determined by means of an indirect measurement, that is the average glucose concentration in the cell culture media. There are several methods to determine metabolites concentration in biological systems as reported in literature [81]. In particular two techniques were considered for this experiment:

- HPLC with evaporative light scattering detector (HPLC-ELSD);
- enzymatic glucose assay kit (BioVision, Inc.).

Both methods were tested to select the more suitable technique for this analysis, and the following features were evaluated:

- analysis time;
- number of metabolites measured;
- sensitivity;
- costs.

The HPLC system is time-consuming due to the operative conditions setup, sample pretreatment and analysis, on the other hand the enzymatic kit ensures easier and faster analysis. Nevertheless, liquid chromatography has a high sensitivity, in the vicinity of micromolar (up to femtomolar thanks to a liquid chromatography-mass spectrometry system), while the enzymatic kit has a sensitivity three order of magnitude greater than chromatography (millimolar); moreover the HPLC system has a high repeatability. For these reasons the glucose measurements were performed by means of the chromatography technique.

Glucose concentration in the medium was determined using HPLC system. It consists of a Jasco PU-1580 isocratic pump and Alltech 800 ELS detector. Separation was achieved at ambient temperature with an Alltech Prevail Carbohydrate ES, 5 µm, (4.6 mm × 250 mm) column preceded by Alltech Prevail Carbohydrate ES All-Guard cartridge to eliminate interferences. The mobile phase was a mixture of water and acetonitrile (25:75, v/v); it was filtered through a 0.22 µm filter and degassed by vacuum before using. Separation was carried out by isocratic solvent elution at a flow rate of 1 mL /min for 15 minutes analysis time. The external standard method was chosen to quantify the samples (Fig. 2.8). To avoid precipitation inside the HPLC, samples were pretreated before the analysis: the medium samples (20 µL) were diluted with acetonitrile, centrifuged and the supernatant was collected and filtered, solutions were stored at $-80\,°\mathrm{C}$.

2.4.2 Experimental setup

In order to fit the glucose kinetic parameters, a cell culture in a 2D system was conducted assuming that the glucose consumption rate is not affect by the cell system structure (2D or 3D).

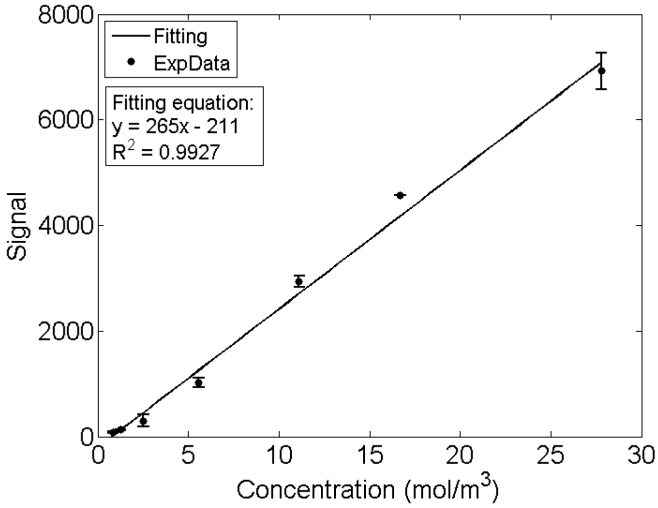

Figure 2.8: Calibration curve for glucose in cell culture media.

The C2C12 cells were grown in Dulbecco's modified Eagle medium supplemented with 10 % fetal bovine serum and 1 % penicillin-streptomycin solution (1000 U /mL) on standard 100 mm Petri Tissue Culture dishes. Cells were seeded with a density of about 760 cell /cm^2 and incubated for 12 h with 10 mL of medium. After the incubation the cell culture media was replaced by 12 mL of fresh media, this denotes the initial time of the experiment; cells were allowed to growth for 3 days. At each time point the medium was homogenized by mixing and a 500 µL sample was collected to determine the average glucose concentration.

2.4.3 Mathematical model

The glucose measurement as described in the previous section is the average value of the whole system, which is different from the local value at which the cells are exposed to. The characteristic time scale of the consumption, τ_{kin}, and diffusion, τ_D, must be considered; indeed if the ratio τ_{kin}/τ_D is less than 1, it means that there is a diffusion profile along the height of the medium which limits the glucose uptake (diffusion regime). Since we aimed to determine the local glucose consumption rate as a function of the glucose concentration in the cell microenvironment, a mathematical model was developed to describe 2D cell culture on a Petri dish in term of the metabolite profiles and cell growth.

In the system, glucose diffuses from the medium bulk to the cell surface where it is consumed, hence the transient diffusion-reaction equation was applied. Moreover the model takes into account the culture medium sampling, indeed each measurement:

- decreases the total medium volume at each time point;
- equalizes the medium glucose concentration.

In the governing equation, the reaction term was assumed to be a function of the cell growth rate and the specific uptake of glucose. The former was expressed with an exponential law because we were interested in describing the exponential growth. On the other hand, it was hypothesized a linear relationship between the specific uptake of glucose and the local glucose concentration.

2.4.3.1 Mass transport

For this system we assumed that all the mass transport phenomena occur only along the height of the Petri dish, therefore the one dimensional form of the equation of continuity for glucose was applied:

$$\frac{\partial c_G}{\partial t} = -\frac{\partial N_G}{\partial z}, \tag{2.4}$$

$$N_G = -D_G \frac{\partial c_G}{\partial z}. \tag{2.5}$$

Where c_G is the glucose concentration, t is the time, N_G is the diffusive flux expressed by the Fick's law (Eq. (2.5)) and D_G is the diffusion coefficient of the metabolite in medium at 37 °C. The boundary and initial conditions required for Eqs. (2.4) and (2.5) are:

$$\left.\frac{\partial c_G}{\partial z}\right|_{z=0} = 0, \qquad \left.N_G\right|_{z=L} = R_G, \tag{2.6}$$

$$c_G\left(z, t_{in}\right) = c_{G,0}. \tag{2.7}$$

The expressions in Eq. 2.6 show the insulation condition at the top of the medium surface and the molar flux at the bottom of the dish due to the cell uptake. The initial condition (Eq. 2.7) is a uniform glucose concentration. The glucose consumption rate, R_G, is expressed by the following equations:

$$R_G = \rho Q_G, \tag{2.8}$$

$$Q_G = k_1 + k_2 t, \tag{2.9}$$

$$\rho = \rho_0 \exp(\mu t) \,. \tag{2.10}$$

Where ρ is the cell density, Q_G is the glucose uptake, k_1 and k_2 are the fitting parameters and μ is the specific growth rate coefficient calculated by means of the doubling time.

2.4.3.2 Fitting and parameter estimation

In Eq. 2.9 the glucose uptake is a function of the time instead of the local glucose concentration in order to have a more generic expression for the kinetic. The system of equations (Eqs. 2.6 - 2.10) was solved fitting the experimental glucose data (Fig. 2.9) at every time point with the average glucose concentration profile calculated

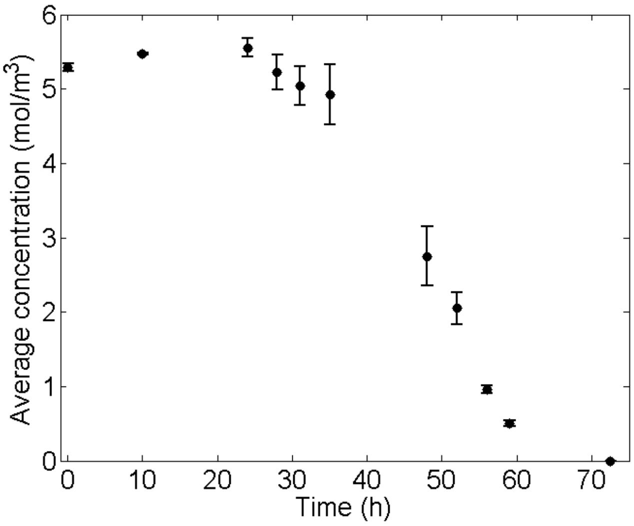

Figure 2.9: Temporal profile of the average glucose concentration with the standard deviation in a Petri dish culture system.

from the mathematical model with Eq. 2.11:

$$\langle c_G \rangle = \frac{\displaystyle\int_V c_G \, dV}{\displaystyle\int_V dV}. \tag{2.11}$$

To evaluate the glucose consumption rate, we considered the experimental points with a significant variation of the glucose concentration, that is during the exponential cell growth. The model adjusts the parameters of the glucose uptake expression (Eq. 2.9), fits the the experimental points (Fig. 2.10) minimizing the objective function (Eq. 2.12):

$$\varepsilon_{tot} = \sum_{i=1}^{n} \left(\frac{\langle c \rangle_{i,exp} - \langle c \rangle_{i,th}}{\langle c \rangle_{i,exp}} \right)^2, \tag{2.12}$$

where $\langle c \rangle_{i,exp}$ and $\langle c \rangle_{i,th}$ are, respectively, the experimental and theoretical average concentration at each time point. The glucose uptake as a function of the local glucose level was correlated to the concentration cells are exposed to at the bottom of the Petri dish.

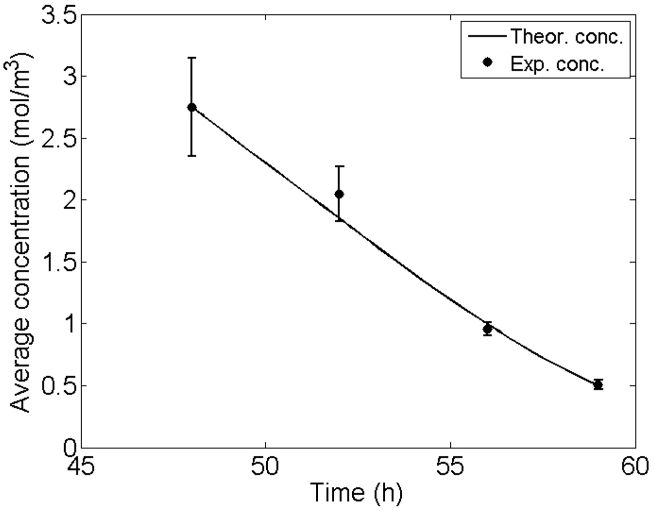

Figure 2.10: Comparison of the average glucose concentration obtained from the simulation with the experimental data during the exponential cell growth.

2.5 Results

Using the model developed for the Petri dish and the fitting algorithm, an explicit expression for the glucose uptake was achieved; Fig. 2.11 shows the cellular uptake as a function of the local glucose concentration. A linear dependence of the glucose uptake, Q_G, from the local glucose concentration was obtained, as reported by Eq. 2.13:

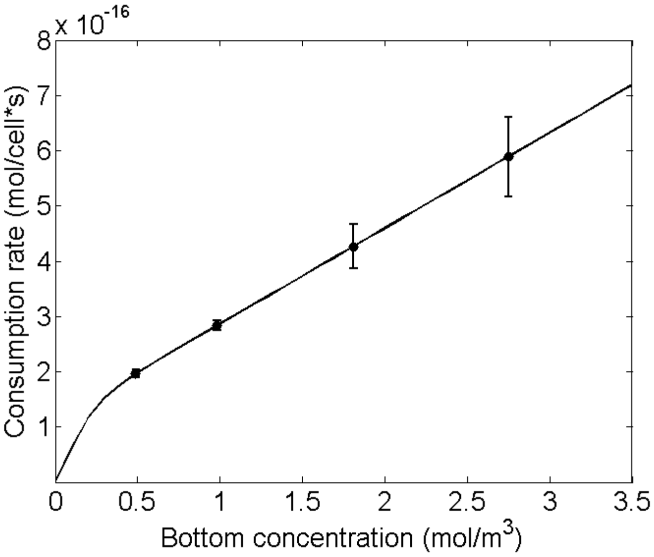

Figure 2.11: Glucose consumption rate dependence from the local glucose concentration. The error bars were obtained from the average measurements by means of the error propagation theory.

$$Q_G = (mc_G + q)\,\varphi, \tag{2.13}$$

$$\varphi = \tanh(\lambda c_G), \tag{2.14}$$

where m and q are two kinetic parameters, and φ is a damping factor in order to set to zero the uptake when the glucose concentration goes to zero without discontinuities. It is defined by Eq. 2.15:

$$\lambda \in \mathbb{R} : \begin{cases} 0 \leq \lambda \leq 1, & \text{if } 0 \leq c_G \leq 1, \\ \lambda = 1, & \text{if } c_G > 1. \end{cases} \tag{2.15}$$

The values of the three kinetic parameters required by Eq. (2.13) and Eq. (2.14), are listed in Table 2.1.

Table 2.1: Glucose consumption rate parameters: their symbols and the respective values.

Symbol	Value
m	$1.73 \times 10^{-16}\,\mathrm{m^3\,cell^{-1}\,s^{-1}}$
q	$1.14 \times 10^{-16}\,\mathrm{mol\,cell^{-1}\,s^{-1}}$
λ	5.3

3

Macroscopic cell growth modeling in a 2D microfluidic bioreactor

In this chapter the analysis of microfluidic chips for cell culture will be presented. Two published examples were studied focusing on the operative conditions and how to carry out a dynamic cell culture taking into account both nutrients and endogenous factors. This work is aimed to investigate the optimal management of microfluidic integrated cell culture systems. This technology will be further discuss in chapter 6.

3.1 Introduction

The traditional cell culture systems have been modified in the recent years thanks to the new culture technologies. Dynamic culture systems (bioreactor) can better control the cell microenvironment [3, 59] and enhance the mass transport of nutrients and metabolic waste products to and from cells [69]. The miniaturization of these systems, thanks to the microfabrication technologies, brought to the development of microscale devices which have been used in several applications ranging from biological analysis [82], drug testing [83, 84], and cell studies, both single cell [85] and cell culture system [86].

Microfluidic platform enables to decrease costs, allows to perform high-throughput analysis for multi-parametric testing [87, 88], a better fluid control [89] and cellular microenvironment [86, 90]. For instance Cimetta et al. [86] have studied the effects of cell density and transport regime on cell morphology and differentiation in human embryonic stem cells (hESC). In addition, the reduced system volume promotes a fast cell response to spatial and temporal stimuli [91], and the higher cell–medium volume ratio (low medium volume), promotes an higher signal-stimulus ratio, thus the cell response can be measured.

A microfluidic cell culture (microbioreactor) is basically composed of a culture chamber, where cells are seeded, an inlet and outlet channel for the medium delivery to and from the cells, a medium reservoir upstream the chamber, a discharged medium collector downstream, and, if required a gas exchanger.

Cell fate is highly related to its microenvironment properties, i.e. mechanical and physical stimuli, electrical and biochemical signals, such as autocrine and paracrine secretion, endogenous and metabolites molecules.

In a traditional static culture (e.g. Petri dish), medium is usually replaced every 1 or 2 days in order to remove the waste products accumulated in the cell microenvironment and to provide nutrients, such as glucose, necessary for the cell metabolism. Since glucose plays a central role in biological processes, its concentration in the system could be considered as an index of the cell activities .

In dynamic cell cultures, medium continuously flows through the system to enhance mass transport to and from the cells. As in the static condition, cell media replacement is required for providing nutrients and for catabolite removal. Unlike the traditional culture, providing fresh media in a dynamic systems can damage the microenvironment surrounding the cells (defined stem cell niche). Indeed medium flow rate could wash out the endogenous factors secreted by cells altering the biochemical composition of soluble factors in contact with cell membrane.

Several microfluidic bioreactor have been proposed in literature, starting from a simple configuration where the culture chamber is represented by an enlargement of the microfluidic channel (Fig. 3.1A) [92], to a more complex systems where cells are seeded at the bottom of a well, therefore they are separated from the inlet and outlet channels [90]. This configuration adds a further mass transfer resistance because the mass transport takes place for higher characteristic distance due to the separation

H_c (Fig. 3.1B). This configuration reduces the efficiency of metabolic delivery to the cell culture, but it avoids that the cell microenvironment is negatively affected by the fluid dynamic regime (i.e. soluble factors wash out).

In this perspective, for both configurations, depending on the uptake and the release rate of metabolites and growth factors, an optimal flow rate value should be defined. This optimal flow rate value could range from 1×10^{-5} to 1×10^{3} µL /min, depending on specific conditions. This wide value range raises technological issues for the management of microfluidic platform.

For this reasons, we aimed to use a discontinuous cell media flow would ensure a suitable glucose level range for cell metabolism, and at the same time it preserves the cell niche maintaining all hormones and endogenous factors above the threshold values required for cell processes such as cell signaling and proliferation.

In this work we studied the cell uptake of oxygen and glucose, and the secretion of epidermal growth factor (EGF) as a function of the most common microfluidic configurations. Afterwards, we analyzed the effect of a discontinuous flow in order to provide nutrients without impairing the cell microenvironment. Such condition was achieved with a pulsatile flow, that is switching from a dynamic to a static state. The flow rate, the duration and the frequency of the medium feeding were fixed based on the cell glucose metabolism.

The full optimization of this system is not behind the aim of this chapter, here we discuss potential alternative to conventional microfluidic cell culture system setup.

3.2 Theoretical framework

Two main configurations (Fig. 3.1) were used as model to investigate the role of discontinuous flow rate: I) the microfluidic platform reported by Gómez-Sjöberg et al. [92], II) the microfluidi chip developed by Figallo et al. [90]. The first one is composed of a rectangular culture chamber with a microchannel at its inlet and outlet that crosses the chamber in the middle; the chamber has the same height of the channel (Fig. 3.1A). The latter configuration is composed of a cylindrical culture chamber with a microchannel at its inlet and outlet which crosses the chamber at its top (Fig. 3.1B).

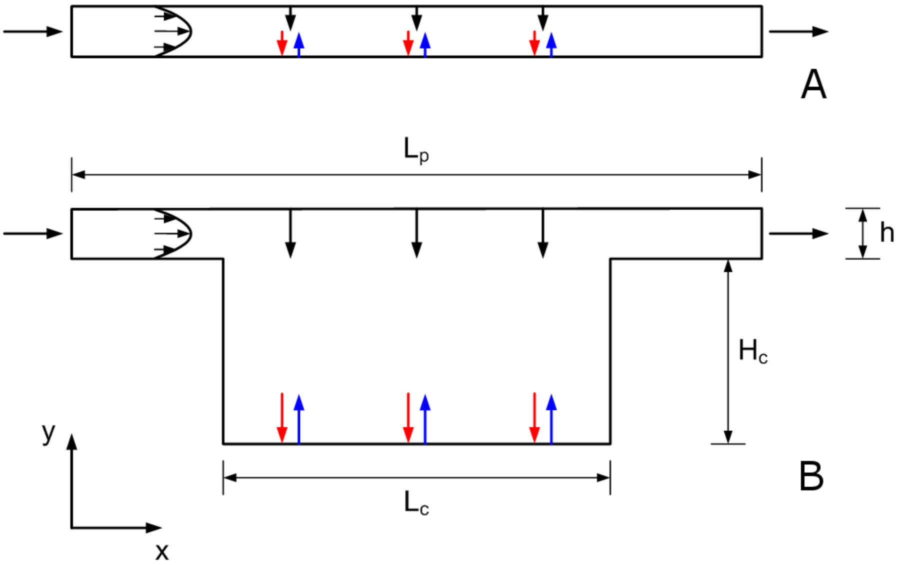

Figure 3.1: Representation of the two microfluidic platform configurations type developed by (A) Gómez-Sjöberg et al. [92] and by (B) Figallo et al. [90]. The black arrows from the top of the geometry depict the oxygen inward flux from the PDMS, the red arrows show the outward flux of nutrients to the cells, and the blue arrows are the flux of factors secreted by the cells

For this study a typical size for a microfluidic platform was used, that is a channel height of 50 µm, a culture chamber length equals to 1 mm (as reported by Gómez-Sjöberg et al. [92]), while the flow rate ranges from 1×10^{-4} to 1×10^{-1} µL /min.

In both cases, cells adhere at the bottom of the culture chambers and fresh cell media flows through the microfluidic platform by means of perfusion, it means that convection and diffusion regulate the species mass transport. Because of the cell metabolism, there is a concentration gradient between cell microenvironment and the medium bulk, hence a flux of nutrients from the bulk to the cells. In contrast there is an inward flux of waste products and factors secreted by cells. Since systems are made in PDMS (Polydimethylsiloxane), an inward oxygen flux must be considered during the overall experiment duration due to the high gas-permeability of the PDMS.

In this study we considered the embryonic stem cells (ESCs) growth, taking into account, as species of interest, oxygen, glucose, and epidermal growth factor (EGF). ESCs are very sensitive to an *in vitro* microenvironment on their phenotypic expression. In addition, we analyzed the effect of the chamber geometry on the cell behavior, along with the two configurations, a third one was chosen changing the chamber length-height ratio. The comparison between these three cases was performed based on a variable $\tilde{Q}$ which is the ratio between the glucose demand by the system and the glucose provided (Eq. (3.1)):

$$\tilde{Q} = \frac{\text{Inlet glucose flux}}{\text{Consumed glucose}}. \tag{3.1}$$

After the comparison between different configurations, a discontinuous cell media flow case was described. Such experimental condition could be required if we want to preserve the cell activities providing the nutrients without affecting the cell niche.

3.3 Mathematical model

Equations of change have been used to describe the microfluidic cell culture system and to develop the mathematical model. Specifically we utilized the Navier-Stokes equation and the equation of continuity for species. Both the continuous and discontinuous cases will be presented pointing out their differences.

3.3.1 Medium fluid dynamic

The medium fluid dynamics in the culture chamber was described by the Navier-Stokes equations for incompressible fluids:

$$\rho \frac{D\boldsymbol{v}}{Dt} = -\nabla p + \mu \nabla^2 \boldsymbol{v} + \rho \boldsymbol{g}, \tag{3.2}$$

where ρ is the medium density, $\boldsymbol{v}$ is the velocity field, p is the pressure, μ the medium viscosity, and $\boldsymbol{g}$ the gravity. The boundary conditions were set as a wall, except for the inlet and the outlet of the system, they were defined as:

$$\boldsymbol{v}\left(x, y, t\right) = \dot{Q}/A \qquad x = 0, \tag{3.3}$$

$$p_{outlet} = 0 \qquad x = L_p, \tag{3.4}$$

where $\dot{Q}$ is the medium flow rate which enters in the system and A is the channel cross section. For the discontinuous case, when there is no medium convection, the velocity was set to zero.

3.3.2 Mass transport equations

The temporal species concentration profile was studied by the convection and diffusion mass transport equation, no reactions occurred in the medium. Indeed cells are seeded at the bottom of the cell culture chamber, therefore its cellular activity (uptake or production) can be assumed as a flux (outward or inward) at the cell interface. The mass transport for oxygen, glucose and EGF were expressed by the species mass balance:

$$\frac{\partial c_i}{\partial t} = -\nabla N_i. \tag{3.5}$$

In Eq. (3.5), c_i is the species concentration, and N_i is the flux, it considered both convection and diffusion phenomena:

$$N_i = \boldsymbol{v} c_i - D_i \nabla c_i, \tag{3.6}$$

where D_i is the species diffusion coefficient in medium at 37 °C.

3.3.2.1 Initial conditions

The initial conditions for the Navier-Stokes equation (Eq. (3.2)) and for the mass balance equations (Eq. (3.5)) follow:

$$\boldsymbol{v}\left(x,y,t\right) = 0 \qquad t = t_{in}, \tag{3.7}$$

$$c_{O_2}\left(x,y,t\right) = c_{O_2,0} \qquad t = t_{in}, \tag{3.8}$$

$$c_G\left(x,y,t\right) = c_{G,0} \qquad t = t_{in}, \tag{3.9}$$

$$c_{EGF}\left(x,y,t\right) = 0 \qquad t = t_{in}. \tag{3.10}$$

At the beginning, in the culture chamber there is fresh cell media in equilibrium with the incubator atmosphere. $c_{O_2,0}$ is the oxygen concentration in equilibrium with the incubator atmosphere and $c_{G,0}$ is the glucose concentration in fresh medium.

3.3.2.2 Boundary conditions

Two different fluid dynamics cases were studied, continuous and discontinuous, so we had two sets of boundary conditions; they are summarized in Table 3.1 for the continuous case, and in Table 3.2 for the discontinuous one. In the transient phase, fresh media is pumped into the chamber and leaves the system due to the convection. Cell metabolism generates a concentration gradient of oxygen and glucose from the medium bulk to the bottom of the channel, moreover there is an inward flux of EGF from the cells to the medium. At the top of the system an oxygen inward flux was considered due to the PDMS gas permeability [93]. In this second condition there is no medium flow, thus at the inlet and outlet insulation conditions were used, while the conditions at the top and the bottom of the system are the same depicted in Table 3.1 .

Table 3.1: Boundary conditions for the mass transport equations for the continuous configuration.

Continuous			
Boundary	Oxygen	Glucose	EGF
Channel inlet	$c_{O_2}^{sat}$	c_G^{phys}	$c_{EGF} = 0$
Channel outlet	Convective flux	Convective flux	Convective flux
Chamber bottom	$N_{O_2} = R_{O_2}$	$N_G = R_G$	$N_{EGF} = R_{EGF}$
Channel top	$N_{O_2} = N_{O_2}^{ext}$	Insulation	Insulation
Others	Insulation	Insulation	Insulation

Table 3.2: Boundary conditions for the mass transport equations for the discontinuous configuration.

Discontinuous			
Boundary	Oxygen	Glucose	EGF
Channel inlet	Insulation	Insulation	Insulation
Channel outlet	Insulation	Insulation	Insulation
Chamber bottom	$N_{O_2} = R_{O_2}$	$N_G = R_G$	$N_{EGF} = R_{EGF}$
Channel top	$N_{O_2} = N_{O_2}^{ext}$	Insulation	Insulation
Others	Insulation	Insulation	Insulation

3.3.3 Phenomenological expressions

To solve the mathematical model, Eq. (3.2) and Eq. (3.5) must be coupled with the expression for the flux at the top of the chamber, and for the kinetic of uptake and production. The inward oxygen flux through the PDMS follows [93]:

$$N_{O_2}^{ext} = K_0 \left(p_{O_2} - k_{O_2} c_{O_2} \right), \tag{3.11}$$

where K_0 is the global mass transfer coefficient ($K_0 = P_m/\sigma$, P_m is the oxygen permeability in PDMS [94] and σ is the PDMS thickness), p_{O2} is the oxygen partial pressure in atmosphere and k_{O_2} is Henry's coefficient for oxygen.

The oxygen and glucose uptake were described, respectively, as a Michaelis-Menten equation and a first order kinetic, as reported in literature [95] for the mESCs:

$$R_{O_2} = -\left[\left(k_1 c_G + k_2 \right) \frac{c_{O_2}}{c_{O_2} + k_3} \right] \rho_{cell}, \tag{3.12}$$

$$R_G = -\left[k_4 c_G \psi + \left(k_5 c_{O_2} + k_6 \right) k_4 c_G \left(1 - \psi \right) \right] \rho_{cell}. \tag{3.13}$$

In Eq. (3.12), k_1, k_2, and k_3 are the oxygen kinetic parameters and ρ_{cell} is the overall cell density; whereas in Eq (3.13), k_4, k_5, and k_6 are the glucose kinetic parameters and ψ is a damping function. It accounts for a shift in glucose uptake due to low oxygen concentration (Pasteur effect) without discontinuities in Eq. (3.13), it follows:

$$\psi = \frac{\tanh \left[k_7 \left(c_{O_2} - c_{O_2}^{lim} \right) \right] + 1}{2}, \tag{3.14}$$

where k_7 is the damping coefficient and $c_{O_2}^{lim}$ is the oxygen threshold value at which the glucose consumption rate switches.

The secretion rate of the epidermal growth factor was described as a linear function of the cell number [96–98]:

$$R_{EGF} = q_{EGF} \rho_{cell} S, \tag{3.15}$$

where q_{EGF} is the specific production rate and S is the culture chamber surface.

3.3.4 Cell growth equation

The cell growth was described with a logistic cell growth model [44, 99]; growth depends on the average oxygen concentration, $c_{O_2}^{aver}$, in the cell culture and on the overall cell density, ρ_{cell}:

$$\frac{d\rho_{cell}}{dt} = \left(1 - \frac{\rho_{cell}}{\rho_{cell}^{max}}\right) \mu_{cell} \frac{c_{O_2}^{aver}}{K + c_{O_2}^{aver}} \rho_{cell}. \tag{3.16}$$

In Eq. (3.16) ρ_{cell}^{max} is the maximum cell density supported by the bioreactor or rather the density at cell confluence, μ_{cell} is the maximum growth rate, and K is the half-saturation coefficient. The average glucose concentration in the culture chamber was expressed by:

$$c_{O_2}^{aver} = \frac{\displaystyle\int_V c_{O_2}\, dV}{\displaystyle\int_V dV}, \tag{3.17}$$

where V is the volume of the chamber. The initial condition for Eq. (3.16) was expressed by the initial cell density, $\rho_{cell,0}$:

$$\rho_{cell}(t) = \rho_{cell,0} \qquad\qquad t = t_{in}. \tag{3.18}$$

3.4 Numerical model

Both the continuous and discontinuous model were numerically solved using the finite element method (FEM), the algorithm was implemented in COMSOL Multiphysics 3.5 (COMSOL Inc., Burlington, MA). The solution for the first case is straightforward, one the other hand, the second model requires the resolution of several loops, each loop is composed of two models:

- dynamic state (medium flow);
- steady state (static condition);

to speed up the algorithm, the two codes were developed in COMSOL and then embedded in a main MATLAB (The MathWorks, Natick, MA) code (Fig. 3.2). To

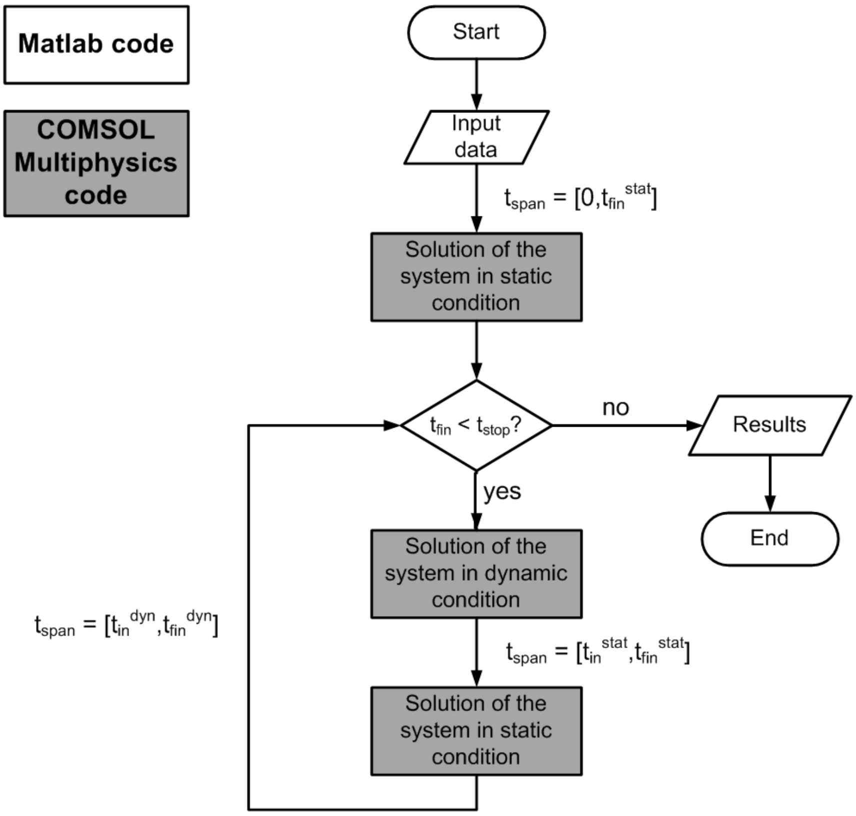

Figure 3.2: Scheme of the algorithm for solving the microfluidic platform model.

this end a MATLAB/COMSOL interface was created: starting from the input data, MATLAB solves the first step ($t_{span} = \left[0, t_{fin}^{stat}\right]$), that is the static condition, with the COMSOL model, afterwards COMSOL outcomes are stored by MATLAB which updates the time span and the initial conditions in order to solve the dynamic state. Specifically this model uses the the solution at the final time of the previous model, hence $t_{span} = \left[t_{in}^{dyn}, t_{fin}^{dyn}\right]$, where the initial time for the dynamic model (t_{in}^{dyn}) equals the final time of the previous static model (t_{fin}^{stat}). Then the code modifies again the initial conditions and the time span according to the last solution; MATLAB algorithm iterates this process, using COMSOL functions, until reaches the final time.

3.5 Results

The mathematical model describes the temporal evolution of species inside the microfluidic platform. All the following plots will consider concentration profiles measured at the bottom-center of the culture chamber; the model simulated experiments for 20 days. First of all a base case using the Gómez-Sjöberg device will be presented, afterwards we will focus on the analysis of the culture chamber configuration effect on the cell behavior, at last we will compare the continuous medium flow condition with the discontinuous one for a specific case.

3.5.1 Base case study

The device developed by Gómez-Sjöberg was considered as base case to show the main model outcomes. Figure 3.3 shows the temporal profiles of cell density (solid line), oxygen (dashed line), glucose (dotted line) and EGF (dash-dot line) concentration at the center of the culture chamber. All the values were normalized using the basal condition ($c_{O_2,0}$, the oxygen concentration in equilibrium with the incubator atmosphere and $c_{G,0}$ the glucose concentration in fresh medium for glucose continuity equation) or the maximum value (c_{EGF}^{max} for EGF, and ρ_{cell}^{max} for cell density). Cells grow as a function of the cell density and oxygen concentration according to Eq. (3.16), after 20 days the maximum cell density is reached. Since the EGF secretion is proportional to the cell density (Eq. (3.15)) its trend is similar to the cell density. The oxygen concentration maintains an high level for all the time because the medium flow inlet and the inward flux through the PDMS supply the cellular oxygen demand. On the other hand, the glucose concentration rapidly decreases in time reaching the 20 % of the initial value after 10 days.

3.5.2 Effect of the microfluidic bioreactor configuration

The effect of the culture chamber configuration on the cell culture was studied varying the ratio H_c/L_c (Fig. 3.1), in particular we used:

- $H_c/L_c = 0$ — Gómez-Sjöberg et al. configuration;
- $H_c/L_c = 1/1$ — Figallo et al. configuration;

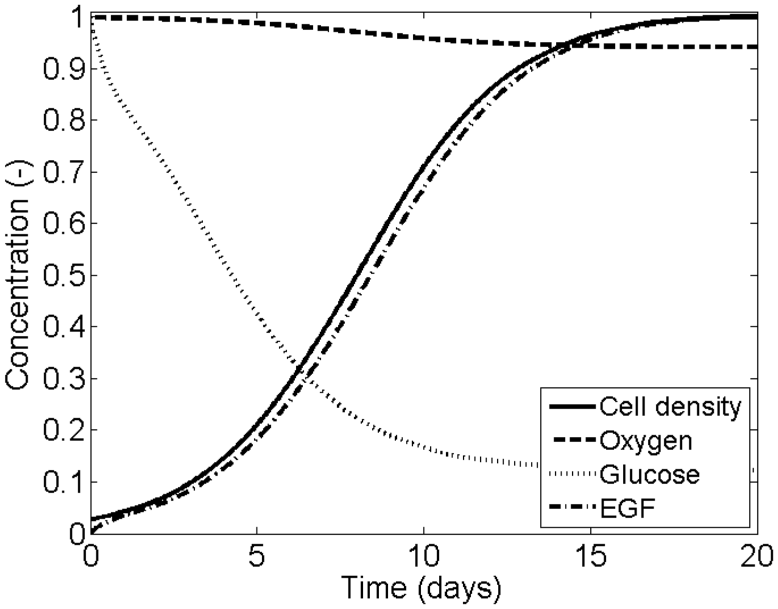

Figure 3.3: Temporal profiles at the center of the culture chamber for the Gómez-Sjöberg microfluidic bioreactor. All the values were normalized using the basal condition (oxygen and glucose) or the maximum value (cell density and EGF). Cell density (solid line), oxygen (dashed line), glucose (dotted line) and EGF (dash-dot line) concentration.

- $H_c/L_c = 10/1$ — conventional culture system limit.

The analysis was performed changing the variable $\tilde{Q}$, it is the glucose rate normalized by the maximum consumption rate; it is expressed by:

$$\tilde{Q} = \frac{\dot{Q} c_{G,0}}{Q_G \left(c_{G,0}\right) \rho_{cell} S}, \tag{3.19}$$

where $\dot{Q}$ is the medium flow rate, $c_{G,0}$ is the glucose concentration in fresh medium, $Q_G\left(c_{G,0}\right)$ is the maximum specific cell glucose uptake (calculated at the $c_{G,0}$), and S is the culture chamber area. In the following discussion only glucose and EGF profiles will be analyzed since they are the limiting factors for the cells culture, oxygen is usually at high level.

Figure 3.4 shows the effect of the chamber configuration and the flow rate on the glucose (Fig. 3.4A) and on the EGF (Fig. 3.4B) concentration. At small values of $\tilde{Q}$, the system is limited by the mass transport, glucose concentration approaches to low values. On the other hand, at high value of $\tilde{Q}$, the glucose level is constant

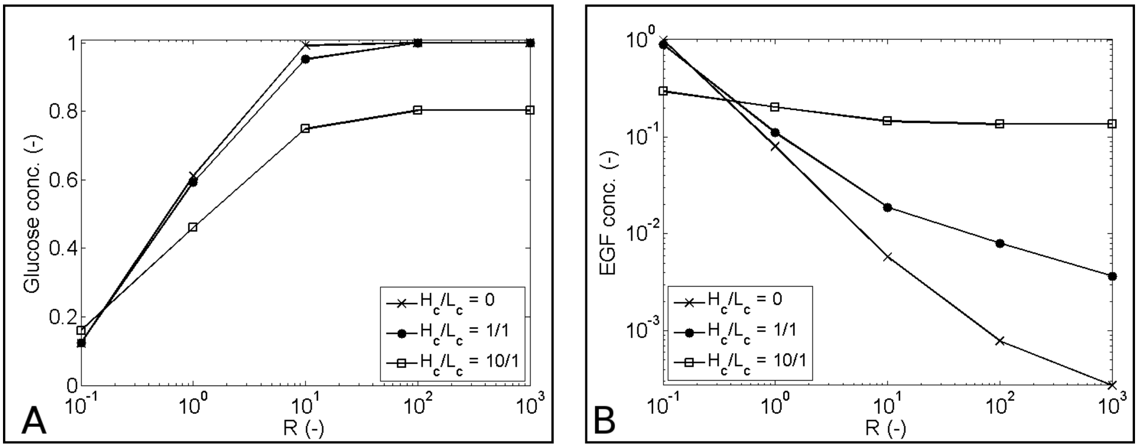

Figure 3.4: Effect of the culture chamber configuration on the temporal profile of glucose (A) and EGF (B) concentration. The chamber height, H_c, equals 0 (×), 1 (•), and 10 mm (□).

because the uptake is the limiting phenomenon. For halfway values of $\tilde{Q}$, the glucose uptake and mass transport are in a competitive regime.

The flow rate has an opposite influence on the EGF concentration, the smaller is the medium flow the higher is the EGF level. In fact a great medium flow washes out EGF secreted by cells; nonetheless in the configuration with bigger chamber height this effect is negligible because of the diffusion regime.

The configuration with a H_c/L_c ratio equals 1 has an average behavior between the other two limiting cases; in the operative conditions range, it is able to maintain a high glucose concentration, and at the same time avoids the cell microenvironment wash out.

3.5.3 Discontinuous cell media perfusion

As previously described, the microfluidic platform developed by Figallo et al. [90] can provide suitable culture conditions, nevertheless the this results is not guaranteed. A discontinuous medium flow rate (Fig. 3.5) could maintain glucose and EGF concentration within an appropriate ranges for cell viability. The discontinuous case (I) was simulated assuming an experiment duration of 20 days; every 24 hours the cell media is pumped in the culture chamber for 5 minutes in order to replace 80 % of the medium inside the system. The two continuous cases were obtained

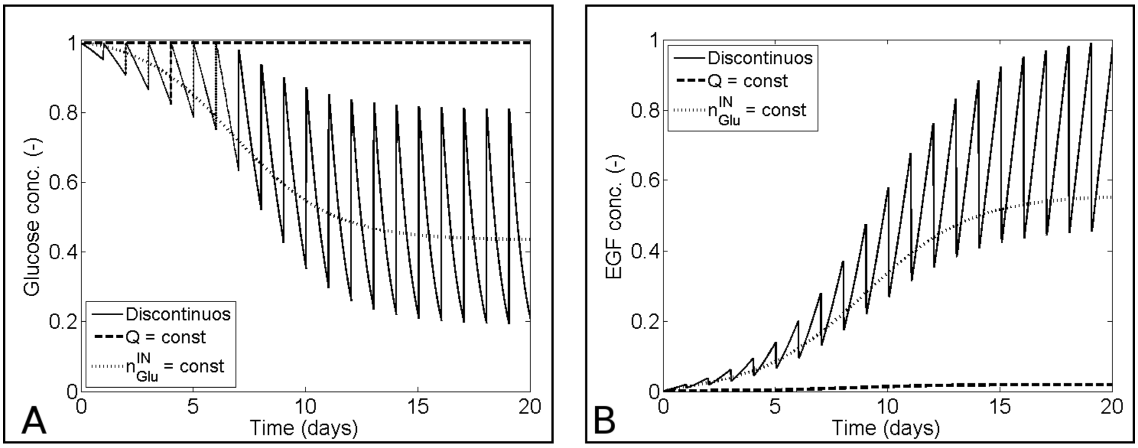

Figure 3.5: Comparison between a discontinuous case (solid line) and two continuous cases obtained using the same flow rate (bold dashed line) of the discontinuous conditions and the same amount of glucose (bold dotted line).

using the same flow rate of the discontinuous condition (II) and proving the same total amount of glucose to the cells (III).

The three experimental setups can provide a sufficient glucose level (Fig. 3.5A); in the case I the dimensionless glucose level ranges from 0.2 to 0.8, on the other hand, condition II maintains the maximum glucose concentration. However, this configuration fails in preserving the cell niche, indeed the EGF concentration is almost 0. Condition III better maintains the cell microenvironment, however the flow rate required could be impossible to setup because it is about 3 order of magnitude less than the discontinuous condition, therefore impossible to realize because of technological limitations. The discontinuous setup gives the best results with the higher EGF concentration.

3.6 Conclusions

In this chapter, a microfluidic bioreactor was analyzed developing a mathematical model to describe the overall cell growth and the local mass transport in such system. The cell microenvironment affects the cell processes [100], therefore in a dynamic culture is important to sustain cell metabolism, providing nutrients, and at the same time preserving the cell niche properties required for cell activities.

The model depicts the cell growth and the temporal evolution of the local concentration of oxygen, glucose and epidermal growth factor. It shows the double effect of the flow rate on the cell microenvironment, indeed it provides nutrients to the cells, but also it could damage the cell niche.

The mathematical model was applied for studying the effect of two different culture chamber configurations [90, 92] on the system response. The analysis showed that the geometrical configuration, along with the medium flow rate play a fundamental role in controlling the cell microenvironment; in addition an optimal configuration among those considered was detected.

At last the mathematical model was used to study the advantages of a discontinuous medium flow through the microfluidic culture chamber. The continuous case which provides the same amount of nutrients to the system is almost equal to the discontinuous case, however the first configuration required a flow rate 2 or 3 times lower. Therefore due to technological limitations it could be impossible to guarantee a constant flow rate at this condition. The discontinuous strategy is a better compromise sine it is able to preserve the cell niche, in term of both nutrients and factors released by cells.

A future development of this work could be the optimization of the discontinuous case considering the experimental constraints, i.e. the frequency of the medium flow, its length of time, the flow rate, and the length of time of the static condition. For example, setting the minimum glucose concentration, we could performed a frequency optimization, that is a frequency of medium feeding as function of the cell growth in order to tightly control the oscillatory system behavior, maintaining the concentration above the threshold level.

4

Microscopic cell growth modeling in a perfusion three-dimensional bioreactor

In this chapter the three-dimensional cell growth in a porous system where the proliferation depends on the cell microenvironment properties will be analyzed. The system is described by means of a mathematical model which considers the most important phenomena that characterized a perfused bioreactor; finally two case studies will be presented: (a) the optimization of the experimental conditions for hepatic precursor cell culture, and (b) the validation of the mathematical model using murine skeletal muscle cell line C2C12.

4.1 Introduction

In vivo, cells are part of a three-dimensional (3D) complex multiscale organization that starts from small cell clusters, and extends to tissues, and to large volume organs. The physiology of an organ depends on the single cell behavior and the cell microenvironment defined by mass transport phenomena of biochemical species, mechanical and hydrodynamic stimuli, electrical signals, and physical and biochemical interaction with the neighboring cells [101].

In contrast, conventional *in vitro* cell culture is based on a two-dimensional (2D) cell culture system where many of the complex *in vivo* stimuli and interactions can be altered or not properly reproduced. Therefore, there is a pressing need of scaling cell culture systems from the 2D to 3D environment to more closely recreate the behavior of the tissue *in vivo*, which may better simulate *in vivo* biology, physiology, or pathophysiology [102–104].

One of the main objective of the three-dimensional cell cultures is the control of the cell behavior to achieve an homogeneous system. The cell fate is characterized by intrinsic and extrinsic variability, related, respectively, to the cell itself and to the microenvironmental properties [105]. Both of them can induce heterogeneity in the cell response, leading to a heterogeneous 3D cell culture; the extrinsic variability is the only one that can be reduced by controlling the properties of the cell microenvironment manipulating the macroscopic operative conditions.

In vivo 3D dynamic cell culture are characterized by two fundamental components: a porous construct for the cell adhesion (scaffold), and a technological device (bioreactor) to overcome the mass transport limitations. The scaffold may be fabricated from natural or synthetic materials [3, 106] and it is selected based on the cell culture and on its morphological properties (i.e. porosity and tortuosity).

The bioreactor promotes the mass transport by means of the medium convection; one of the most promising devices is the perfusion bioreactor where the cell media flows through the scaffold and the cells, providing all the nutrients to the system and removing the waste products. The medium perfusion and the scaffold morphology affect the cell microenvironment properties, hence the cell heterogeneity.

It is fundamental to rationalize the correlation between macroscopic variables such as scaffold morphology and medium flow rate and the microscopic properties of the cell culture in order to optimize the experimental parameters for achieving a high and homogeneous cell density.

In the following sections the modeling of the 3D dynamic cell culture will be treated for describing the cell heterogeneity and its dependence from the operative variables.

4.2 Theoretical framework

A bioreactor system is usually composed of four units: a medium reservoir, a volumetric pump, a gas exchanger and a culture chamber. The medium reservoir ensures all the nutrients necessary for the duration of the experiment while the volumetric pump guarantees a constant flow independently from the pressure drop. The gas exchanger controls the oxygen and carbon dioxide (i.e. pH) level in the cell media, the culture chamber holds a 3D structure (scaffold) and cells are seeded onto its surface; in this configuration the medium is constrained to flow through the scaffold (in detail a collagen scaffold). It is composed of a complex network of interconnected pores with different size, length and tortuosity.

Since this project focused on the cell growth heterogeneity, we assumed the scaffold geometry as a bundle of independent parallel channels [107] with a defined channel diameter distribution. Under this assumption, for a given channel diameter distribution, it is possible to determine the flow rate partitioning based on the channel diameter (Fanning equation) considering that the isohead loss is the same for each channel. Hence for each channel is defined an external diameter, D_i^{ext}, and a specific flow rate, Q_i, and for a short interval of time, each channel geometry can be studied independently.

In this subsystem we assumed that cells adhere on the inner channel surface creating a uniform layer, hence an effective diameter is defined ($D = 2S$), that is the difference between the outer channel diameter and the cell thickness. Two different domain are identified, the medium (domain I) and the cell domain (domain II). In cell cultures, cells are subjected to a variety of molecular, structural, hydrodynamic, mechanical, and electrical cues and their spatial and temporal levels and combinations [3] which affect cell fate. Herein we studied the effect of the oxygen on the cell behavior, since it is one of the most important metabolite for the cell viability and proliferation [39]. Inside a channel, medium, having oxygen concentration $c_{O_2}^{I}$, flows from the top to the bottom of it with velocity field v_z, and oxygen diffuses toward the domain II. In this domain the transport of the metabolite ($c_{O_2}^{II}$) is governed by the intracellular diffusion, since there is no medium convection here, finally oxygen is consumed by the cell uptake. Because of the metabolism, cell growth modifies the channel geometry, therefore the domain I/domain II interface position change in time, that the effective diameter ($2S$) is reduced changing also the whole system fluid dynamics. Moreover it was assumed an inhibition of the cell proliferation due to the lack of oxygen and to the shear stress imposed by medium flow on the cell surface.

4.3 Mathematical model

As previously described, the bioreactor system, hence the 3D porous scaffold can be approximated as a bundle of stream-flow oriented parallel channels. Considering a period of time shorter than the cell doubling time, the cell growth does not affect the flow rate partitioning, therefore each single channel is independent and they can be studied separately.

4.3.1 Bioreactor model

For a given channel diameter distribution, the Fanning equation provides the flow rate, Q_i, for a single channel i as a function of the total pressure drop, ΔP:

$$Q_i = \frac{\pi D_i^4 \Delta P}{128 \mu L}, \tag{4.1}$$

where μ is the medium viscosity and L and D_i are the channel length (that is the scaffold height) and the channel diameter, respectively. The flow rate partitioning must satisfy the overall mass balance expressed as followed:

$$Q_{tot} = \sum_{k=1}^{N_D} p_k(D_k) Q_k. \tag{4.2}$$

In Eq. (4.2) Q_{tot} is the total medium flow rate, N_D is the number of channel classes and p_k is the probability from the channel diameter distribution. The flow rate partitioning is obtained combining Eq. (4.1) and Eq. (4.2). Figure 4.1 shows the algorithm used for solving the bioreactor model. It is composed of two main for loops, one for the time and one for the diameters. Starting from the input data

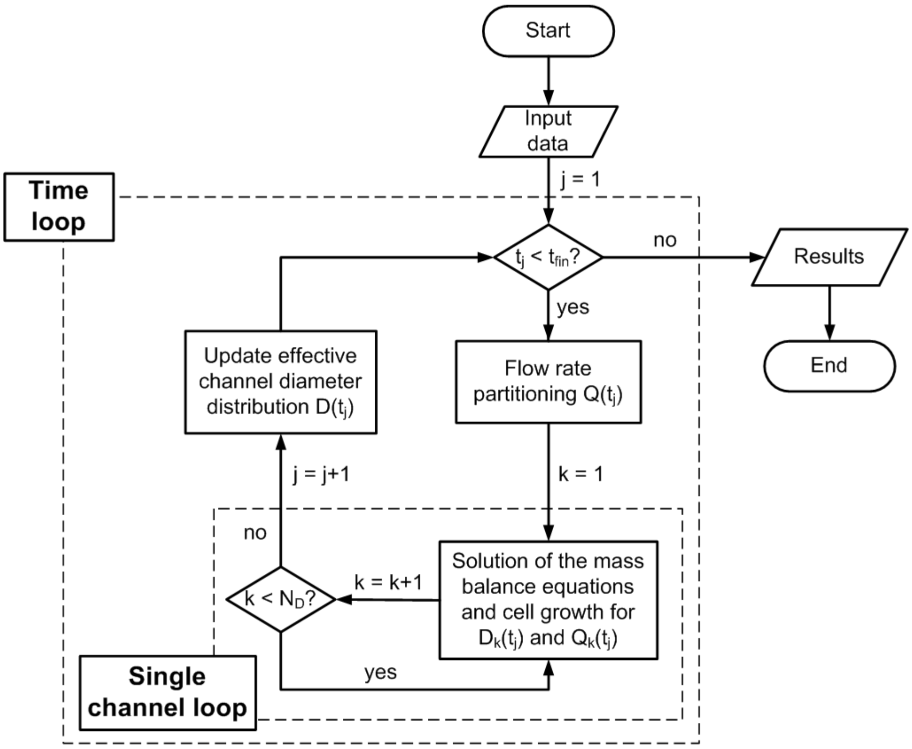

Figure 4.1: Scheme of the algorithm for solving the bioreactor model.

such as biological and physical properties, operative conditions and the channel distribution, the code determines the flow rate partitioning, hence each single channel system is solved for a Δt period of time. When all the channel classes have been solved, since the cell growth modifies the effective channel diameter distribution, the new flow rate partitioning is recalculated and the model solves all single channel systems for the new Δt. The algorithm iterates until reaching the final time.

4.3.2 Single channel model

The single channel geometry is reported in Fig. 4.2. The region in the center is the medium domain, the one at the inner wall is the cell domain. The governing equation for domain I was solved in the range $0 \leq r < S\left(z,t\right)$, while the equations for domain II were solved in the range $S\left(z,t\right) \leq r \leq R$, where R is the channel radius. All the equation were derived for a cylindrical geometry, that is in term of axial and radial coordinates, indeed we assumed that all the phenomena are independent

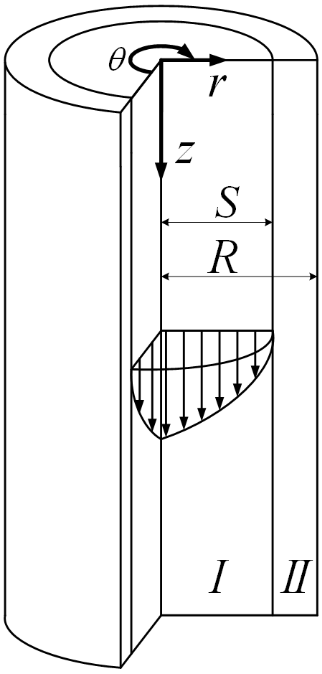

Figure 4.2: Scheme of the single channel geometry.

from the angular coordinate. The generic equation of continuity for oxygen for both domains are given by Eq. (4.3) and (4.4):

$$\frac{\partial c^{I}_{O_2}}{\partial t} = -\nabla N^{I}_{O_2} \qquad r \in [0, S(t)), \tag{4.3}$$

$$\frac{\partial c^{II}_{O_2}}{\partial t} = -\nabla N^{II}_{O_2} + R_{O_2} \qquad r \in [S(t), R]. \tag{4.4}$$

Hereafter the superscript I and II denote variables of domain I and II, respectively; c_{O_2} is the oxygen concentration, N_{O_2} is the oxygen flux and R_{O_2} is the cell oxygen uptake which occurs only in domain II. In this domain, also the cell growth equation must be considered:

$$\frac{dn}{dt} = R_{cell} \qquad r \in [S(t), R], \tag{4.5}$$

where n is the number of cells and R_{cell} is the cell growth rate.

4.3.2.1 Equations of Change

In domain I, we assumed that the convective flux is relevant only in the axial direction, moreover in the normal operative conditions, the axial diffusive flux is negligible if it is compared to the convection ($Pe > 1$). The microscopic oxygen mass balance follows:

$$\frac{\partial c_{O_2}^{I}}{\partial t} = -\left[\frac{1}{r}\frac{\partial}{\partial r}\left(rN_{O_2,r}^{I}\right)\right] - v_z\left(r,t\right)\frac{\partial c_{O_2}^{I}}{\partial z}. \tag{4.6}$$

In Eq. (4.6) $N_{O_2,r}$ is the radial diffusive flux and v_z is the axial velocity. In domain II, oxygen flux is expressed only by the radial diffusion:

$$\frac{\partial c_{O_2}^{II}}{\partial t} = -\left[\frac{1}{r}\frac{\partial}{\partial r}\left(rN_{O_2,r}^{II}\right)\right] + R_{O_2}. \tag{4.7}$$

Eq. (4.6) and (4.7) were solved with respect to the oxygen concentration with the following boundary and initial conditions.

Boundary conditions. Boundary conditions required to solved the microscopic mass balance equations are:

$$c_{O_2}^{I}\left(r,z,t\right) = c_{O_2,0} \qquad z = 0, \tag{4.8}$$

$$\frac{\partial c_{O_2}^{I}\left(r,z,t\right)}{\partial r} = 0 \qquad r = 0, \tag{4.9}$$

$$N_{O_2}^{I}\left(r,z,t\right) = N_{O_2}^{II}\left(r,z,t\right) \qquad r = S\left(t\right), \tag{4.10}$$

$$\frac{\partial c_{O_2}^{II}\left(r,z,t\right)}{\partial r} = 0 \qquad r = R, \tag{4.11}$$

where $c_{O_2,0}$ is the oxygen concentration in equilibrium with the incubator atmosphere hence at the inlet of the channel. Eq. (4.9) and (4.11) show, respectively, a symmetry and insulation condition in the center and at the wall of the channel, and Eq. (4.10) denotes the balance of fluxes at domain I/domain II interface.

Initial conditions. At the initial time, in both domains oxygen is in equilibrium with the incubator atmosphere, therefore the initial conditions follow:

$$c_{O_2}^{I}(r,z,t) = c_{O_2,0} \qquad t = t_{in}, \tag{4.12}$$

$$c_{O_2}^{II}(r,z,t) = c_{O_2,0} \qquad t = t_{in}. \tag{4.13}$$

4.3.2.2 Phenomenological expressions

For solving the system of equations, the previous Eq. (4.6) and (4.7) must be coupled with the constitutive expression for the oxygen flux in both domains, for the medium velocity, and for the oxygen uptake. The radial diffusive oxygen flux is expressed by Fick's law [108]:

$$N_{O_2,r}^{I} = -D_{O_2}^{I}\frac{\partial c_{O_2}^{I}}{\partial r}, \tag{4.14}$$

$$N_{O_2,r}^{II} = -D_{O_2}^{II}\frac{\partial c_{O_2}^{II}}{\partial r}, \tag{4.15}$$

where D_{O_2} is the oxygen diffusion coefficient at 37 °C. The medium velocity is obtained by Hagen-Poiseuille equation [108] because of the low Reynolds value in all channels:

$$v_z(r,z,t) = v_{z,max}\left[1-\left(\frac{r}{S(z,t)}\right)^2\right] = \frac{2Q}{\pi S(z,t)^2}\left[1-\left(\frac{r}{S(z,t)}\right)^2\right]. \tag{4.16}$$

The cell oxygen uptake was assumed as a Michaelis-Menten kinetic; it depends on the local oxygen concentration and on the specific cell volume [5, 34, 109]:

$$R_{O_2} = -\frac{1}{\tilde{v}_{cell}}\frac{Q_m c_{O_2}^{II}}{C_m + c_{O_2}^{II}}, \tag{4.17}$$

where $\tilde{v}_{cell}$ is the cell specific volume, Q_m is the maximal oxygen consumption rate, and C_m is the oxygen concentration at half-maximal oxygen consumption.

Finally an expression for the cell growth rate is necessary for solving Eq. (4.5) in order to determine the position of the interface between the two domains as function of the time and the axial coordinate. The expression was simplified as a first-order kinetic as reported in literature [39, 50, 51, 110], where the growth rate is proportional to the local oxygen concentration and to the number of cells:

$$R_{cell} = F_{damp} k_{cell} c_{O_2}^{II} n. \tag{4.18}$$

In Eq. (4.18), F_{damp} is a damping function, and k_{cell} is the cell growth kinetic constant. The damping function takes into account the inhibitory effect on the cell growth because of a low oxygen level and of a high shear stress on the cell surface; when the oxygen concentration reaches the minimum value necessary for the cell viability and/or the medium flow generate shear stress higher than the value that cells can tolerate, the growth stops. It was formulate as follow:

$$F_{damp} = \frac{1}{\pi} \left\{ \frac{\pi}{2} + \arctan \left[k_{damp} \left(c_{O_2}^{II} - c_{O_2}^{lim} \right) \left(S\left(z,t\right) - S^{lim} \right) \right] \right\}, \tag{4.19}$$

$$S^{lim} = \left(\frac{4\mu Q}{\pi \tau_{shear}} \right)^{1/3}, \tag{4.20}$$

k_{damp} is the tunable damping coefficient which determines the steepness of the damping function between 1 and 0, $c_{O_2}^{lim}$ is the minimum threshold of oxygen concentration necessary for the cell growth, and S^{lim} is the effective channel radius below which the shear stress inhibits the cell growth or induces cell detachment at a rate equal to cell growth rate. Assuming a constant specific cell volume the number of cells can be expressed as:

$$n = \frac{V_{cell}}{\tilde{v}_{cell}} = \frac{1}{\tilde{v}_{cell}} \int_0^{2\pi} \int_0^L \int_{S(z,t)}^R r \, dr dz d\vartheta, \tag{4.21}$$

where V_{cell} is the total cell volume. Combining Eq. (4.5), (4.18) and (4.21) the rate of displacement of the effective channel radius, dS/dt, is obtain:

$$\frac{dS}{dt} = -\frac{k_{cell}}{S\left(z,t\right)} \int_{S(z,t)}^R F_{damp} c_{O_2}^{II} r \, dr. \tag{4.22}$$

The initial condition for Eq. (4.22) derived from the initial cell number which was converted to an initial effective channel radius, S_0:

$$S\left(z,t\right) = S_0 \qquad\qquad t = t_{in}, \tag{4.23}$$

4.4 Numerical model

Since there is no analytical solution for the mathematical model, a numerical algorithm was developed; first and foremost, all the equations were normalized in order to:

- reduce numerical instability;
- avoid round-off due to manipulations with large/small numbers;
- assess the relative importance of terms in the model equations.

The dimensionless form of the model was obtained using the following scaling factors:

$$\tau = \frac{D^I_{O_2}}{L^2}t, \qquad \tilde{r} = \frac{r}{R}, \qquad \tilde{z} = \frac{z}{L}, \qquad \tilde{s}\left(\tilde{z},\tau\right) = \frac{S\left(z,t\right)}{R}, \tag{4.24}$$

$$c^I\left(\tilde{r},\tilde{z},\tau\right) = \frac{c^I_{O_2}\left(r,z,t\right)}{c_{O_2,0}}, \qquad c^{II}\left(\tilde{r},\tilde{z},\tau\right) = \frac{c^{II}_{O_2}\left(r,z,t\right)}{c_{O_2,0}}. \tag{4.25}$$

The moving boundary condition (Eq. (4.22)) was solved by the front fixing method [111]. A further coordinate system transformation was applied to both domains of the model to solve the moving boundary problem:

$$\xi_I = \frac{\tilde{r}}{\tilde{s}\left(\tilde{z},\tau\right)}, \tag{4.26}$$

$$\xi_{II} = \frac{\tilde{r}-1}{\tilde{s}\left(\tilde{z},\tau\right)-1}. \tag{4.27}$$

In this coordinate system, both ξ_I and ξ_{II} range from 0 to 1. The finite volume method was used to implement the new channel model obtained from from Eq. (4.6), (4.7) and (4.22); we chose this technique since it is a conservative method and therefore it guarantees the mass conservation. The spatial discretization of the PDEs leads to a system of ordinary differential equations (ODEs) which was solved using MATLAB (The MathWorks, Natick, MA), and the function *ode15s* to compute the equations.

Two different type of spatial discretization were used in the model, a linear one along the axial coordinate, by contrast a geometric discretization in the radial direction. Starting from the domain I/domain II interface, the dimensionless width of the mesh i ($\tilde{h}_i$) follows:

$$\tilde{h}_1 = \frac{(1-2^q)}{\left[1-(2^q)^{N_r}\right]}, \tag{4.28}$$

$$\tilde{h}_{i+1} = 2^q \tilde{h}_i, \tag{4.29}$$

where q is a discretization parameter and N_r is the number of mesh in the radial direction. Using this kind of spatial discretization it was possible to locally refine the mesh where the oxygen gradient is steeper, that is at the interface, with a reasonable computational cost. Several simulations were run in order to optimize the mesh size resulting with 10 meshes in the axial direction and 20 meshes in the radial coordinate, for each domain.

The implementation of the moving boundary scheme by means of the front fixing method was validated comparing the numerical solution to the analytical one of the Stefan problem [111]; moreover the model was tested to ensure the conservation of the mass.

4.5 Results

The mathematical model of the three-dimensional bioreactor describes the heterogeneity properties of the system providing the spatiotemporal evolution of several outcomes:

- the effective channel diameter distribution;
- the flow rate partitioning;
- the cell volume (i.e the cell growth);
- the oxygen concentration;

- the shear stress on the cell surface.

First of all we will focus on the single channel results to depict the evolution in time of a simple system like this one, after that the whole model outcomes will be presented where the initial channel distribution is a Gaussian distribution.

4.5.1 Single channel

Figure 4.3 shows the spatiotemporal evolution of the cell volume as changing of the position of the domain I/II interface ($\tilde{s}$) and the oxygen concentration profiles (c) for a 300 µm diameter channel.

The effective diameter, $2\tilde{s}$, decreases from the uniform initial condition of $\tilde{s}_0 = 0.91$ which corresponds to a thickness of domain II equal to 9 % of the channel diameter. The model points out different cell growth rates at different axial positions, resulting in a modifying of the interface line slope line in Fig. 4.3A. The cell domain at the channel inlet ($\tilde{z} = 0$) grows faster than at the channel outlet ($\tilde{z} = 1$). At the steady state, $\tilde{s}$ reaches a uniform value along the z-direction equal to 0.30, which corresponds to a cell thickness of 0.70.

The grayscale maps (Fig. 4.3B and C) represent the dimensionless oxygen concentration in domain II after 1 and 11 days, respectively. Oxygen value is higher near the inlet of the channel, and it decreases along the axial and radial coordinates, it reduces more as domain II is thicker. After 1 day, the cell domain is thicker at the inlet than the outlet section and the minimum oxygen value is about 0.95, while after the 11 days, the cell layer is uniform along the channel and equals 0.70, and the lower oxygen value is about 0.85.

Figures 4.3D and E show the temporal evolution of the oxygen concentration for $\tilde{z} = 0.25$ and $\tilde{z} = 0.9$, respectively. The dashed line in Fig. 4.3D and E denotes the position of domain interface at different time for the two z-sections. In domain II the oxygen concentration is reduced by the cell consumption; the thicker cell domain means lower concentrations not only in this region but also in the center of the channel. Figures 4.3D and E show the oxygen concentration reduction with time and the cell volume growth. At the outlet of the channel (Fig. 4.3E), the concentration is lower than at the inlet (Fig. 4.3D), and the different shape of the dashed lines underlines the difference in cell volume growth as observed in Fig.

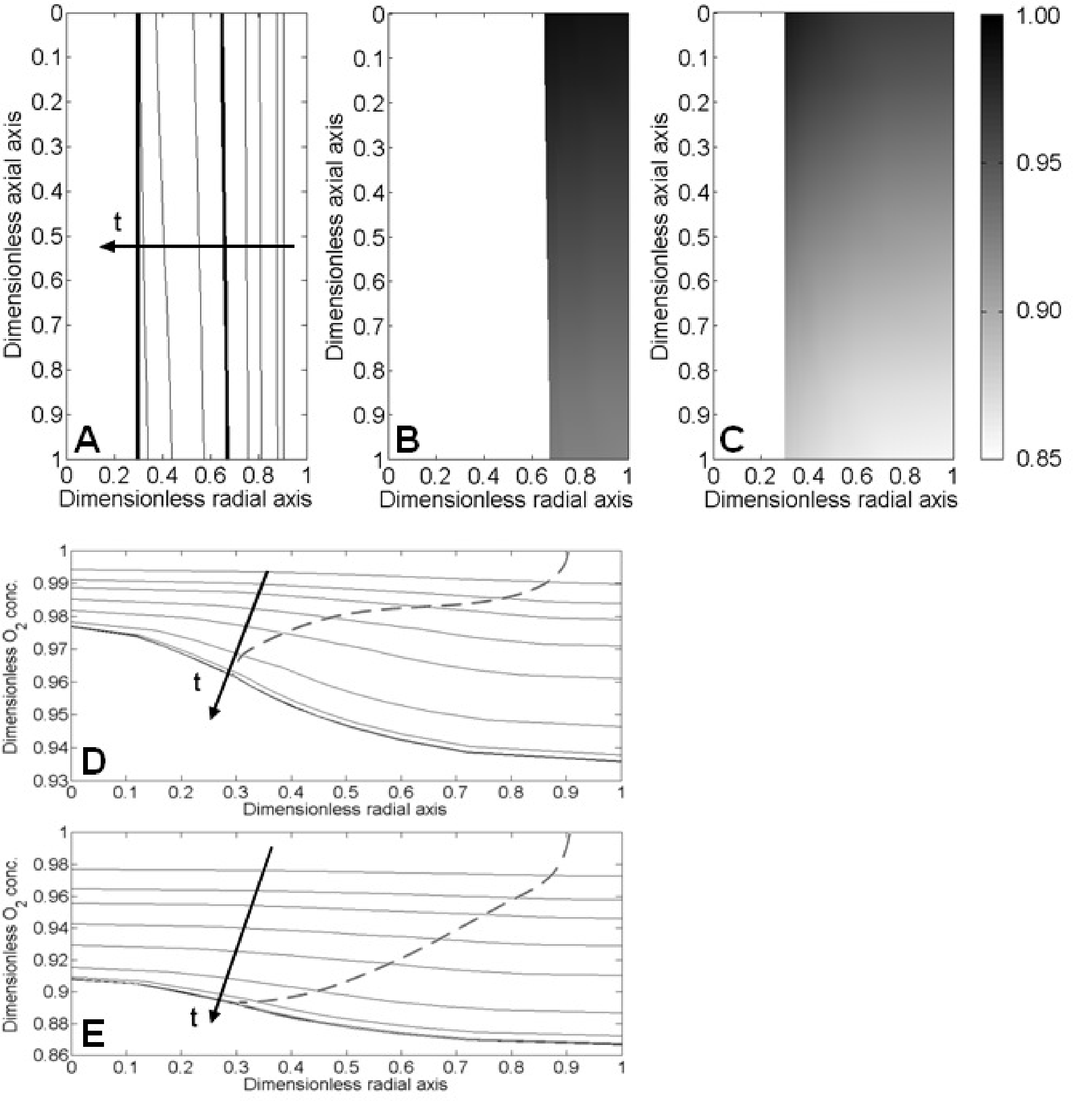

Figure 4.3: Outcomes for a 300 µm diameter channel. (A) Temporal evolution of the domain I/domain II interface in the channel; the bold lines show the interface position at 1 day and at 11 days, the same time reported in (B) and (C). (B,C) Grayscale maps of the oxygen concentration in the cell domain at 1 day (B) and 11 days (C). (D,E) Evolution in time of the normalized oxygen concentration streamline in the radial direction at $\tilde{z} = 0.25$ (D) and $\tilde{z} = 0.9$ (E). Dashed lines depict the position of the domain I/II interface.

4.3A-C. The oxygen concentration is always much higher than the critical value of 0.25, hence the cell growth is inhibited by the shear stress.

4.5.2 Bioreactor

Figures 4.4 and 4.5 show an example of the outputs obtained from the model. In particular a scaffold with a Gaussian channel diameter distribution with mean and variance value equal, respectively, to 2.8×10^{-4} m and 2.5×10^{-9} m^2 [112] was considered. Figure 4.4 shows the evolution in time of the effective channel diameter distribution and the flow rate partitioning. At first, effective diameters (Fig. 4.4A) has a Gaussian distribution (bold dashed line centered in 2.78×10^{-4} m), in time it becomes narrower, then lognormal, and at last, it resembles a bimodal distribution (bold line on the left) with the two modes, the highest centered at 4.7×10^{-5} m, while the second, smaller and wider, at 1.2×10^{-4} m.

Similarly, it is possible to analyze the temporal evolution of the total volumetric flow rate partitioning between channels (Fig. 4.4B). The initial distribution (bold dashed line on the left) is obtained from the Gaussian diameter distribution and it is asymmetric because the flow rate is related to the channel effective diameter through a four power law (Fanning equation). The discontinuity that can be seen for a diameter of 3.8×10^{-4} m in each profile is due to a change of diameter sampling. In channels with a smaller external diameter (less than 3.1×10^{-4} m), the medium flow rate decreases in time approaching almost to zero; on the other hand above this threshold value the flow rate increases. The presence of this threshold value is visible also in Fig. 4.4C, which summarizes the information of the previous two plots, showing the temporal evolution of the effective diameter versus the relative channel flow rate. Each line represents a class of channels defined by the value of the external diameter (D). During the first 4 days, the flow rates are constant in almost all channel classes, while the effective diameters decrease. After this initial trend, channels follow two different evolutions, a first group which effective diameter approaches to a unique value (about 4.7×10^{-5} m) as discussed above for Fig. 4.4A, and the flow rates come closer to zero, as shown in Fig. 4.4B. While a second group of channels hold a higher effective diameter values and at the final time they create a second diameter distribution centered at 1.2×10^{-4} m, as discussed above for Fig.

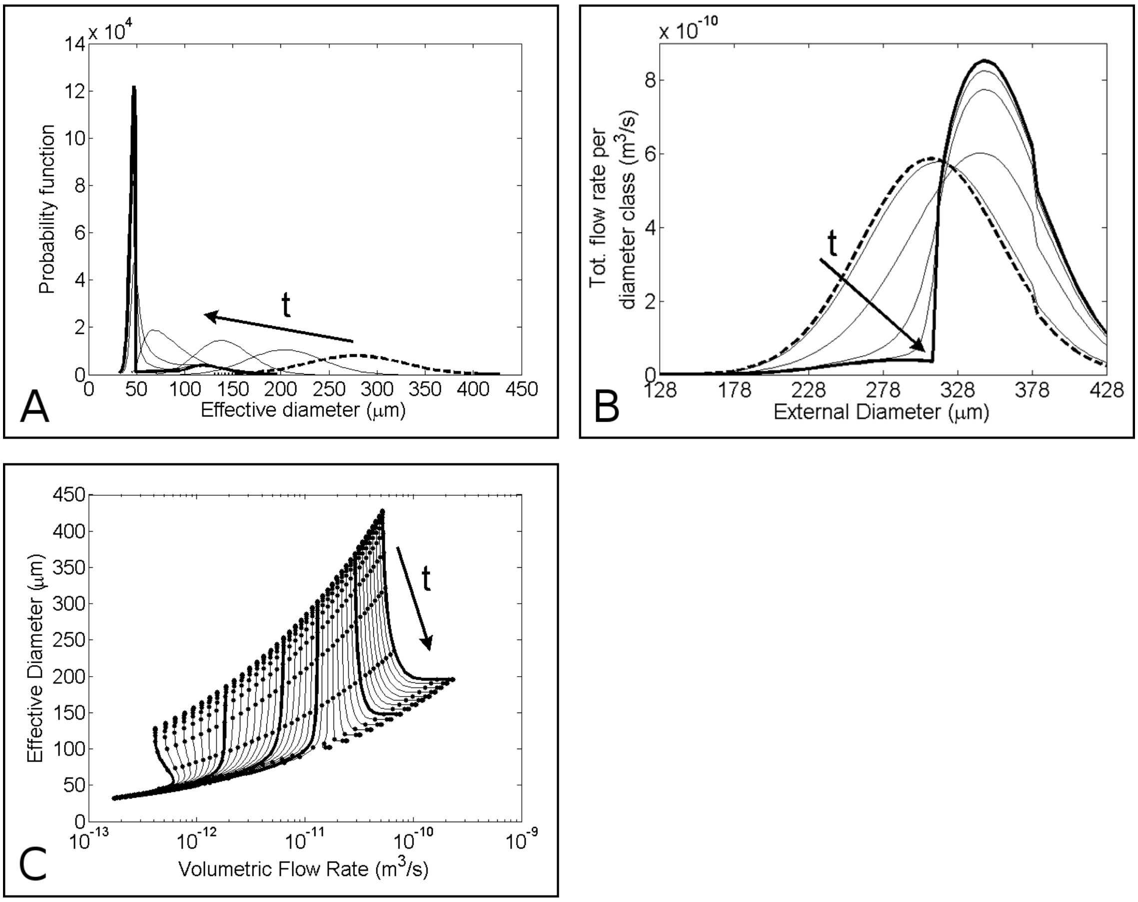

Figure 4.4: Temporal evolution of effective channel diameters and volumetric flow rates in a multichannel scaffold. (A) Probability function of the effective diameters at different time points. Bold dash line represents the initial distribution, and the thicker solid line is the final distribution. (B) Evolution of the volumetric flow rate partitioning per each channel. Bold dash line corresponds to the initial distribution, and the thicker solid line is the final distribution. (C) Temporal evolution of the effective channel diameter versus the volumetric flow rate of that channel. Each line corresponds to a class of channel defined by the external diameter; the top part of the figure denotes the initial condition, while the bottom one denotes the condition at the final time; the points on the lines indicate time steps of 12 h.

4.4A and the flow rates increase, as seen in Fig. 4.4B. The threshold value between these two groups is the class with external diameter equals to 3.1×10^{-4} m.

For each channel, Fig. 4.5 reports data of the average cell volume fraction (Fig. 4.5A), the uniformity of cell growth along the z-direction (Fig. 4.5B), the shear stress on the cells at the inlet (Fig. 4.5C), and the oxygen concentration at outlet (Fig. 4.5D).

In this particular case, the model predicts a cell volume fraction raising in every channel up to a value higher than 0.8 (Fig. 4.5A). The cell volume grows at the same rate in all of the channels until a cell fraction of about 0.45 (points on the line indicate time step of 12 h), after that in the channels with external diameters around 2.5×10^{-4} m the growth rate becomes higher; the steady state is reached earlier and at lower final cell volume fraction in the larger channels. As previously reported in Fig. 4.4A-C, Fig. 4.5A shows once more how the effective diameters of the smaller channels approach to the same value. Figure 4.5A and 4.4 show the cell growth heterogeneity in the whole scaffold system using an effective diameter calculated as the average value along the z-direction. By contrast, Fig. 4.5B shows the variance of the $\tilde{s}$ value along the z-direction in each channel, which represents the heterogeneity along this direction. In this graph, the effective average diameter is plotted versus the absolute value of the difference between $\tilde{s}$ evaluated at the inlet and at the outlet of each channel. At the beginning, it increases and the inlet value is lower than the outlet one. This difference reaches a maximum and then decreases. In the larger channels, the difference reaches almost the zero value at the stationary state; in the smaller channels (e.g., inset in Fig. 4.5B) after a decreasing phase, the difference increases again up to 0.25 at the end of the culture in the smallest channel.

The shear stress on the cell surface was evaluated at the inlet of the channels, since this is the zone where the $\tilde{s}$ is always the minimum of the channel, and thus the shear stress reaches the higher values. The shear stress distribution in time is reported in Fig. 4.5C. The shear stress depends on the flow rate partitioning, and in channels with external diameter greater than 3.1×10^{-4} m, it increases with time overcoming the shear stress limit (dashed line at 0.1 Pa). In addition to the shear stress, oxygen concentration is the other factor that can inhibit the cell growth. Figure 4.5D reports the temporal evolution of the oxygen concentration at the outlet

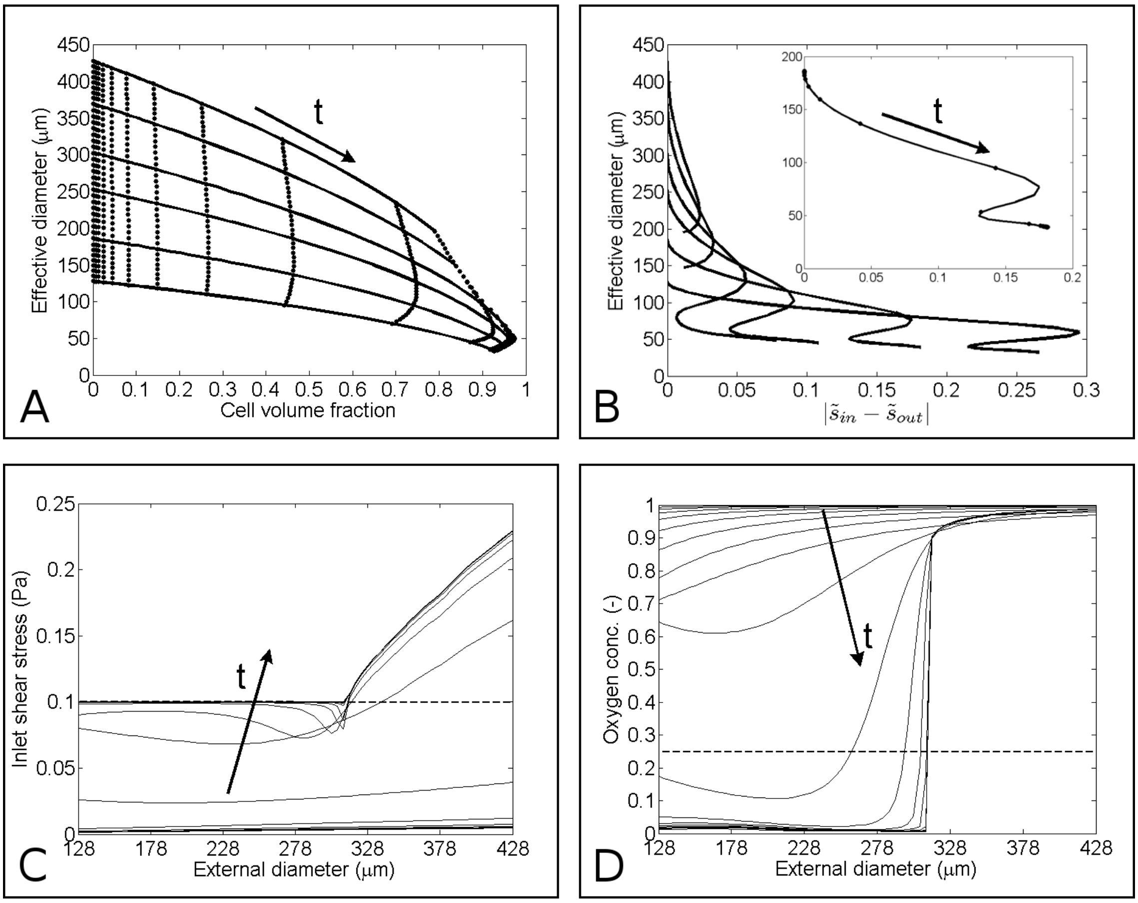

Figure 4.5: Outcomes of a simulation of a multichannel scaffold. The temporal evolution of the effective diameter of different classes of channels is reported versus the cell volume fraction in that channel (A) or versus the absolute value of the difference between $\tilde{s}$ at the inlet and at the outlet of every channel (B). Each line corresponds to a class of channel defined by the external diameter; the left side corresponds to the initial Gaussian distribution, and the points on the lines indicate time steps of 12 h. Inset in (B) shows the temporal evolution of the effective diameter for a channel with small diameter value. Temporal profile of the shear stress evaluated at the inlet of the channels as a function of the external channel diameter; the dash line shows the threshold shear stress value above which it inhibits cell growth (0.1 Pa) (C). Dimensionless oxygen concentration evaluated at the outlet of the channels versus the external diameter and parametric in time; the dashed line indicates the minimum dimensionless oxygen concentration necessary for cell growth ($5.26 \times 10^{-2}\,\mathrm{mol/m^3}$) (D).

of each channel as a function of the external channel diameter. Starting from the initial value (Eq. (4.12) and (4.13)), the oxygen level decreases with time. The decrement is almost negligible in channels greater than $3.1 \times 10^{-4}\,\mathrm{m}$, on the other hand, in the smaller channels the oxygen level drops below the minimum oxygen concentration necessary for the cell growth (dashed line at 0.25), reaching values close to zero.

Sensitivity analysis on the model parameters was performed showing that the presented results are quite insensitive to the parameters. For instance, a 100 % variation of the cell growth kinetic constant k_{cell} or the maximal oxygen consumption rate Q_m induces a change in the mean cell volume fraction of about 4 % and 1 %, respectively, without modifying the general trend.

Analysis of the effect of operative variables on the cell growth was studied, in particular the diameter variance and the medium flow rate were taken into account (results are reported in appendix B). Briefly, changing the diameter distribution (i.e. variance), the mean cell volume fraction is not sensible affected, nevertheless the dispersion, that is the difference between the highest and the lowest cell volume is enhanced, increasing the variance value of the Gaussian distribution. In contrast, the medium flow rate highly affects the cell growth heterogeneity, indeed at low flow rate cells grow slowly and they are mainly inhibited by the lack of oxygen resulting in a uniform, but low cell volume fraction at the final time. While, at high flow rate, the cell growth is characterized by a high heterogeneity (cell volume ranges from 0.1 to about 1) due to the effect of both inhibitor factors. In particular in the bigger channels the growth stops only because of a shear stress higher than the threshold limit. On the other hand, in the smaller channels, both a shear stress equals to the limit and an oxygen concentration equals to zero inhibit the cell growth. Between these two limit cases an optimum flow rate value can be found in order to obtain a high and uniform cell fraction.

4.6 Applications

The developed mathematical model was applied to the two different cases, the *in vitro* differentiation of hepatic precursor cells and the cell growth of C2C12 muscle cell. In particular, the operative conditions for hepatic precursor cell culture were optimized through model simulations, whereas muscle cell line C2C12 culture experiment was setup for validating the mathematical model.

4.6.1 Optimization of the experimental conditions for hepatic precursor cell culture

The model was used for rationalize the precursor liver cells culture in a 3D perfusion bioreactor. The model supported the design of an optimal experimental plan to improve the differentiation of adult precursor liver cells to mature hepatic cells.

In this work, the mathematical model was applied to optimize the medium flow rate in order to obtain a high and uniform cell fraction within the 3D scaffold maintaining an oxygen concentration greater than the threshold value for avoiding growth inhibition due to the formation of hypoxic region. In particular, a single channel model was used considering the average channel diameter of the scaffold and its flow rate. Simulations were run changing the flow rate to determine the optimum; three values were studied, 0.1 mL /min, 0.5 mL /min and 2.5 mL /min.

All these conditions ensure an oxygen level above the limit value through the channel (see Appendix A), however, the flow rate equals to 0.1 mL /min should be considered the lower limit because in this case the oxygen level at the outlet almost reaches the threshold oxygen concentration. Figure 4.6 shows the effect of the flow rate on the cell growth and heterogeneity. At low values, cells reach higher density,

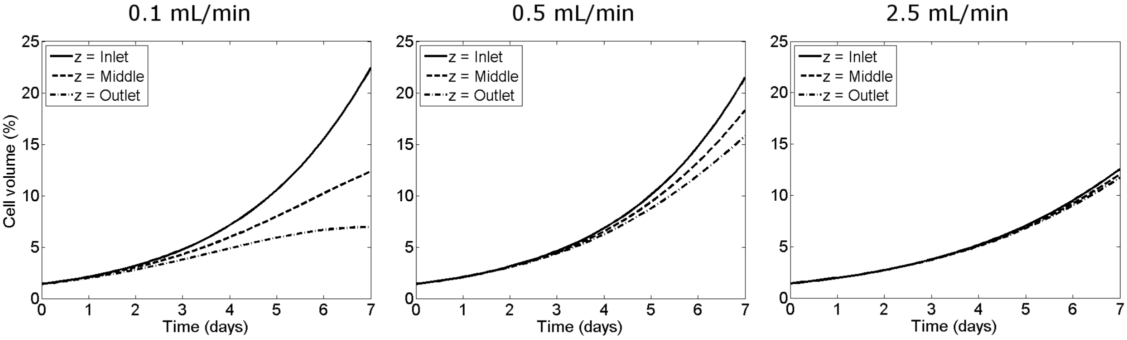

Figure 4.6: Time variation of the percentage of cell volume. Data are given for three flow rates: 0.1 mL /min (left), 0.5 mL /min (center), 2.5 mL /min (right). Each graph shows the data for three z-coordinates, that is at the channel inlet (continuous line), midline (dashed line), and outlet (dashed and dotted line).

especially at the inlet of the channel, nevertheless the growth is heterogeneous, in fact the cell volume percentage at the inlet of the channel is three times bigger than the outlet. On the other hand, increasing the flow rates ensures a uniform cell growth, but at lower values. In conclusion flow rate equals to 0.5 mL /min is the optimal value since it guarantees high and uniform cell volume fraction.

These results were used to design an optimal experimental plan for developing an efficient differentiation method of adult precursor liver cells to mature hepatic cells. Complete discussion of this research is reported in Appendix A; these results are published by Carraro et al. [113].

4.6.2 Validation of the mathematical model using murine skeletal muscle cell line C2C12

A three-dimensional C2C12 cell culture in a perfusion bioreactor was used for validating the mathematical model; the cell growth and its distribution in the porous scaffold were considered.

The experimental device used for the model validation is the perfusion bioreactor described in chapter 2 with recirculation of cell media. In the original configuration [76] (Fig. 4.7A), inside the chamber is allocated a perforated PDMS (polydimethylsiloxane) holder which holds the scaffold; medium was forced to flow inside the hole through the construct. The adhesion between PDMS and the chamber is guaranteed by a Teflon film placed at the bottom of the culture chamber, nevertheless, if

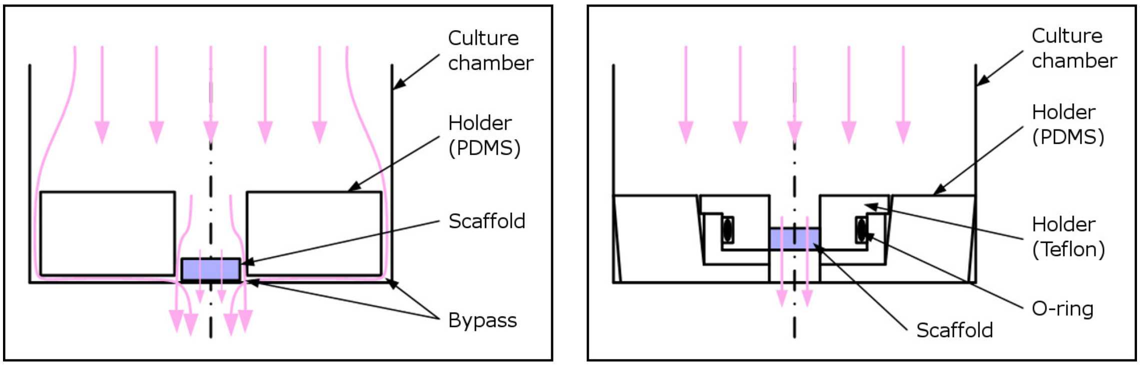

Figure 4.7: Longitudinal section of the bioreactor culture chamber. (A) Original configuration, (B) New configuration.

the holder or the scaffold are not well positioned, medium bypass can occur. To fix this problem, a new culture chamber setup was developed (Fig. 4.7B). In this new configuration, the scaffold is inserted into a removable Teflon holder and it is sealed with an O-ring. This holder is held in place by a PDMS holder with a cone shape in order to ensure the adhesion to the culture chamber.

Figure 4.8 shows a scaffold cross section after 7 days of culture with the new chamber configuration, cell nuclei were dyed with Hoechst 33342. It presents almost a uniform cell distribution in the whole section, although there is a small region at the periphery with a high cell density. In addition, this new setup facilitates the operation of insertion and extraction of the scaffold.

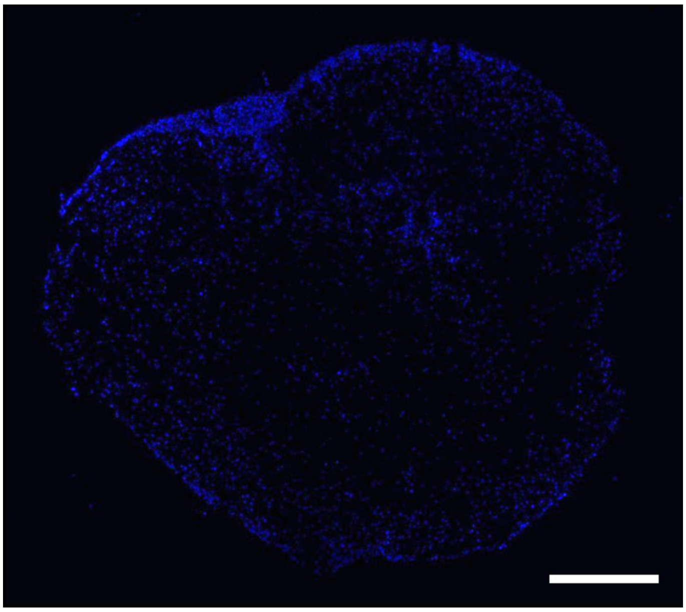

Figure 4.8: Cross section of the scaffold after 7 days of culture in the bioreactor. Nuclei are counterstained with Hoechst. Scale bars 1 mm.

For validating the mathematical model, C2C12 cells were cultured in the perfusion bioreactor; cells were seeded on each scaffold with a cell density equals to 5×10^5 cells /scaffold, and cell media was pumped at a flow rate of 0.65 mL /min for 7 days. At every time step, that is day 0, 2, 4 and 7, two scaffolds were collected and frozen for the cell count. Cell analysis were performed with Hoechst 33342 as reported in chapter 2, three values were measured for each scaffold:

- the total number of cells;

- the cell distribution for the top, the middle and the bottom region;
- the cell distribution along the height of the scaffold.

Using the last type of data at the initial time as input for the model, a simulation was run to compare its results with the experimental data. Figure 4.9 shows the cell distribution (as number of cells for each channel class) in the scaffold middle section at the final time. The blue bars represent the experimental data with their standard deviation, while the green line is the data obtained from the simulation using all the proper parameters for this case. As shown, the model well represents the experimental data both in term of number of cells and in term of cell distribution.

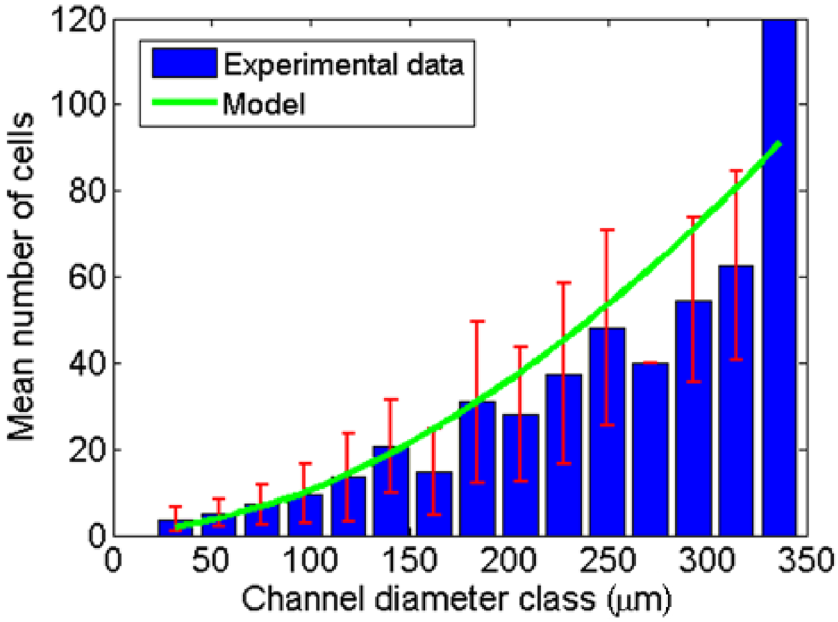

Figure 4.9: Comparison between the experimental data (blue bars) with the model data (green line) for the cell heterogeneity for the middle section of the scaffold after 7 days of culture in the perfusion bioreactor

The development of the mathematical model is published by Flaibani et al. [41], while the experimental validation is in preparation for the submission.

4.7 Conclusions

In this chapter, a mathematical model of the cell growth in a three-dimensional porous scaffold in a perfusion bioreactor was developed. In particular, we focused on the cell volume fraction evolution in time and its degree of heterogeneity in a porous scaffold with a known pore size distribution. The cell microenvironment controls the cell fate, such as the cell metabolism and the cell growth [100, 104] and there are not any techniques to monitor the local properties of a 3D cell culture. Therefore a mathematical model which can predict these properties and their spatial and temporal profile is necessary to estimate how the operative conditions affect the cell growth and to achieve a uniform 3D cell culture. In particular, we studied the effect of the oxygen on the cell growth since it has a great influence on the cell culture [39].

The model provides information on the temporal evolution of the microscopic variables of the system and their distribution inside each channel in the radial and axial direction. Moreover, the model takes into account the cell growth inhibition due to chemical and/or mechanical stimuli, such as the oxygen concentration and the shear stress imposed on the cell surface.

The mathematical model was applied in two different cases, for the hepatic precursor cells culture and for C2C12 cells culture. In the former it was used in order to optimize the operative conditions, in particular we focused on the medium flow rate to ensures a high oxygen level inside the scaffold and a uniform cell proliferation. In the second case a C2C12 culture was carried out for validating the model; at every time step scaffolds were taken from the culture chamber to perform the cell analysis. The comparison between the experimental data and the simulation outcomes shows that the model is able to predict the cell growth heterogeneity as function of the operative variables.

At last the model can be adapted to different cell types or other molecules, since it has been written in a generic form. For example it could be used to study the effect of endogenous and exogenous factors in the microenvironment on the cell processes.

5

Cell signaling model in a perfusion three-dimensional bioreactor

In this chapter we will use the model framework developed in chapter 4 for studying the cell response to an exogenous stimulation, we focused on the influence of an insulin stimulation to the cell glucose metabolism. The insulin signaling pathways was analyzed and it was coupled with the previous cell growth model for describing the cell signaling in a cell culture system.

5.1 Introduction

The possibility of obtaining *in vitro* 3D cell culture model which can reproduce the *in vivo* physiology is becoming of paramount importance for assisting the process of drug development and drug screening.

Three-dimensional cell culture systems are characterized by high complexity [101], indeed they require a spatial organization, spatially and temporally controlled stimuli such as all the biological, chemical, mechanical cues must be provided to the cells for controlling their fate.

In vitro cell models are commonly used as step for therapy discovery program because they allow to perform low cost and quick experiments, moreover high-throughput analysis can be carried out. However this approach could not describe the response of a complex functional tissue due to the lack of structural and topological cues, the different of chemical and mechanical properties and the not controlled spatio-temporal combination of soluble factors in a conventional cell culture systems [114]. The other type of models, the animal models (spontaneous, induced or transgenic), are not able to represent human biology, cannot guarantee the efficiency of drug on human models, and experimentations are time consuming with usually highly sophisticated and costly procedure for the maintenance of animals. Thus there is a need of "something between a Petri dish and a mouse", to represent a cell environment in a living organism and to be more predictive of *in vivo* systems [115]. An *ex vivo* tissue culture model could be an intermediate approach which resembles the complexity of an *in vivo* physiology and at the same time the achievement of this experiment is as easy as a standard cell culture.

A rational understanding of the correlation between the experimental conditions, the cell microenvironment and therefore the cell response is important for accurately investigate biological problems, and, furthermore for the experiment optimization.

Several models that describe the pathways related to signal transduction have been developed. Most of them focus on specific steps of the whole signaling, for example the insulin receptor binding kinetics [116–118], protein kinase cascade [119, 120] and GLUT4 translocation [121, 122]. In addition, models which study the diffusion of protein kinases and intracellular enzymes during signaling transduction have been developed [123]. Nevertheless there are only a few insulin signaling models which describe the system beginning from the binding of the insulin to its receptor until the translocation of GLUT4, the most used is the model proposed by Sedaghat et al. [15]. This particular signaling model has been applied for studying its interaction with other pathways [124, 125] or for analyzing the effect of the insulin signaling of the whole-body blood glucose regulation system [126, 127]. These whole-body models although, does not consider the *in vivo* mass transport of molecules and their fluid dynamics, and the different time and spatial scales that characterized each subsystem.

In this project, we aimed to study the intracellular response of a three-dimensional cell culture in a perfusion bioreactor to an insulin stimulation. All the phenomena which occur at a bioreactor level have lengths scale and characteristic times which are different from those that characterized the intracellular insulin processes. Therefore to analyze such system from the macroscopic scale to the single cell level, we must also model the signaling pathways and subsequently couple it with the mass transport model in order to (a) describe the effect of the system heterogeneity on the insulin signaling pathways and on the glucose consumption rate, (b) determine if the cell response is experimentally measurable, and (c) detect which are the variables that most affect the signal transduction cascade.

Glucose was considered along with the insulin because it plays an important role in the cell processes and most importantly it is involved in metabolic disorder such as type 2 diabetes mellitus [128, 129]. Such model could be a fundamental step for the understanding of the physiology of this disease. Having a tool that predicts the biological response to an insulin stimulation of both healthy and diabetic patient can be used to characterized tissues and therefore determine the optimal experimental conditions with a view to perform drug screening tests.

5.2 Multiscale theoretical framework

Before defining the theoretical framework, a brief description of three-dimensional cell culture in perfusion bioreactor (Fig. 5.1) follows. Medium flows through the scaffold from the top to the bottom and its geometry was simplified by reducing the interconnected pores network to a bundle of parallel, stream-flow oriented, cylindrical channels with a defined channel diameter distribution. In each channel, cells

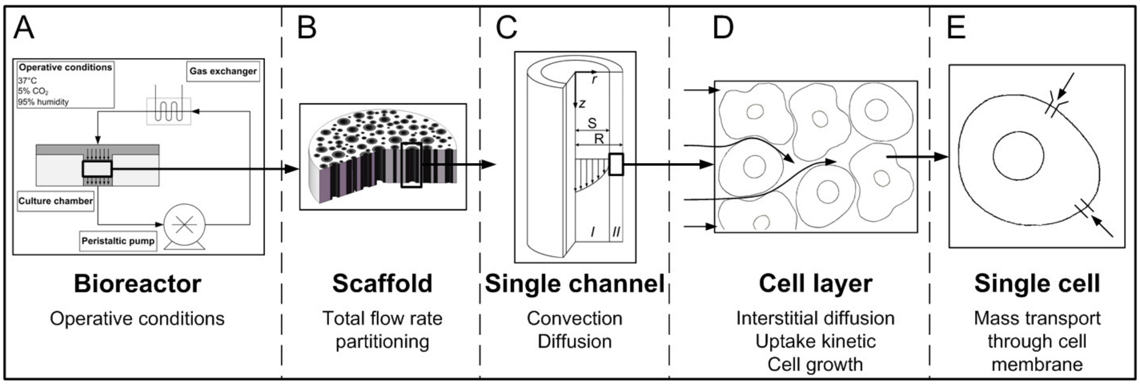

Figure 5.1: Representative scheme of multiscale mass transport between bioreactor and single cell.

adhere at the inner wall creating a continuous and uniform layer, so there are two regions, the medium and the cell domain, respectively at the center and at the wall of the channel. The cell media flows in the center and the mass transport of all the molecules, such as nutrients, metabolites, oxygen, waste products is governed by axial convection and radial diffusion; because of the concentration gradient between the two domains, there is a flux of molecules toward the interface medium/cell domain. In the latter, the mass transport is governed by the interstitial diffusion, then substances are internalized and consumed by cell metabolism. When insulin is internalized it triggers its signaling pathways (Fig. 5.2).

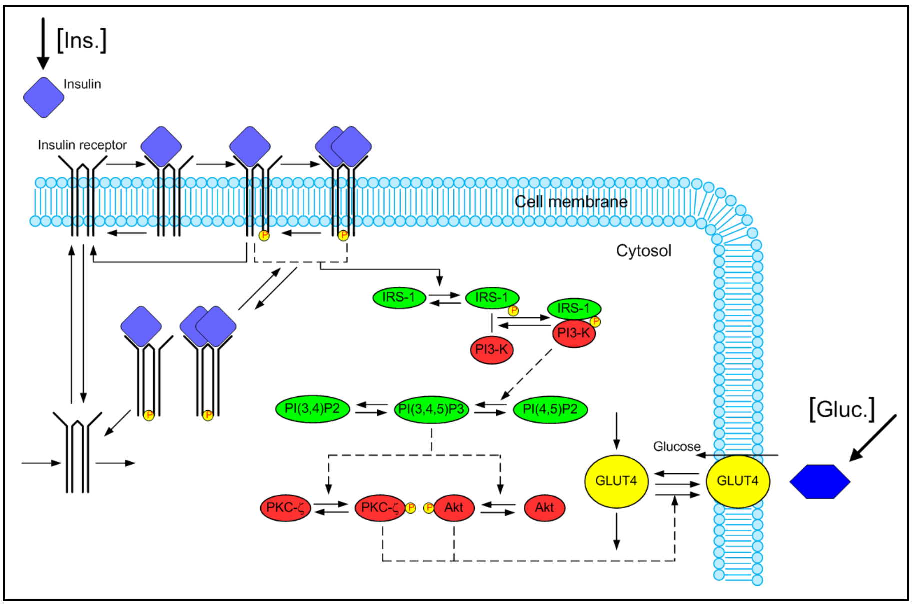

Figure 5.2: Kinetic framework, insulin signaling pathways without feedback, adapted from Sedaghat et al. [15]. The bold arrows represent insulin and glucose outcomes from the mass transport model.

Insulin receptors, on the cell membrane, bind one or two molecules of insulin, hence both once- and twice-bound phosphorylated receptors phosphorylate IRS-1, which then binds and activates PI 3-kinase. Consequently activated PI 3-kinase converts the substrate phosphatidylinositol 4,5-bisphosphate [PI(4,5)P2] to the product PI(3,4,5)P3, which promotes the activation of the downstream reactions, that is the serine/threonine protein kinase (Akt) and PKC-ζ. The final reactions involve the GLUT4 translocation. Under basal conditions it recycles between an intracellular compartment and the cell surface, on the other hand, on insulin stimulation, there is an increase of GLUT4 trafficking from the cytosol to the membrane. It is explained by the presence of a separate pool of intracellular GLUT4 recruited to the cell surface, this raise is a linear function of the metabolic effect produced by phosphorylated Akt and PKC-ζ. Since the glucose consumption rate is mediated by the cell surface GLUT4, and an inward insulin flux promotes the translocation of the protein from the cytosol to the cell membrane, it is straightforward that the increasing of GLUT4m raises the flux of glucose internalization and therefore the glucose uptake.

5.2.1 Bioreactor model

All the assumptions necessary to model this system have been described in chapter 4, where the oxygen mass transport was analyzed. In this model we also studied other molecules, that is glucose and insulin which have different experimental conditions compare to the oxygen, in particular the inlet conditions. Indeed oxygen is always in equilibrium with the incubator atmosphere thanks to the gas exchanger and its concentration is calculated taking into account of its composition [32]. The oxygen concentration in the incubator is reduced by both the supplemental carbon dioxide (CO_2 at 5 %) and water vapor (95 % RH) [130]; this conditions yield p_{O_2} values of 142 Torr. Oxygen is slightly less soluble in tissue culture medium than water, reported at 1.29 nmol /(cm^3 Torr) at 37 °C in DMEM [131]. The product of this solubility coefficient and p_{O_2} gives the boundary conditions for dissolved O_2 in the model.

Glucose inlet concentration depends on the bioreactor configuration; for an open configuration it means that scaffold is always perfused by fresh media and therefore the glucose level equals the physiological condition, on the other hand for a closed configuration, without make up of medium, glucose decreases in time as a function of the cell metabolism.

At last, insulin has a defined profile as function of time since it is a stimulus fixed by the experimental plan.

The mathematical bioreactor model will be describe in two main parts: mass transport model and kinetic model.

5.2.1.1 Mass transport model

In this section we will present an upgraded version of the single channel model to include all the species, where all the assumptions made in chapter 4 are still reasonable.

The system was described considering adipose cell since the signaling model was developed for this cell type, however it has been used for studying muscle cell [127].

As previously reported, the governing equations for the medium (domain I) and for cell (domain II) domain were solved in the range $0 \leq r < S\left(z,t\right)$ and $S\left(z,t\right) \leq r \leq R$, respectively, with $S\left(z,t\right)$ the medium/cell interface and R the channel radius. In domain I and II the 2D mass balances follow:

$$\frac{\partial c_i^I}{\partial t} = -\left[\frac{1}{r}\frac{\partial}{\partial r}\left(rN_{i,r}^I\right)\right] - v_z\left(r,t\right)\frac{\partial c_i^I}{\partial z}, \tag{5.1}$$

$$\frac{\partial c_i^{II}}{\partial t} = -\left[\frac{1}{r}\frac{\partial}{\partial r}\left(rN_{i,r}^{II}\right)\right] + R_i. \tag{5.2}$$

Where the subscript i stands for oxygen, glucose and insulin, $N_{i,r}$ is the diffusive molar flux in the radial direction, v_z is the axial medium velocity and R_i is the i-species uptake rate. In both Eqs. (5.1) and (5.2) the radial diffusive molar fluxes were expressed by Fick's law [108] and the axial velocity by the Hagen-Poiseuille equation [108]. The rate of consumption of oxygen and glucose were described using data from literature [58, 132] and they are reported, respectively, by Eqs. (5.3) and (5.4):

$$R_{O_2} = -\frac{1}{\tilde{v}_{cell}}\frac{V_{m,O_2}c_{O_2}^{II}}{K_{m,O_2} + c_{O_2}^{II}}, \tag{5.3}$$

$$R_G = -\left(\frac{GLUT4m}{GLUT4m|_{basal}}\right)\left(\frac{1}{\tilde{v}_{cell}}\frac{V_{m,G}c_G^{II}}{K_{m,G} + c_G^{II}}\right). \tag{5.4}$$

Where $\tilde{v}_{cell}$ is the cell specific volume, V_m is the maximal species consumption rate and K_m is the concentration at half-maximal consumption, for both species. $GLUT4m$ is the percentage of protein on cell surface, $GLUT4m|_{basal}$ is the percentage of protein on cell surface at basal condition, that is without insulin stimulation. These two variables are outcomes of the insulin signaling model and their ratio represents the increment of the glucose consumption rate due to the raise of cell surface GLUT4 expressed by cells after an insulin perturbation. A linear dependence of glucose metabolism from cell surface GLUT4 was assumed [15]. By contrast the insulin depletion due to the insulin signaling internalization is negligible compare to the total amount which enters in the system.

Eqs. (5.1) and (5.2) were solved respect to c_i^I and c_i^{II} along with the insulin signaling model (see Appendix C for details), the boundary conditions in the radial direction are equals to those reported in chapter 4, that is symmetry at the center of the channel, insulation at the channel wall and balance of fluxes at domain I/II interface. The channel inlet conditions ($z = 0$) depend on the metabolites; it is a Dirichlet boundary condition for oxygen (Eq. (5.5)):

$$c_{O_2}^I\,(r, z, t) = c_{O_2,0} \qquad\qquad z = 0, \tag{5.5}$$

where $c_{O_2,0}$ is the oxygen concentration in equilibrium with the incubator atmosphere. Regarding glucose, its inlet condition is determined by the bioreactor configuration: without recirculation or with recirculation. The former brings to a Dirichlet boundary condition like oxygen expressed by Eq (5.6):

$$c_{Glu}^I\,(r, z, t) = c_{Glu}^{phys} \qquad\qquad z = 0, \tag{5.6}$$

where c_{Glu}^{phys} is the glucose concentration in the cell media. On the other hand with recirculation (without glucose make up), glucose decreases in time because of the total cell metabolism (Eq. (5.7)):

$$\frac{dc_{Glu}^I\,(r, z, t)}{dt} = \frac{1}{V_{holdup}} \int_{V_R} R_G\, dV_R \qquad\qquad z = 0, \tag{5.7}$$

In Eq. (5.7), V_{holdup} id the holdup bioreactor volume and V_R is the reaction volume, i.e. the total cell volume. The inlet insulin concentration is given by the stimulus, for example, with a pulse perturbation ($t_2 - t_1$) long as described by Sedaghat et al. [15], the condition follows:

$$c_{Ins}^{I}\left(r,z,t\right):\begin{cases} c_{Ins,0}, & \text{if } t_1 \le t \le t_2, \\ 0, & \text{otherwise.} \end{cases} \qquad z=0, \tag{5.8}$$

In Eq. (5.8), $c_{Ins,0}$ is the intensity of the perturbation, that is the concentration of the insulin solution used to stimulate the system. The initial conditions ($t = t_{in}$) for the oxygen and glucose is a uniform concentration in the whole system (Eq. (5.9)):

$$c_i^{I}\left(r,z,t\right) = c_i^{II}\left(r,z,t\right) = c_{i,0} \qquad t = t_{in}, \tag{5.9}$$

where $c_{i,0}$ is the the oxygen concentration in equilibrium with incubator atmosphere for oxygen continuity equation; and the glucose concentration in fresh medium for glucose continuity equation. Initial condition for insulin must be consistent with the boundary condition, therefore, since $t_1 > 1$ in most cases, it gives (Eq. (5.10)):

$$c_{Ins}^{I}\left(r,z,t_{in}\right) = c_{Ins}^{II}\left(r,z,t\right) = 0 \qquad t = t_{in}. \tag{5.10}$$

To solve the system of equation defined by Eqs. (5.1)-(5.2) for each i-species, these equations must be coupled with the cell growth equation for describing the temporal displacement of the domain I/domain II interface. The cell growth is defined by a Monod expression [99]:

$$\frac{dn}{dt} = R_{cell}\left(z,t\right), \tag{5.11}$$

$$R_{cell} = F_{damp}\mu n = F_{damp}\mu_{max}\frac{c_{O_2}^{II}}{K + c_{O_2}^{II}}n. \tag{5.12}$$

In Eqs. (5.11) and (5.12), n is the number of cells, R_{cell} is the cell growth rate, F_{damp} is a damping function, μ is the specific growth rate and μ_{max} is the maximum growth rate, K is the half-saturation coefficient. As reported in chapter 4, the damping function takes into account the cell growth inhibition effect of low oxygen concentration. The kinetic decreases once the oxygen concentration approaches the limit value, when it is reached the growth stops. In this system the shear stress inhibition was not considered since the adipose cell growth rate is slow compare to an experiment duration of 24 h (the doubling time equals about 240 hours [133]. The damping function has been defined as:

$$F_{damp} = \frac{1}{2}\left\{1 + \tanh\left[k_{damp}\left(c^{II}_{O_2} - c^{lim}_{O_2}\right)\right]\right\} \tag{5.13}$$

Similarly to what has been done in chapter 4, Eqs. (5.11) and (5.12) were rearrange to obtain the time profile of the interface displacement (Eq. (5.14)):

$$\frac{dS}{dt} = -\frac{\mu_{max}}{S\left(z,t\right)}\int_{S(z,t)}^{R}\frac{F_{damp}c^{II}_{O_2}}{K + c^{II}_{O_2}} r\, dr. \tag{5.14}$$

Eq. (5.11) satisfies the given initial condition ($n\left(z, t_{in}\right) = n_0\left(z,\right)$), hence the initial number of cells is converted in the interface position:

$$S\left(z,t\right) = S_0\left(z\right) \qquad\qquad t = t_{in}, \tag{5.15}$$

where $S_0\left(z\right)$ is the initial domain I/domain II interface position as function of the axial coordinate. Following the procedure showed in chapter 4 the whole model was rewritten in dimensionless form before its implementation and resolution in MATLAB (The MathWorks, Natick, MA).

5.2.2 Kinetic insulin signaling pathways model

One of the most mechanistically detailed model of the insulin signaling pathways that can be find in literature was developed by Sedaghat et al. [15]. Two variations of the model were proposed by the authors, one without the feedback mechanisms and one with feedback. Ordinary differential equations, derived using the mass-action principles, were used to describe the time-varying concentration of the state variables. The model with feedback mechanisms is more detailed and better fits the experimental data showed by the authors [15], nevertheless we utilized the one without feedback. The latter one was used because it is easier to implement and its numerical resolution is faster; moreover the error introduced with this approximated model does not strongly affect the cell surface GLUT4 determination giving an average error equals to 8.5 %, as depicted in Fig. 5.3. In this project we mainly

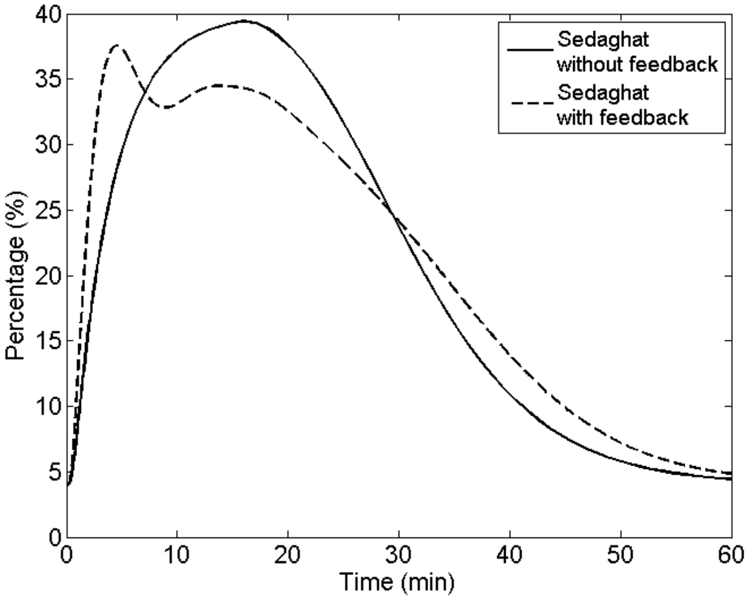

Figure 5.3: Comparison in the temporal GLUT4m profile between the two model reported by [15].

focused on the GLUT4m, which is the most important outcome of the signaling model since its temporal profile affects the glucose consumption rate.

5.2.2.1 Model reduction

Before coupling the bioreactor model with the cell signaling model, the insulin pathways has been analyzed to reduce its order and therefore its complexity, obtaining a new version which preserves its input-output behavior while reducing the computational costs. The Sedaghat [15] model has been simplified using the following assumptions:

- the production and degradation of receptors, specifically for insulin and glucose receptor, were not considered because they are slow processes [134] compare to the signaling process;
- it is reasonable considering the conservation of the total amount of proteins [134], such as insulin receptor (IR), insulin receptor substrate-1 (IRS-1), phosphatidylinositide 3-kinase (PI 3-kinase), phosphatidylinositol bi/tri-sphosphates, Akt, protein kinase C (PKC-ζ), glucose transporter type 4 (GLUT4);

- the dependency of original kinetic parameters from state variables was removed.

The first hypothesis allowed to neglect the production and degradation of insulin and glucose receptor as showed in Fig. 5.4. The second hypothesis allowed to replace 7 ordinary differential equations with so many algebraic equations. The third simplification involved a modification of 4 parameters introduced by Sedaghat et al. [15], hence Eqs. (C.9)-(C.13) have been modified.

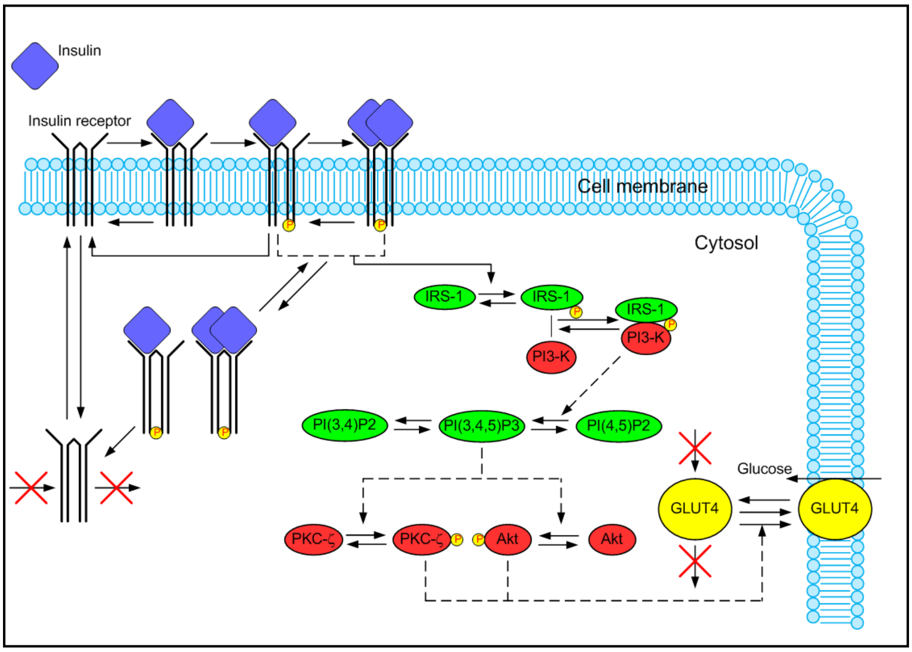

Figure 5.4: Modifications (red crosses) of the insulin signaling pathways model after the model reduction.

The reduced model was compared with the original one (Fig. 5.5), in particular the cell surface GLUT4 was taken into account; its temporal profile evaluated with the new model closely represents the original data with an average error equals to 0.3 %. Thanks to the model reduction approach, the new system of equations is composed of 13 ordinary differential equations and 7 algebraic equations, while the Sedaghat model is composed of 20 ordinary differential equations. All the equations of the simplified insulin signaling pathways model are listed in Appendix C.

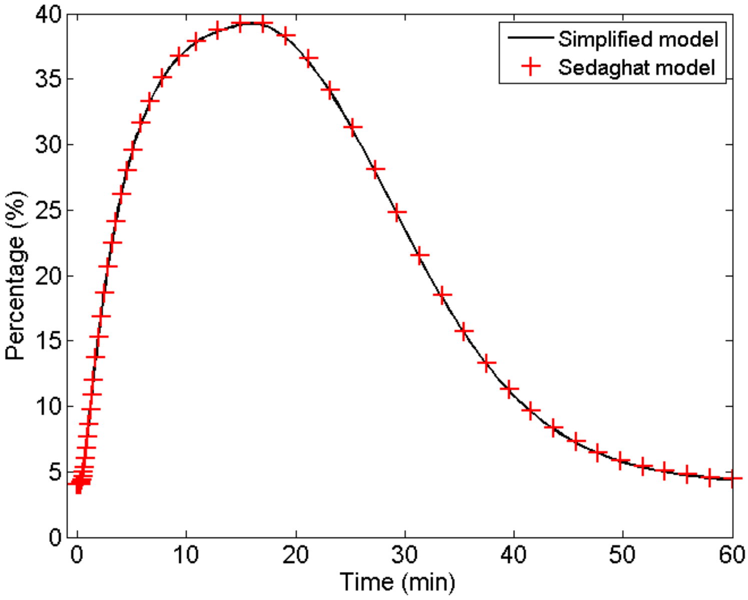

Figure 5.5: Comparison between original and simplified model outcome for cell surface GLUT4.

5.3 Results

In this section the results will be presented; first of all, the single cell and the single channel model will be compared to show the difference between these two elementary systems. Secondly the whole bioreactor will be analyzed focusing both on the macroscopic outcomes and on the cell microenvironment properties distribution.

5.3.1 Comparison between single cell and single channel model

Signaling model are usually developed to describe the complex networks involved in the intracellular processes such as metabolism, proliferation, apoptosis and the interactions between different pathways. In this work we applied an already developed signaling model to a bioreactor model, that is a fluid dynamics and mass transport model, because we wanted to analyzed the mass transport effect on the cell processes and fate. First of all the difference between a single cell and a single channel will presented reminding that the latter is the fundamental unit in the bioreactor model. Although the insulin signaling pathways model describes up to 20 species, only the most important for this work will be presented, that is the insulin and the cell surface GLUT4 concentration profile.

In the single cell system, once the insulin stimulus is defined by the duration and the concentration (Fig. 5.6A), it is the value the cell are exposed to and which triggers the pathways.

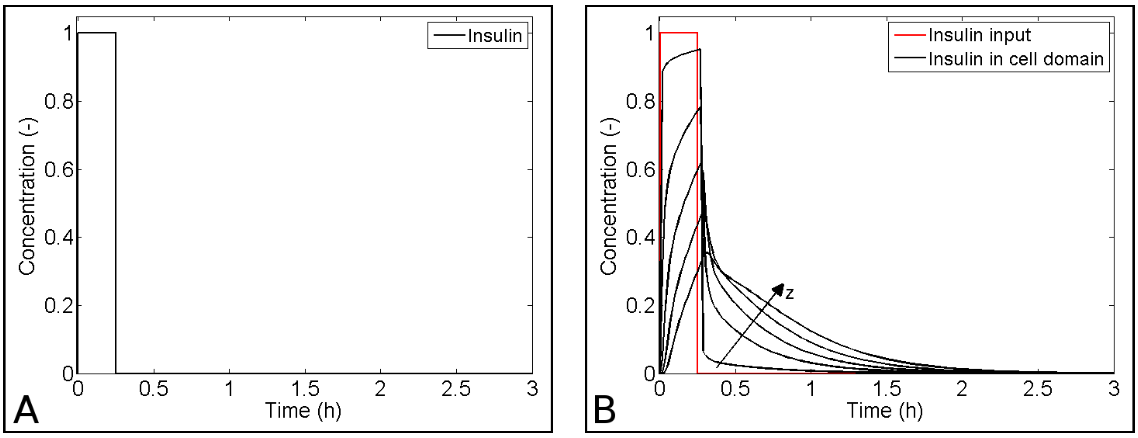

Figure 5.6: Comparison of the temporal insulin profile in the single cell (A) and single channel (B) system.

In the channel system (Fig. 5.6B), the insulin signal has a delay along the channel, this means that the original pulse stimulus becomes a wide distribution with lower intensity along the axial coordinate.

This modification affects all the signal transduction, in fact for the single cell there is a well defined cell surface GLUT4 profile which transient lasts about 1 h (Fig. 5.7A). While in the single channel the GLUT4m profile marginally depends on the axial coordinate (Fig. 5.7B). Even though the maximum concentration peak is the same as in the single cell (40 %), the temporal evolution is different. In all sections the transient is more than 3 h long; it quickly reaches the maximum value in about 15 minutes and then it slowly decreases to return to its basal condition. The profiles are quite similar in all sections, except for the inlet (dashed line) which lasts longer because it was subjected to a higher concentration (Fig. 5.7B), similar to the original pulse.

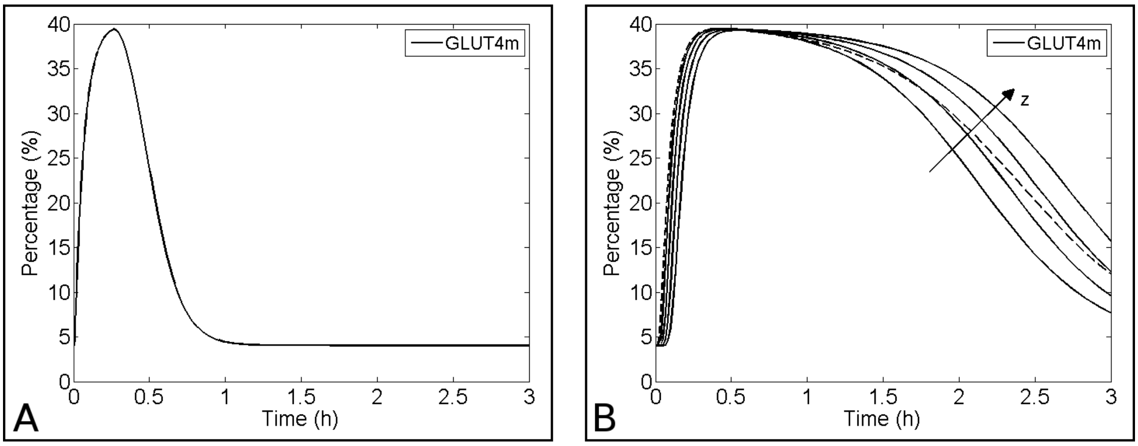

Figure 5.7: Comparison of the temporal cell surface GLUT4 profile in the single cell (A) and single channel (B) system.

5.3.2 Spatial evolution of the single channel system

In the single channel system the spatiotemporal species distribution can be obtained. In this case we considered the concentration of four variables: insulin, glucose, phosphorylated insulin receptor and cell surface GLUT4 (Fig. 5.8). After the stimulation, along the channel axis, Figure 5.8A shows a decreasing insulin profile, because of the operative conditions medium has a high residence time (about 1 h),

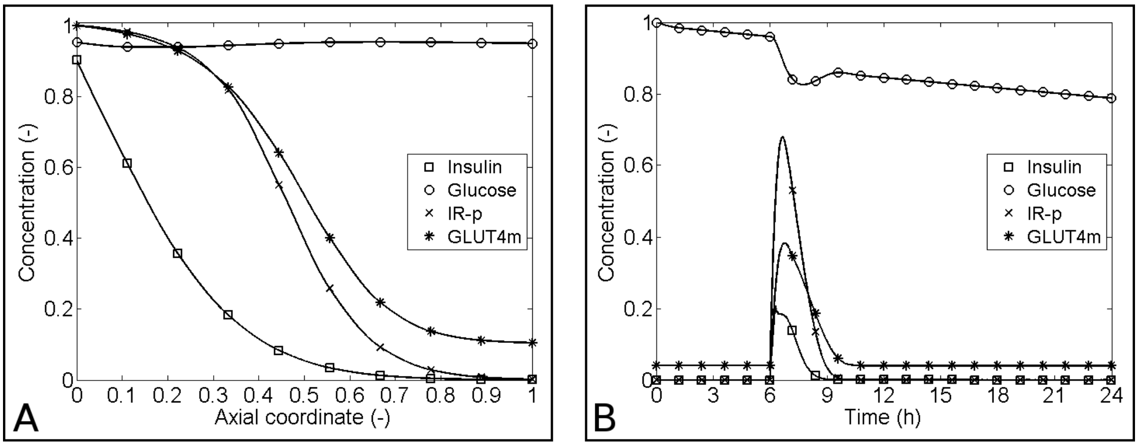

Figure 5.8: Effect of the insulin signaling pathway on cell metabolism in a single channel system. Plots show the dimensionless concentration profile insulin, glucose, once and twice bound phosphorylated insulin receptor and cell surface GLUT4. (A) Average concentration value along the axial coordinate at the end of the stimulation. (B) Temporal evolution of the average species concentration.

consequently both the insulin receptors and GLUT4m reach the maximum value at the inlet, but at the outlet their value is the basal one. Therefore the glucose concentration is lower at the inlet compare to the other sections of the channel since cells in this area are affected by the glucose uptake raising by the insulin.

Figure 5.8B shows the temporal profile of the average species value with a 100 nM insulin pulse stimulation of 15 minutes which starts after 6 h. Although the stimulus is short, its effect lasts longer in this geometry, in fact the insulin concentration returns to the zero value after about 3 h, while the other species needs even more time to restore their basal condition. Moreover the average insulin concentration reaches only the 20 % of the original stimulus due to the mass transport limitation.

5.3.3 Bioreactor outcomes

To evaluate the whole bioreactor system response subjected to an insulin stimulation is more useful to consider the macroscopic outcomes, in particular the average glucose concentration downstream the culture chamber. In this case a bioreactor with recirculation was considered in Figure 5.9; it shows the comparison between two identical simulations, one in the basal condition and one perturbed with a 100 nM insulin pulse stimulation of 15 minutes which starts after 6 h. The green line is the insulin profile at the inlet of the system, the blue lines represent the system evolution without insulin; the bold line is the average glucose value at the outlet of the system, whereas the other two lines depict the glucose dispersion due to the scaffold channel distribution. Similarly, the bold red line is the average glucose value in the stimulation case and the red region represents the glucose concentration dispersion. Without stimulation glucose concentration decreases in time because of the cell metabolism and the dispersion is almost constant with the higher concentration in the bigger channels. With insulin, the glucose level drops after the stimulus reaching a minimum value in about 2.5 h, then it raises approaching a trend parallel to the basal condition case. Also in this situation, in the bigger channels the concentration maintains a high glucose level with a small decreasing trend after the stimulus; on the other hand, in the smaller channels glucose is reduced by 80 %. For a fixed time point, Figure 5.9 depicts the glucose distribution at the outlet of each channel, its temporal evolution is represented in Figure 5.10.

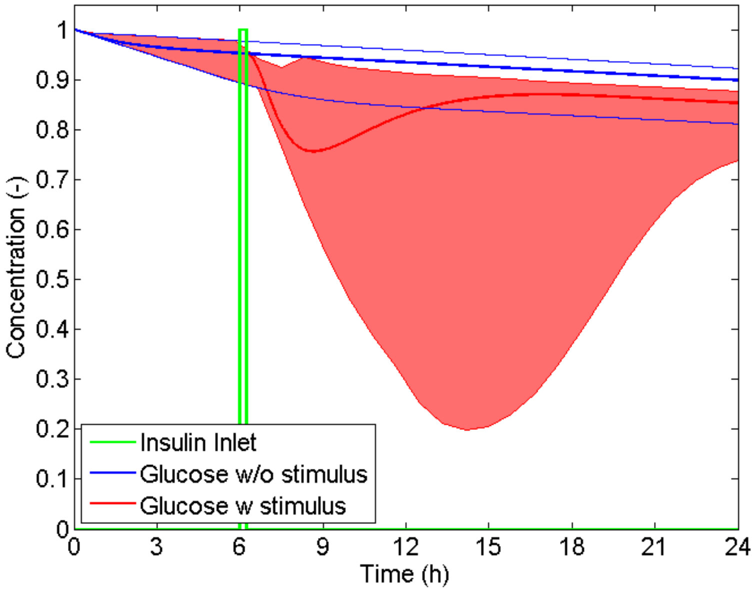

Figure 5.9: Temporal average glucose concentration profile downstream the culture chamber. The green line represents the insulin profile, the blue lines relate to the glucose concentration in a bioreactor system without stimulation and the similarly the red lines to the system with stimulation.

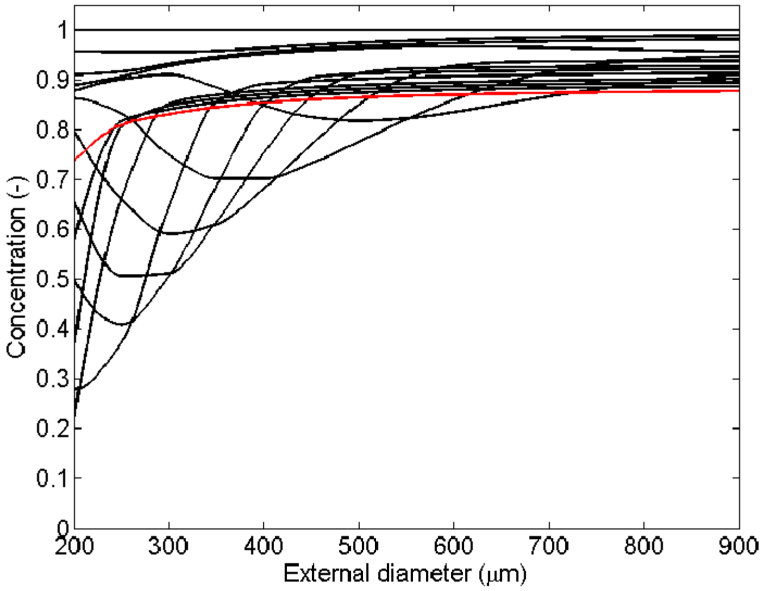

Figure 5.10: Temporal distribution of glucose concentration at the outlet of each channel. The red line depicts the glucose profile at the final time.

At the begin, all the channels are in the same condition, that is the physiological glucose level, which decreases in time due to the glucose uptake; the reduction is greater in the smaller channels. After the insulin perturbation the glucose drops faster in the channels with a diameter close to the average diameter. After that, this minimum value moves toward the smaller channels, while in the bigger glucose maintains a high value. Finally, when the effect of the insulin is over, the glucose concentration between channels is rather uniform (red line in Fig. 5.10).

5.3.4 Parameter sensitivity analysis

A parameter sensitivity analysis was performed to point out the most important variables, suggesting the accuracy to which they must be calculated; the study was performed by means of the local sensitivity method. Local sensitivity coefficients are the partial derivatives of the model state variables to the model parameters evaluated at the normal operating point where all the parameters have their nominal values. Considering a dynamic system defined by a set of N_x ordinary differential equations with N_p time-invariant parameters p:

$$\dot{x} = f\left(x, t; p\right); \quad x\left(0\right) = x_0, \tag{5.16}$$

then the absolute sensitivity is defined as:

$$S_{ij} = \left(\frac{\partial x_i}{\partial p_j}\right)_{x=x(t,\hat{p}),p=\hat{p}}. \tag{5.17}$$

These coefficients are useful for calculating errors due to parameter variations and for assessing the times at which a parameter has its greatest or least effect. The relative sensitivity of the function x_i to variations in the parameter p_j is given by:

$$\bar{S}_{ij} = \frac{p_j}{x_i} S_{ij} = \frac{p_j}{x_i}\left(\frac{\partial x_i}{\partial p_j}\right)_{x=x(t,\hat{p}),p=\hat{p}}. \tag{5.18}$$

The relative sensitivity functions are formed multiplying the absolute sensitivity function (S_{ij}) by the nominal value of the parameter and dividing by the value of the function. The computing of the local sensitivities was calculated using the finite difference approximation; it is based on changing one parameter at a time (usually 1 %) and rerunning the model. These are the parameters considered for the analysis:

- flow rate;
- insulin concentration;
- initial seeding density;
- mean channel diameter of the distribution;
- variance of the channel distribution;

and the cell membrane GLUT4 is the observed function since the glucose consumption rate is linearly proportional to this variable. The average GLUT4m was used as variable, calculated as the mean value in the channel with the average diameter. Figure 5.11 shows the influence of the parameters on the cell membrane GLUT4.

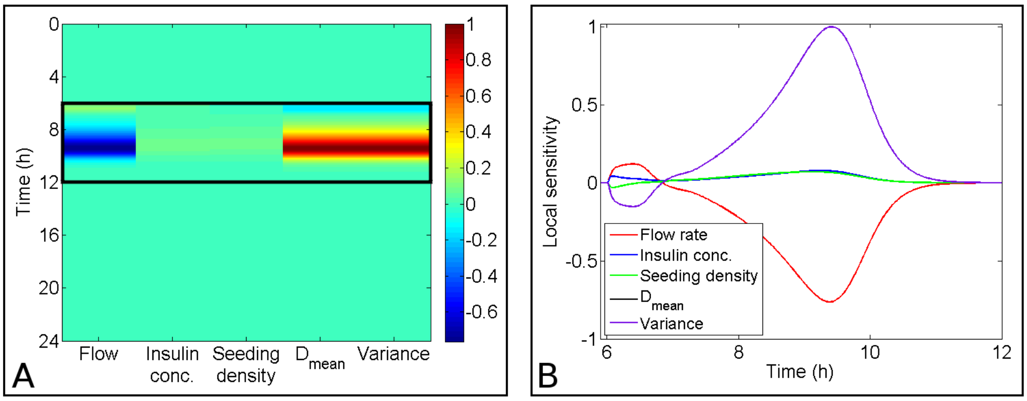

Figure 5.11: Sensitivity plot of the experimental variables: flow rate, insulin concentration, initial seeding density, average channel diameter and variance of the channel distribution. (A) Sensitivity analysis of the entire experiment duration. (B) Magnification of the sensitivity analysis for the 6 h after the insulin stimulation, framed in black in panel A.

The effect of all parameters last up to 6 hours after the beginning of the insulin perturbation, however insulin concentration and the initial seeding have a small effect than the others. On the other hand, the accuracy in the determination of the flow rate, the average diameter and the variance strongly affect the model, even if opposite effect. The average diameter and variance of the distribution have the same effect because the scaffold distribution was described with a Rayleigh distribution and the mean value and variance of this distribution are linearly dependent.

5.3.5 Operative conditions analysis

The developed model was applied to study the influence of the operative conditions and bioreactor configuration on the system response, that is the glucose consumption rate. Specifically the following variables were analyzed:

- flow rate;
- bioreactor configuration;
- stimulus type.

The flow rate was taken into account since it is easier to manipulate and in chapter 4 we have demonstrated that it highly affects the cell behavior. Considering the bioreactor configuration (open and closed) we have analyzed two limit cases; it is worth to note that the closed configuration is not easily feasible because we assumed that the cell media is continuously recirculated and at the end of the stimulus the insulin can be removed from the system without modify anything else. At last we determined if the stimulus type can influence the system behavior changing the stimulus duration and the perturbation shape.

Figure 5.12 shows the effect of the flow rate (3, 30 and 300 µL /min) on the GLUT4m expression (Fig. 5.12A-C) and on the glucose concentration and dispersion downstream the system (Fig. 5.12D-F). The simulation were run with a 100 nM insulin pulse stimulation of 15 minutes which started after 6 h from the initial time. The lower is the flow rate the higher is the effect of the glucose metabolism, i.e. the lower is the average glucose concentration at the outlet of the scaffold; in fact the system needs long time to remove all the insulin (GLUT4m level is still high after 18 hours from the stimulation). Moreover the glucose has a high dispersion

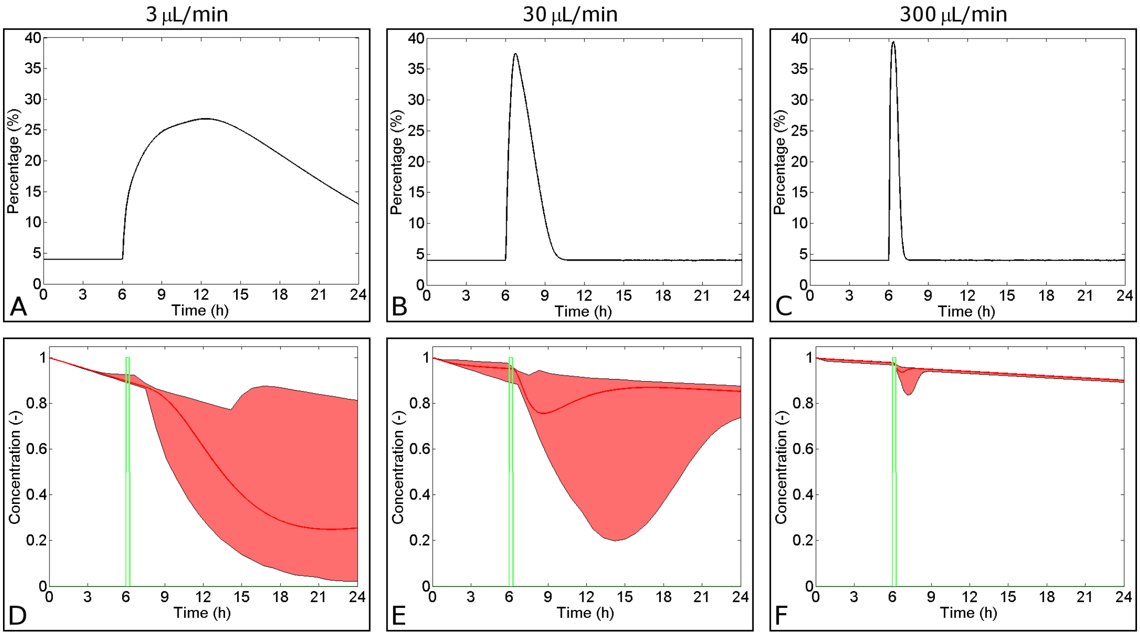

Figure 5.12: Effect of Peclet number on the temporal evolution of the cell glucose metabolism in the three-dimensional system. Total volumetric flow rate equals 3 μL /min (A, D), 30 μL /min (B, E), and 300 μL /min (C, F). (A, B, C) Temporal evolution of the GLUT4m concentration in the channel that has the mean diameter value; concentration was calculated as the average value in the whole channel. (D, E, F) Temporal evolution of the glucose metabolism after a 100 nM insulin pulse stimulation of 15 minutes. The green line represents the dimensionless input insulin concentration, the red line represents the dimensionless glucose concentration downstream the scaffold system, and the red area depicts the dimensionless glucose concentration distribution between the all channels of the scaffold.

between the smaller and the bigger channels due to the fluid dynamics; at 15 hours there is no insulin in the bigger channels, that is the glucose concentration at their outlet raise up, while in the smaller channels cells still are exposed to insulin. The increasing of the flow rate has two effects: (I) reduces the residence time, thus the effect of the insulin is shorter, and the average glucose variation is smaller; (II) the glucose dispersion at the outlet of the channels is lower. At high flow rate the effect on the average glucose level is negligible, but the dispersion is still present.

Table 5.1 summarize the influence of all evaluated variables on the average glucose concentration; two values were considered (Fig. 5.13):

- Δc, the difference between the concentration at the begin of the stimulation and its minimum value;

- $R = \Delta c / \Delta t$;

Δt is the interval of time for the determination of Δc. Figure 5.13 shows the two variables Δc and Δt in a generic glucose concentration profile plot. Maximize both Δc and R means to determine the optimal experimental conditions because the system response will be faster and detectable. Changing the amount of insulin (30 minutes pulse) or changing the stimulus shape (ramp up) does not significantly modify the cell behavior, as well as varying the bioreactor configuration. By contrast the flow rate have a double effect, indeed the lower is its value and the higher are Δc and Δt, on the other hand high flow rates reduce the response time but also its intensity.

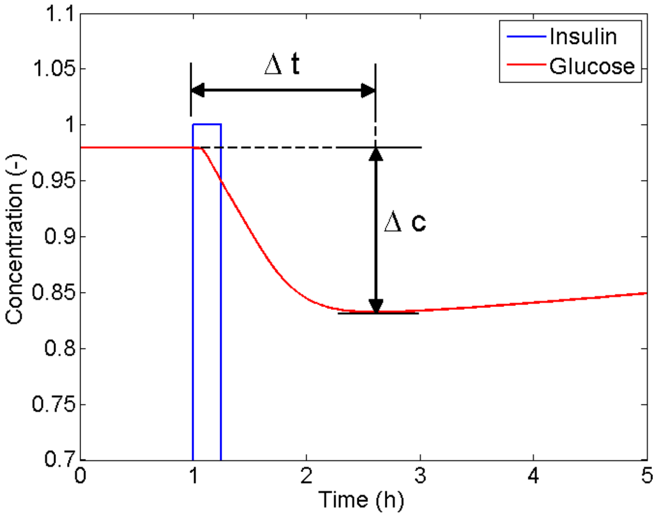

Figure 5.13: Representation of the variables Δc and Δt employed for evaluating the system response to an insulin stimulation

Table 5.1: Effect of the operative variables on the cell response to an insulin stimulation.

	Base case	Low flow	High flow	Open config.	30 min. pulse	Ramp up
Δc (mol /m^3)	0.196	0.649	0.041	0.182	0.215	0.202
R (mol /(m^3 h))	0.074	0.041	0.059	0.075	0.078	0.072

However, if the purpose would be the maximization of Δc and R a code must be written for optimizing the perturbation; a simple example is to choose the number of insulin pulses and their initial time, then the algorithm can determine their duration and intensity. For this specific system, however, the computational cost is quite high and it is not the objective of the present study.

5.4 Conclusions

In this work we studied the effect of the cell microenvironment heterogeneity in a 3D dynamic cell culture on the intracellular processes. Specifically the effect of an exogenous insulin stimulation on the cell metabolism (glucose consumption rate) was considered. To achieve this objective, our microscopic mass transport model was coupled with an insulin signaling model to describe the insulin mass transport in a 3D porous scaffold and thus study its effect on the cell signaling and on the glucose metabolism. Because of its importance for the cell physiology, insulin signaling pathways have been widely studied [15, 118, 124, 135], especially single cell model have been proposed. In this project one of the most important model [15] was analyzed and with the model reduction it was slightly simplified for computational costs reasons.

The new developed model is able to describe the spatiotemporal evolution of metabolites in a 3D geometry and to determine the local cell response to an exogenous insulin stimulation. First of all, it catches the difference of a 3D system, for example a single channel, compare to the single cell case (Fig. 5.6 and 5.7), pointing out the mass transport effect on the whole system behavior.

In addition the influence of different experimental conditions was evaluated, in particular the flow rate, the bioreactor configuration and the stimulus type were considered; above all, the medium flow rate is the variable which most affects the cell response (Tab. 5.1).

This model could play an important role for studying metabolic disorder such type 2 diabetes, indeed it can reproduce the physiological response of a cell system to an insulin stimulation and therefore modifying the signaling model it could describe the cell response for a type 2 diabetes case. Such model could be a helpful tool in the bioreactor design for diagnosis of the disease and for drug screening.

6

Cell signaling modeling of a three-dimensional tissue culture in microfluidic platform

In the last chapter of the thesis, the mathematical and numerical framework developed in chapter 3, 4, and 5 were used for creating a model of cell signaling for a tissue culture in a microfluidic platform. The final aim of this study is the development of tools for supporting the design and the realization of microfluidic platform to be used as drug signaling pathways screening assay.

6.1 Motivations

In human body, blood glucose level is regulated by hormonal control to brings back the glucose concentration to the normal range whenever a perturbation occurs; this regulatory mechanism is the glucose homeostasis. There are mainly two molecules involved in the controlling of glucose level: insulin and glucagon. Insulin is a peptide hormone produced in the pancreas within the β-cells of the islets of Langerhans, glucagon is a hormone secreted by the α-cells of the islets of Langerhans. Insulin and glucagon are part of a feedback system that keeps blood glucose levels at the right level (Fig. 6.1). When glucose concentration increases, for example after a meal, insulin is secreted from the pancreatic β-cells into the body to decrease the endogenous hepatic glucose production and to promote the glucose uptake into insulin-sensitive tissues, such as skeletal muscle and adipose tissue. By contrast, when the glucose level is low, the pancreatic α-cells release glucagon into the circulation, in the liver it promotes the conversion of stored glycogen into glucose, which is released into the bloodstream.

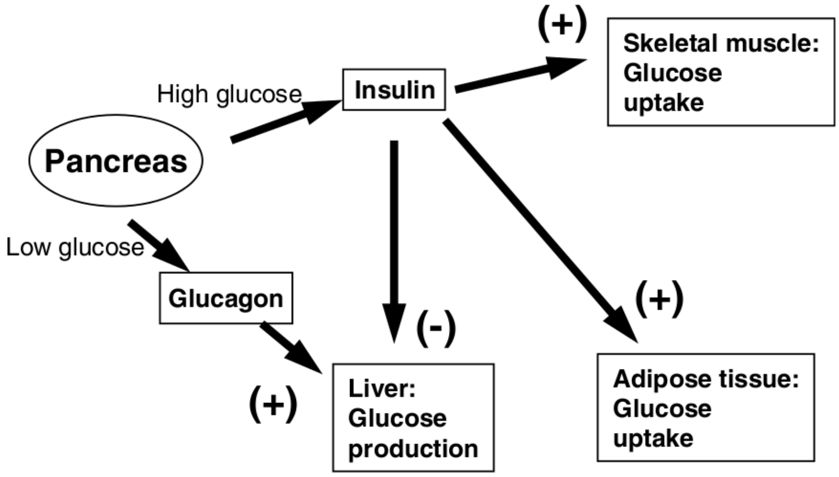

Figure 6.1: Representation of glucose homeostasis. High glucose concentration triggers the secretion of insulin from the pancreas which increases the glucose uptake and reduces the glucose production from the liver. Low glucose level leads to glucagon release to enhance the glucose production. Figure reprinted from Karlsson and Zierath [136].

However, in diabetic individual, this regulatory system fails to control the blood sugar resulting in a hyperglycemia condition. Lack of or severe reduction in insulin secretion due to autoimmune destruction of β-cells is responsible for type 1 diabetes mellitus. The more prevalent form, type 2 diabetes mellitus (T2DM) accounts about 90 % of all diabetes in developed countries.

Type 2 diabetes is a complex metabolic disorder that involves progressive development of insulin resistance and deficient insulin secretion by pancreatic β-cells, leading to hyperglycemia [137–140]. Early in the natural history of type 2 diabetes, insulin resistance is well established [141–143], that is cells fail in the insulin signaling transduction pathways starting from the binding of insulin to insulin receptor to the translocation of GLUT4. Glucose transporter type 4 (GLUT4) is a protein found in adipose tissues and striated muscle that regulates the glucose transport into the cells. At basal conditions, GLUT4 is mainly in the cytoplasm within vesicles, in contrast, insulin increases the fraction of GLUT4 at the cell membrane.

Glucose tolerance remains normal because of a compensatory increase in insulin secretion [128, 144–146]. As adaptive response to this condition, plasma insulin concentration progressively rises (hyperinsulinemia), but when the blood glucose level exceeds a threshold value (about 140 mg /dL), β-cells are unable to maintain the elevated production rate of insulin secretion and the its concentration declines.

The causes of type 2 diabetes are still not well known, however studies have associated this disease with genetic [147, 148] and environmental factors [149]. Because of the economical and sociological impact of the this disease, early diagnosis and adequate treatment are important to decrease the long-term adverse effects of diabetes. There are several oral antidiabetic drugs, as well as insulin, and the common practice is the trial and error approach to determine the right medication for each patient. Therefore it would be extremely relevant the development of a fast drug screening protocol able to determine the more suitable drug for a specific individual.

To this end we have designed and developed a microfluidic platform for culturing adipose tissue from human biopsy in order to characterize cells in term of glucose uptake for obtaining specific metabolic information. This microfluidic device is a complex system characterized by multiscale phenomena and its design and operative conditions can strongly affect the final results, hence the information that we could acquire from a tissue culture.

A mathematical model was developed to rationalize such system and assisting the design of the microfluidic platform for an *ex vivo* human adipose tissue culture for the optimization of the system readouts. In addition it was applied to reproduce *in vitro* the pathophysiological response of type 2 diabetes to an insulin stimulation in adipose tissue culture through the inhibition of insulin receptor effector, according to a chronic inflammatory response.

6.2 Theoretical framework

The PDMS microfluidic platform (Fig. 6.2A) designed for the tissue culture and characterization is composed of a culture chamber where the adipose tissue is allocated. Medium flows through the well and an online biosensor monitors the tissue response, that is the glucose concentration.

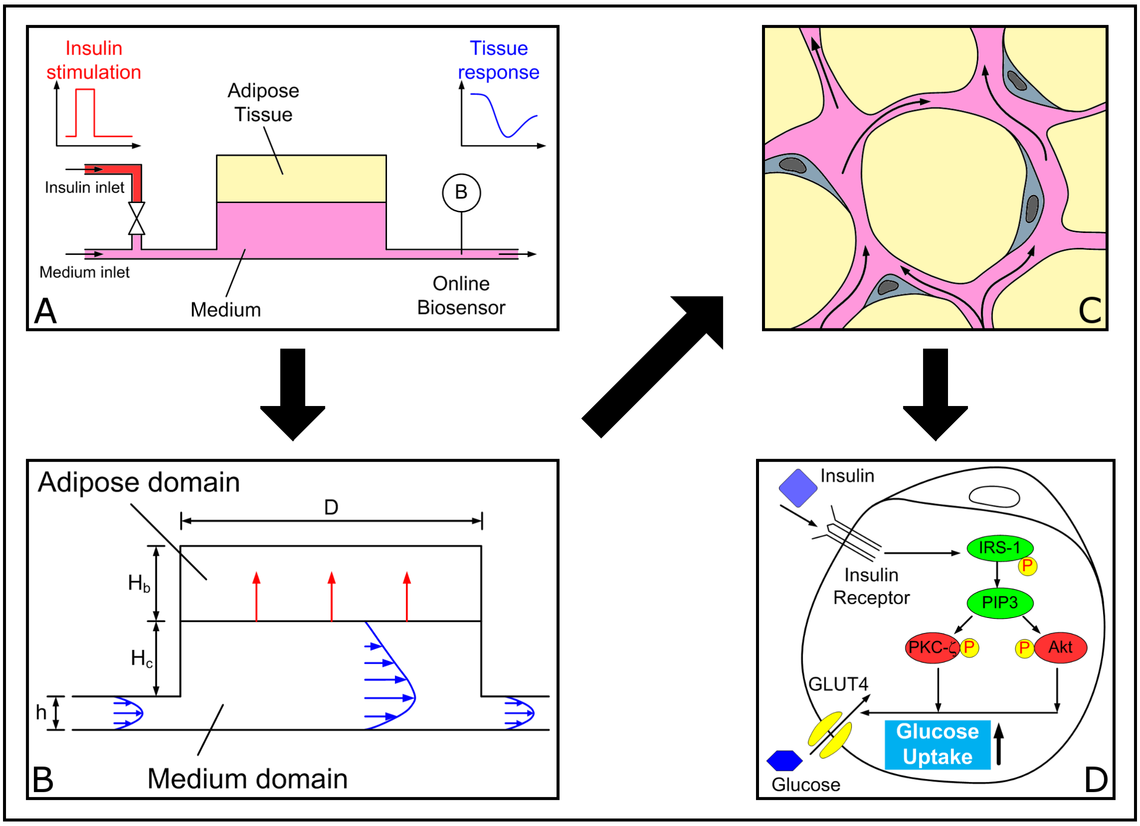

Figure 6.2: Representative scheme of the microfluidic multiscale system. (A) Microfluidic platform, (B) culture chamber, (C) cell cluster, (D) single cell system.

The chamber (Fig. 6.2B) is a cylindrical well with diameter (D) equals to 4 mm, a bottom inlet/outlet configuration was used. A microfuidic channel at the bottom of the well delivers fresh cell media, while the waste medium exits by means of the outlet channel on the other side of the chamber. The whole channel has a rectangular cross section, it is 100 µm height and 40 µm width and 3.5 cm long. The human adipose tissue biopsy is allocated at the top of the culture chamber since its density is lower than the medium density, so it floats. Experimentally we are able to obtain biopsy of 1 mg, and we assumed that it occupies a cylindrical volume with the same diameter of the well and its height ranges from 1 to 2 mm.

In this system there are two regions, the medium domain (I) and the tissue domain (II). Fresh cell media in equilibrium with the incubator atmosphere is continuously pumped in the system using a syringe pump, here the mass transport of the molecules is governed by both convection and diffusion. In the culture chamber there is a gradient from the bulk to the medium/biopsy interface (red arrows in Fig. 6.2B), therefore glucose enters in the tissue where the mass transport is governed only by the intracellular diffusion (black arrows in Fig. 6.2C). Finally glucose is consumed by cell metabolism. The model describes also the perturbation of the system by means of an insulin stimulation; it diffuses in the tissue where it is internalized by cells and triggers the insulin signaling pathways (Fig. 6.2D) that increases the glucose consumption rate. Since the objective of these experiments is the characterization of the adipose tissue in term of glucose consumption, a period of adaptive behavior of a *ex vivo* tissue culture has not been considered. New steady state is assumed to be reached after 24 h.

6.3 Mathematical model

The microfluidic platform was modeled considering the medium fluid dynamic, the glucose and insulin mass transport and the insulin signaling pathways. To reduce the computational costs the 2D geometry was studied.

6.3.1 Microfluidic platform model

The Navier-Stokes equation for incompressible flow was used to describe the fluid dynamic in the medium domain (no convection in the tissue domain):

$$\rho \frac{D\boldsymbol{v}}{Dt} = -\nabla p + \mu \nabla^2 \boldsymbol{v} + \rho \boldsymbol{g}, \tag{6.1}$$

where ρ is the medium density, $\boldsymbol{v}$ is the velocity field, μ is the medium viscosity, p is the pressure, and g is the gravity. The species mass balance for glucose and insulin, for both domains, are given by Eq. (6.2):

$$\frac{\partial c}{\partial t} = -\nabla N + R, \tag{6.2}$$

with c is the concentration, N is the flux and R is the cell substrates uptake. The term R equals zero in domain I because no reactions occur in this region, whereas the fluxes are expressed in the two domains by:

$$N^{I} = -D^{I}\nabla c^{I} + \boldsymbol{v}c^{I}, \tag{6.3}$$

$$N^{II} = -D^{II}\nabla c^{II}, \tag{6.4}$$

where D is the species diffusion coefficient at 37 °C. The glucose consumption rate was described using Michaelis-Menten kinetic model from literature [132], as reported in chapter 5, and it follows:

$$R_G = -\left(\frac{GLUT4m}{GLUT4m|_{basal}}\right)\left(\frac{1}{\tilde{v}_{cell}}\frac{V_{m,G}c_G^{II}}{K_{m,G}+c_G^{II}}\right). \tag{6.5}$$

In Eq. (6.5) $\tilde{v}_{cell}$ is the cell specific volume, $V_{m,G}$ is the maximal glucose consumption rate and $K_{m,G}$ is the glucose concentration at half-maximal glucose consumption, $GLUT4m$ is the percentage of protein on cell membrane, and $GLUT4m|_{basal}$ is the percentage of protein on cell membrane at basal condition, i.e. in absence of insulin stimulation. Both $GLUT4m$ concentrations are outputs of the insulin signaling model, and glucose consumption rate is proportional to their ratio due to the raise of cell membrane GLUT4 expressed by cells after an insulin perturbation. As assumed in chapter 5, a linear dependence of glucose metabolism from cell surface GLUT4 was considered. On the other hand, the insulin depletion due to the insulin binding with its receptor at the cell membrane and its internalization is negligible compare to the total amount inside the system.

The model, composed of the Navier-Stokes equation, a mass balance equation for each domain and the insulin signaling model (see Appendix C for signaling model details), were solved with the following inlet boundary conditions:

$$\boldsymbol{v}(x,y,t) = \boldsymbol{v}_{inlet} \qquad x=0, \tag{6.6}$$

$$c_G(x,y,t) = c_{G,0} \qquad x=0, \tag{6.7}$$

$$c_{Ins}(x,y,t) : \begin{cases} c_{Ins,0}, & \text{if } t_{in}^{stim} \leq t \leq t_{fin}^{stim}, \\ 0, & \text{otherwise.} \end{cases} \qquad x=0. \tag{6.8}$$

Where the $\boldsymbol{v}_{inlet}$ is the medium velocity in inlet microfluidic channel, $c_{G,0}$ is the glucose concentration in fresh medium, $c_{Ins,0}$ is the concentration of the insulin solution used to stimulate the system, t_{in}^{stim} and t_{fin}^{stim} are the initial and final time of the stimulation, respectively. At the outlet a pressure condition was applied ($p = 0$) for Eq. (6.1), while a convective flux condition was used for both species. All other boundaries were set as a wall for Eq. (6.1) and an insulation condition was used for the mass balance equations. The initial conditions for the Navier-Stokes equation and for the mass balance equations follow:

$$\boldsymbol{v}\left(x,y,t\right) = 0 \qquad t = t_{in}, \tag{6.9}$$

$$c_G\left(x,y,t\right) = c_{G,0} \qquad t = t_{in}, \tag{6.10}$$

$$c_{Ins}\left(x,y,t\right) = 0 \qquad t = t_{in}. \tag{6.11}$$

All the initial conditions for species concentration involved in the signaling model are reported in Appendix C.

6.3.2 Signaling model

The reduced model derived in chapter 5 from the Sedaghat model [15] was applied to describe insulin signaling pathway. Using the outputs of the mass balance equations, the model locally describes the temporal evolution of all state variables in domain II and most importantly provides the GLUT4m expression for the determination of the local glucose consumption rate. All the equations with their kinetic parameters all listed in Appendix C.

6.4 Numerical model

The tissue culture in the microfluidic platform model was numerically solved using the finite element method (FEM) and it was implemented in COMSOL Multiphysics 3.5 (COMSOL Inc., Burlington, MA). Two test were conducted on this approach:

- the solution and the computational validation of the original insulin signaling model [15];

- the mass conservation was tested for all species;

The signaling model was implemented in COMSOL for a 1D geometry for simulating a single cell system and obtain all the state variables temporal profiles. The outcomes were compared with the published data [15], specifically we compared the once and twice bound phosphorylated insulin receptor and cell surface GLUT4 since they are, respectively, the firsts and the last variables in the signal cascade. These results are in agreement with the original outcomes, and the average percentage error in the GLUT4m determination equals 1.7 %. For testing the mass conservation, the whole model was run for a long simulation time to allow the insulin to leave the system, and the amount of insulin at the inlet and at the outlet was determine as:

$$n_{Ins} = \int_t \int_L c_{Ins} \, dx dt, \tag{6.12}$$

Comparing these two values we achieved a percentage error equals to 0.01 %.

6.5 Results

The developed mathematical model was applied to support in the process of design and realization of the microfluidic platform for tissue culture; finally a type 2 diabetes case study will be presented.

6.5.1 Microfluidic platform outcomes

Figure 6.3 shows an example of the outcomes of the mathematical model for a three-dimensional tissue culture in the microfluidic platform. Both macroscopic variables and microscopic distribution of species are represented. The three main species in the glucose uptake under insulin stimulation were considered, that is insulin, cell membrane GLUT4 and glucose. The average concentration downstream the chamber was evaluated for insulin and glucose; in contrast the local distribution of insulin, cell membrane GLUT4 and glucose were detect in the tissue domain. These distributions were studied along the length (section A–A in Fig. 6.3a) and the height of the domain (section B–B in Fig. 6.3a).

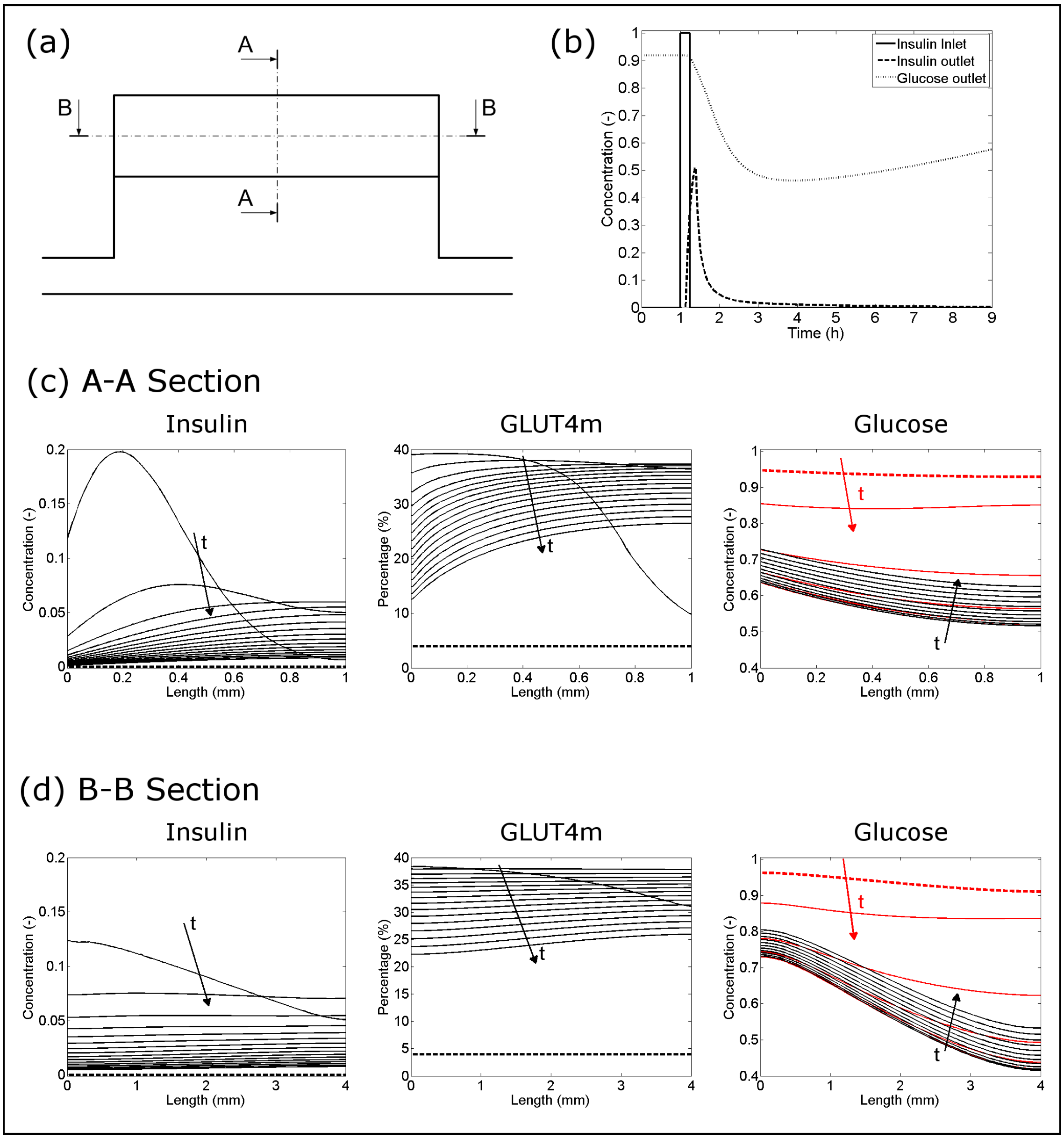

Figure 6.3: Outcomes of a 3D tissue culture in the microfluidic platform model. (a) Representation of the tissue culture chamber. (b) Temporal evolution of the insulin concentration at the inlet (solid line) and at the outlet (dashed line) of the chamber, and glucose concentration at the outlet (dotted line). (c) Temporal evolution of insulin, cell membrane GLUT4, and glucose distribution along section A-A of the biopsy. (d) Temporal evolution of insulin, cell membrane GLUT4, and glucose distribution along section B-B of the biopsy. In both (c) and (d) figures, the bold dashed line represent the initial condition, each line represents a 30 minutes time step; for glucose plots, red lines show the temporal evolution during the first hours until reaching the maximum effect of the insulin stimulation (lower glucose concentration), then black lines represent the evolution in time of the system during the recovery of the system.

The system at the steady state (without insulin) was stimulated with a 100 nM insulin perturbation of 15 minutes after 1 hour from the beginning (Fig. 6.3b). After the stimulation, insulin exits the system with a delay, its signal is wider and has a lower intensity than the inlet condition due to the fluid dynamics in the platform. After the perturbation, glucose level decreases in time because of the activation of the insulin signaling pathway, the signal cascade reaches the maximum effect after about 3 hours, then the glucose level slowly goes up.

Figure 6.3c shows the species distribution along the height of the tissue. In these experimental conditions, the maximum insulin concentration the cells are exposed to is only the 20 % of the inlet value. Moreover only 400 µm in depth of the adipose tissue is subjected to this value, in the other regions the insulin is about the 5 %. Although the stimulation within the tissue is heterogeneous, the GLUT4m almost reaches the maximum value all over the domain, moreover the inner region is affected for longer time. Because of its higher residence time, the insulin has a stronger effect in the regions far from the medium, here, the glucose concentration decrement is greater than the cells closer to the medium.

Figure 6.3d depicts the species distribution along the length of the tissue. The species profiles are quite uniform, but due to the residence time, there is a delay on the tissue region close to the outlet, therefore the GLUT4m increases slowly and its effect lasts longer. The glucose concentration is lower in this region due to a high demand glucose uptake.

6.5.2 Microfluidic platform optimization

The mathematical model was developed mainly for helping in the design of the microfluidic chip, that is defining the experimental parameters to have a detectable and fast tissue response to an insulin stimulation. To achieve this goal we used the same approach presented in chapter 5; variables Δc and R were maximized changing the following parameters:

- culture chamber geometry;
- flow rate;
- stimulus type and duration.

For the culture chamber, the height of the biopsy (H_b) and the height of the chamber interlayer (H_c)(Fig. 6.2B) were determined; once the chamber geometry was fixed the flow rate ($\dot{Q}$) and the stimulus were optimized. Unlike the original initial conditions (Eq. (6.9) and (6.10)), all the simulations were run using the steady state at basal level (without insulin) as initial condition; the system was perturbed with a 100 nM insulin pulse stimulation of 15 minutes (except for the stimulus duration analysis) which started after 1 h from the initial time. Simulations were stopped after 9 h because we were interested in a fast system response and in the positive variation of glucose uptake rate.

Figure 6.4A shows the effect of the culture chamber configuration on the average glucose concentration downstream the system. The red line depicts the insulin stimulation, while all the others lines are the glucose concentration. In detail solid lines represent simulations with a biopsy height of 1 mm, while the dashed lines is the case with a thickness equals to 2 mm. Each group has three distinct lines, they represent the culture chamber height (H_c):

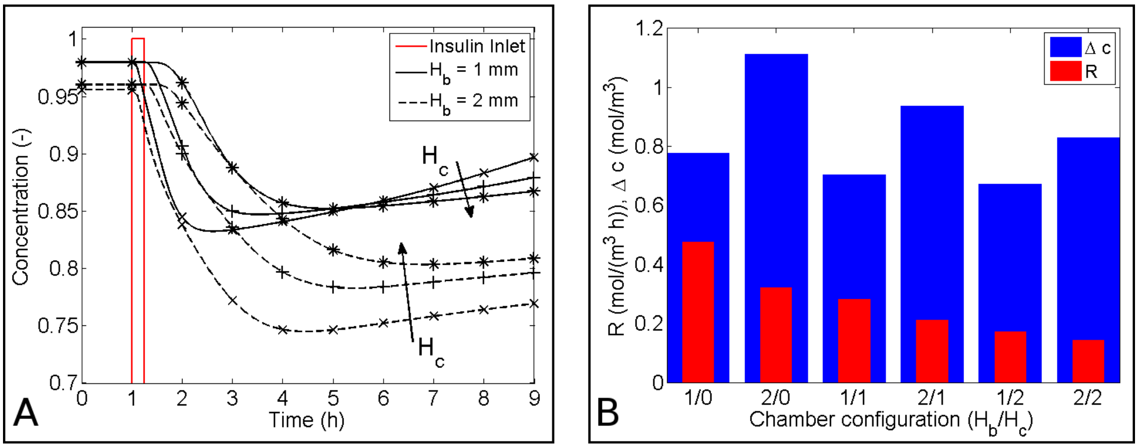

Figure 6.4: Effect of the microfluidic platform configuration on the glucose uptake. (A) Average glucose concentration profile downstream the culture chamber after a 100 nM insulin pulse stimulation of 15 minutes at the inlet of the chamber (red line). Solid line and dashed lines denote a biopsy height of 1 and 2 mm, respectively. Each biopsy condition was studied changing the culture chamber height, 0 mm (×), 1 mm (+) and 2 mm (∗). (B) Quantification of the influence of the microfluidic platform configuration, in term of the variables Δc (blue bars) and R (red bars).

- 0 mm (×);

- 1 mm (+);
- 2 mm ($*$);

The configuration with a small biopsy (solid lines in Fig. 6.4A) has a faster response, i.e. it reaches the minimum of concentration in a shorter time, because the mass transport in the tissue is governed only by interstitial diffusion. However in the case with $H_b = 2\,\mathrm{mm}$ the minimum glucose concentration is lower because of the grater reaction volume. The chamber height has a negative effect on the tissue response, indeed the higher is the chamber, the slower and the smaller is the outcome because the holdup volume acts as a buffer for the system. The intensity of the variables (Δc) and R were analyzed to determine the optimal configuration (Fig. 6.4B). Chambers with the thicker biopsy has a higher concentration drop, however configuration A is preferred; it has a Δc about 20 % smaller than the 2 mm biopsy cases, but the highest value of R. Once the culture chamber geometry is optimized, different operative conditions were investigated. Figure 6.5A shows the effect of the medium flow rate on the tissue response (black lines) subjected to the insulin perturbation (red line); flow rate value ranges from 0.5 to 0.005 µL /min. The lower is the cell media flow, the lower is the downstream glucose concentration, it almost approaches

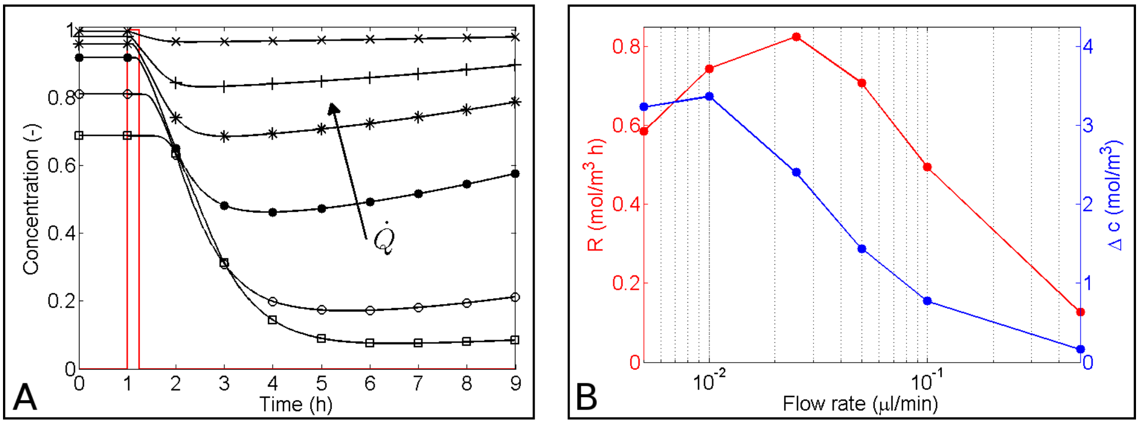

Figure 6.5: Effect of the medium flow rate on the glucose uptake. (A) Average glucose concentration profile downstream the culture chamber after a 100 nM insulin pulse stimulation of 15 minutes at the inlet of the chamber (red line) at different flow rate: 0.5 µL /min (×), 0.1 µL /min (+), 0.05 µL /min ($*$), 0.025 µL /min (•), 0.01 µL /min (○), 0.005 µL /min (□). (B) Quantification of the influence of the medium flow rate, in term of the variable R (red line) and Δc (blue line).

to zero for the minimum flow value. On the other hand, at the highest flow rate the variation is only about 3 %.

The R and the Δc profiles as function of the flow rate are represented in Figure 6.5B; the R value approaches to a maximum with a flow rate of 0.025 µL /min, this condition is characterized by a concentration drop of about 55 %.

At last the stimulus was analyzed, i.e. changing the pulse duration from 1 min to 1 h, up to a step perturbation (Fig. 6.6). The longer is the stimulation the lower is the downstream average glucose concentration while the system response time raises. Since the Δc values are quite similar for stimulation longer that 10 minutes we picked the 30 minutes pulse which has the highest value of R, although it is worth to observe that from 10 to 30 minutes the experimental results could be the same.

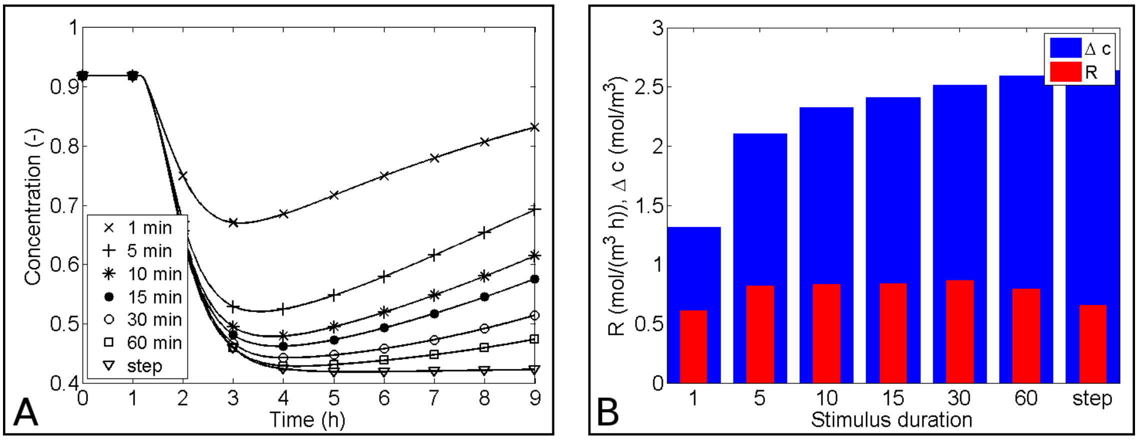

Figure 6.6: Effect of the stimulus duration on the glucose uptake. (A) Average glucose concentration profile downstream the culture chamber after a 100 nM insulin stimulation at the inlet of the chamber with different duration, 1 min ($\times$), 5 min ($+$), 10 min ($*$), 15 min ($\bullet$), 30 min ($\circ$), 60 min ($\Box$), step ($\bigtriangledown$). (B) Quantification of the influence of the stimulus duration, in term of the variable Δc (blue bars) and R (red bars).

6.5.3 Simulation of insulin resistance case study

Recent studies have demonstrated that adipose tissue is not only a passive reservoir for energy storage, but also an endocrine organ [150, 151]. Indeed, adipose cell is actively involved in sensing the nutritional and metabolic status of the organism through several different signaling pathways and regulates energy metabolism by secreting molecules in response to these cues [152]. These hormones (adipokines) act at both the local (autocrine/paracrine) and systemic (endocrine) level. Tumor necrosis factor α (TNF-α) is one of these cytokines secreted by adipocytes and it potentially has a physiological or pathophysiological roles in the regulation of adipocyte differentiation, lipid metabolism and *in vivo* insulin sensitivity. Eighty percent of type 2 diabetes mellitus patients are obese and obesity is associated with insulin resistance [153]. Obese subjects have a higher TNF-α level [154] and it has been demonstrated to regulate or interfere with adipocyte metabolism at different sites such as the insulin receptor, so it has been linked with the development of insulin resistant [154–158].

In cultured adipocytes TNF-α increases the phosphorylation of insulin receptor substrate-1 (IRS-1) at serine residues, hence this adipokine acts as an inhibitor of the insulin receptor (IR) tyrosine kinase [159, 160]. Such a modification of IRS-1 has been observed in obesity [161] and is sufficient to block the downstream events of IR signaling, including the association of IRS-1 with phosphotidylinositol (PI) 3-kinase [159, 161, 162].

The effect of the TNF-α on the insulin signaling pathways (Fig. 6.7) presented in chapter 5, was described as an inhibition reaction which reduces the tyrosine-phosphorylated IRS-1, therefore the amount of activated PI 3-kinase [163]. Using the microfluidic culture chamber with the operative conditions previously defined we compared the biological response of two different cases: a human biopsy from healthy patient and one from an insulin resistance subject. In Figure 6.8 the black line depicts a 100 nM insulin pulse stimulation of 30 minutes which, while the other solid lines represent the glucose concentration downstream the culture chamber; the blue solid line shows the healthy case profile, by contrast the red solid line is the insulin resistant patient. The dashed lines depicts the experimental error (5 %) for the glucose measurement using for example a standard glucose meter for testing the blood glucose level. The glucose concentration decreases in time due to the stimulation, and the reduction is greater in the healthy patient case. Nevertheless it must be noted that the difference between the two cases is experimentally measurable, it is about 50 %.

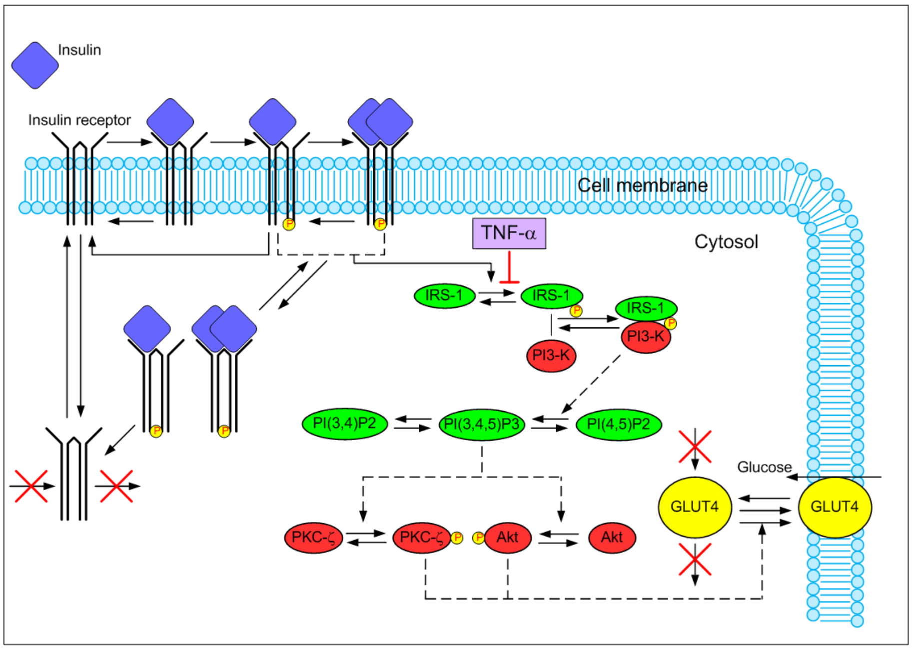

Figure 6.7: Reduced insulin signaling pathways model with the TNF-α inhibition effect on the IRS-1 tyrosine phosphorylation.

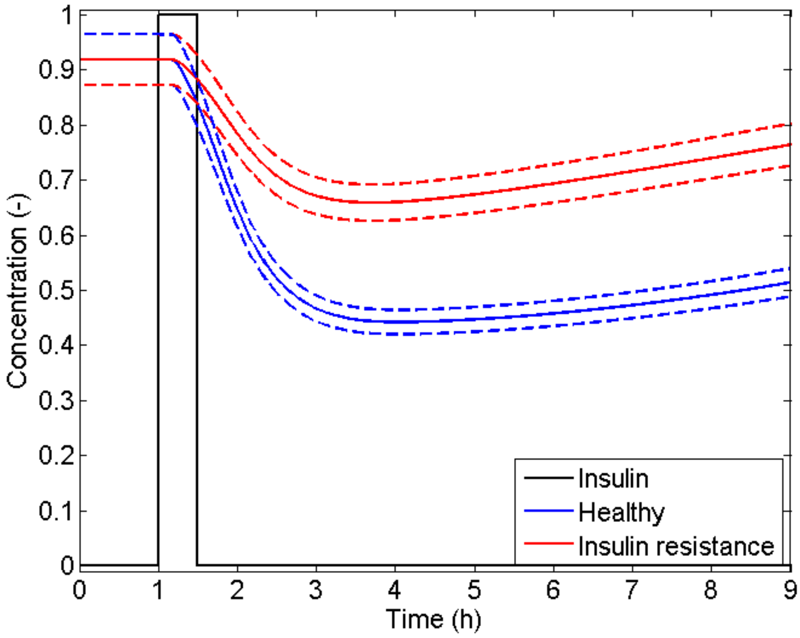

Figure 6.8: Temporal glucose concentration profile downstream the culture chamber with a 100 nM insulin pulse stimulation of 30 minutes. The black line represents the insulin profile, the blue lines relate to the glucose level for a healthy patient, while the red lines for an insulin resistance case. Dashed lines represents an experimental error of 5 %.

6.6 Conclusions

The project developed in this chapter has integrated together all the work presented in the thesis:

- the analysis of multiscale systems;
- the mathematical modeling of biological system;
- the numerical approaches and techniques;
- the biological sensitivity derived from the laboratory experiences and applications.

In particular, a mathematical model was developed to describe an *ex vivo* human adipose tissue culture in a microfluidic platform. The model considers the metabolic response, in term of glucose concentration, of the tissue to an insulin stimulation.

Such model was applied for the optimization of the macroscopic system outcomes because these are the experimental variables that could be easily measured. Specifically, we determine the geometrical properties of the culture chamber (Fig. 6.4) and the operative conditions (Fig. 6.5 and 6.6) to maximize the adipocytes glucose consumption rate.

In addition, the model is able to reproduce the pathophysiological response of *ex vivo* human adipose tissue from diabetic patient to an insulin stimulation. Comparing this result with a normal case study (healthy individual), the model predicts an experimentally measurable difference between the two outcomes (Fig. 6.8). It means that the effect of pharmacological treatments of diabetes (drug screening) could be detected and it would be possible to evaluate their efficiency.

7

Conclusions

This work focused on the development of a multiscale and multidisciplinary approach for understanding biological and physical phenomena in three-dimensional dynamic cell and tissue culture.

We used mathematical modeling to rationalize *in vitro* 3D model experiments of the pathophysiological condition of type 2 diabetes mellitus. The theoretical study of cell and tissue culture in a dynamic perfusion bioreactor has been supported by experimental data.

The scaffold morphology has been characterized by means of image analysis. A new protocol for the measurement of glucose levels in the cell medium has been developed in order to determine the glucose consumption rates of C2C12 cell line. As mentioned above, three-dimensional cell cultures in a perfusion bioreactor have been carried out for the validation of the mathematical model.

Theoretical studies were performed on different dynamic cell culture systems. We at first analyzed the influence of operative variables, such as medium flow rate and culture chamber configuration, on a cell culture in a microfluidic platform. This study showed that operative parameters could negatively affect the cell microenvironment. In addition, it has been proved that a discontinuous management of such devices could be an alternative to the traditional microfluidic cell culture setup to better preserve the cell niche.

Uniform cell culture is required for obtaining useful *in vitro* models or grafts for transplantation. In a perfusion bioreactor, the extrinsic heterogeneity due to the pore size distribution and the operative conditions can affect the culture homogeneity.

To this end, we developed a mathematical model to link the experimental parameters to the local properties of the cell microenvironment and to the cell growth. The model is able to describe the relations between macroscopic and microscopic variables and it gives the temporal evolution of the local properties distribution.

The cells response to endogenous and exogenous factors, such as insulin, has an important role for understanding the physiopathology of type 2 diabetes. For this reason, we have studied the influence of insulin on the glucose consumption rate; the insulin signaling model was integrated with a mass transport model in order to describe the dynamic response of a cell or tissue culture to an insulin stimulation. This study showed that the culture conditions (operative variables and heterogeneities) highly affect the cell response to an insulin perturbation, moreover such conditions can be controlled to have a detectable signal.

The relevant biological results have been obtained coupling all these skills. The development of a microfluidic platform for an *ex vivo* human adipose tissue culture from both healthy and diabetic patients has been supported by a mathematical model. The model helped during the design of the microfluidic chip to determine the geometrical parameters and also the experimental conditions to have a measurable tissue response when subjected to insulin stimulation.

This application can be used for the characterization of human tissue and moreover for testing the effect of pharmacological treatments of diabetes (drug screening) and to evaluate their efficiency.

Appendix A

A Combining Method to Enhance the *In Vitro* Differentiation of Hepatic Precursor Cells

Amedeo Carraro, M.D.,[1,*] **Marina Flaibani, Ph.D.,**[2,*] **Umberto Cillo, M.D.,**[1] **Lisa Michelotto, Sc.D.,**[3] **Enrico Magrofuoco, M.Sc.,**[2] **Maurizio Buggio, Sc.D.,**[1] **Giovanni Abatangelo, M.D.,**[3] **Roberta Cortivo, Sc.D.,**[3] **Maria Beatriz Herrera, Sc.D.,**[4] **Ciro Tetta, M.D.,**[5] **Nicola Elvassore, Ph.D.,**[2] **and Barbara Zavan, Ph.D.**[3]

[1]Hepatobiliary and Liver Transplant Unit, Department of General Surgery and Organ Transplantation, [2]Department of Chemical Engineering, Principles and Practice, and [3]Department of Histology, Microbiology, and Biomedical Technology, University of Padova, Padova, Italy.

[4]Molecular Biotechnology Center, University of Torino, Torino, Italy.

[5]Fresenius Medical Care Deutschland GmbH, Bad Homburg, Germany.

[*]These two authors contributed equally to this work.

TISSUE ENGINEERING: Part C
Volume 16, Number 6, 2010

DOI: 10.1089/ten.tec.2009.0795

A.1 Abstract

The ideal bioartificial liver should be designed to reproduce as nearly as possible *in vitro* the habitat that hepatic cells find *in vivo*. In the present work, we investigated the *in vitro* perfusion condition with a view to improving the hepatic differentiation of pluripotent human liver stem cells (HLSCs) from adult liver. Tissue engineering strategies based on the cocultivation of HLSCs with hepatic stellate cells (ITO) and with several combinations of medium were applied to improve viability and differentiation. A mathematical model estimated the best flow rate for perfused cultures lasting up to 7 days. Morphological and functional assays were performed. Morphological analyses confirmed that a flow of perfusion medium (assured by the bioreactor system) enabled the *in vitro* organization of the cells into liver clusters even in the deeper levels of the sponge. Our results showed that, when cocultured with ITO using stem cell medium, HLSCs synthesized a large amount of albumin and the MTT test confirmed an improvement in cell proliferation. In conclusion, this study shows that our *in vitro* cell conditions promote the formation of clusters of HLSCs and enhance the functional differentiation into a mature hepatic population.

A.2 Introduction

Liver transplantation still represents the only effective treatment for patients with liver failure, but the increasing demand for organs is unfortunately so great that many patients die while awaiting transplantation.[1] Many researchers have attempted to develop various extracorporeal bioartificial liver systems to provide temporary support for exhausted liver. The bioartificial liver is a cell-based life-support device intended to enhance hepatic detoxification and protein synthesis functions. In theory, it should compensate for the functions of a whole liver.[2–5] For the time being, however, such supports can only temporarily replace a subset of essential liver functions; the most important challenge concerns how to maintain viable and functional hepatocytes outside the native liver environment.[6] The use of bioreactors is a fundamental requirement because of the high metabolic activity of liver cells. Several hepatocyte bioreactors, based on different configurations, have been developed and most attempts were focused on adapting bioreactor technologies to the development of an extracorporeal hybrid liver support device.[2,7] Despite recent advances, isolated hepatocytes usually begin to proliferate under suboptimal culture conditions, but they have the tendency to lose most of the characteristic differentiated hepatic functions progressively, dying within 3–4 days.[8,9] In an effort to overcome this limitation, which relates to the marked specialization of mature hepatocytes, several authors turned their attention to stem cell biology. Herrera *et al.* were recently successful in isolating a population of adult human liver stem cells (HLSCs).[10] These HLSCs differentiated into mature hepatocytes and *in vivo* they contributed to regenerating the liver parenchyma in severe combined immunodeficient mice. In light of these results, obtained with classical cell biology techniques (i.e., monolayer and static growth conditions), we applied advanced tissue engineering strategies based on the use of a bioreactor to create flow of perfusion medium through the scaffolds and on the presence of supporting cells (such as hepatic stellate cells [ITO] cells) in HLSC cultures in an effort to create a more natural hepatic milieu *in vitro*.

A.3 Material and Methods

A.3.1 Perfusion bioreactor: Mathematical model

We used a perfusion bioreactor in which eight porous scaffolds can be cultured in eight independent chambers. In each chamber the medium flows from top to bottom through a three-dimensional (3D) scaffold. HLSC growth in each scaffold was described using a mathematical model. The model applied in this work was derived from our previous work.[11] Briefly, the geometry of a highly porous scaffold, as the collagen sponge (Avitene Ultrafoam Collagen Hemostat; Davol Inc., Cranston, RI) used in the experiment (Fig. A.1a), was approximated to a cylinder with parallel cylindrical channels and no interconnections (Fig. A.1b). A channel diameter of 200 µm was the mean value used for the distribution, based on microscopic evidence and image analysis of the collagen scaffolds, whereas the total scaffold porosity was the maximum available for this geometry. The model contains a uniform cell layer (Domain II) adhering to the channel wall while the medium flows through the central portion of the channel (Domain I) as exemplified in Figure A.1c. The thickness of the cell layer increases as the cells grow, while the axial velocity of the medium, v_z,

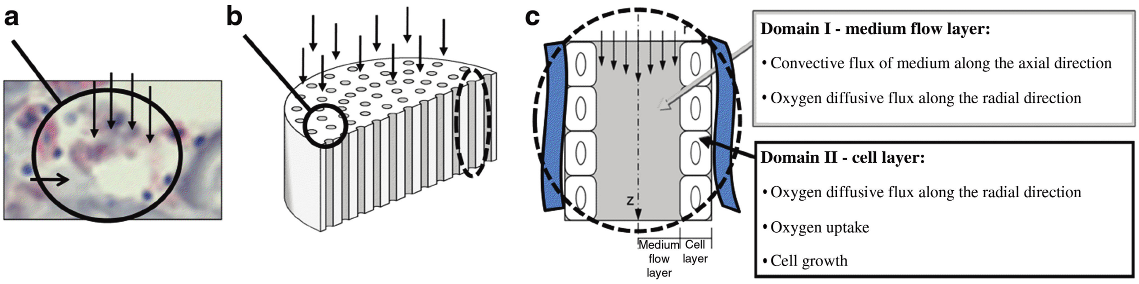

Figure A.1: Bioreactor model. (**a**) *In vitro* image of one channel of the scaffolds used for the mathematical model. Vertical arrows: flow medium direction; horizontal arrows: scaffolds fibers. (**b**) Scheme of the scaffold structure with parallel cylindrical channels considered in the model (the white area is the collagen). Vertical arrows show the direction of medium flow. The circle indicates the area corresponding to **a**. (**c**) Scheme of one channel of the scaffold. Domain I, in gray, is the medium flow layer where the medium flows along the axial coordinate z, while oxygen spreads along the radial coordinate r. Domain II, in white, is the uniform layer of cells adhering to the channel wall. There is no convection of medium in Domain II, but there is oxygen diffusion and uptake. Domain II thickness increases with cell growth. The blue areas are the collagen where cells adhere. Color images available online at www.liebertonline.com/ten.

depends on the total flow rate and the diameter of Domain I. Oxygen was chosen as the reference species because its concentration strongly affects cell growth.[12] The phenomena governing oxygen concentration for each layer, and consequently also cell growth, are summarized in Figure A.1c. Assuming that none of the phenomena depend on angular coordinates, the governing equations were derived for cylindrical geometry in term of axial and radial coordinates as follows:
Domain I: medium flow layer

$$\frac{\partial c^I_{O_2}}{\partial t} = -\left[\frac{1}{r}\frac{\partial}{\partial r}\left(rN^I_{O_2,r}\right)\right] - \frac{\partial N^I_{O_2,z}}{\partial z}, \tag{A.1}$$

$$N^I_{O_2,r} = -D^I_{O_2}\frac{\partial c^I_{O_2}}{\partial r}, \tag{A.2}$$

$$N^I_{O_2,z} = v_z c^I_{O_2}. \tag{A.3}$$

where $c^I_{O_2}$ is the oxygen concentration, $N^I_{O_2,r}$ is the radial diffusive molar flux, and $N^I_{O_2,z}$ is the axial convective molar flux. $D^I_{O_2}$ is the coefficient of oxygen diffusion in the medium and v_z is the medium axial velocity. Velocity profile was assumed to be parabolic.

Domain II: cell layer

$$\frac{\partial c_{O_2}^{II}}{\partial t} = -\left[\frac{1}{r}\frac{\partial}{\partial r}\left(rN_{O_2,r}^{II}\right)\right] + R_{O_2}, \tag{A.4}$$

$$N_{O_2,r}^{II} = -D_{O_2}^{II}\frac{\partial c_{O_2}^{II}}{\partial r}, \tag{A.5}$$

$$R_{O_2} = -\frac{1}{V_{cell}}\frac{Q_m c_{O_2}^{II}}{C_m + c_{O_2}^{II}}, \tag{A.6}$$

$$\frac{dn}{dt} = F k_{cell} c_{O_2}^{II} n, \tag{A.7}$$

$$F = \frac{1}{\pi}\left\{\frac{\pi}{2} + \arctan\left[k_{damp}\left(c_{O_2}^{II} - c_{O_2}^{lim}\right)\left(S\left(z,t\right) - S^{lim}\right)\right]\right\}, \tag{A.8}$$

$$S^{lim} = \left(\frac{4\mu Q_{ch}}{\pi\tau_{shear}}\right)^{1/3}, \tag{A.9}$$

where $c_{O_2}^{II}$ is the oxygen concentration, $N_{O_2}^{II}$ is the radial diffusive molar flux, R_{O_2} is the oxygen uptake rate, $D_{O_2}^{II}$ is the coefficient of oxygen diffusion in the cell layer, n is the total number of cell, Q_m and C_m are parameters depending on the type of cells, and k_{cell} and V_{cell} are the cell doubling time and the cell volume, respectively. F is a inhibitory function that stops the cell growth when oxygen concentration is below the physiological limit $c_{O_2}^{lim}$ (corresponding to 40 mmHg) or when the shear stress is higher than τ_{shear} (0.5 Pa). S_{lim} is the dimension of Domain II corresponding to the limiting shear stress, k_{damp} is the damping coefficient that determines the steepness of variation of F from 1 to 0, μ is viscosity of the medium, and Q is the flow rate in the channel. The oxygen concentration at each channel inlet ($c_{O_2}^{I}$ at $z = 0$) equated to the concentration at equilibrium with air ($c_{O_2,0}$). The initial condition with a uniform oxygen concentration ($c_{O_2}^{I} = c_{O_2}^{II} = c_{O_2,0}$ at $t = 0$) in both domains was applied. The values of the parameters and the respective references are given in Table A.1. The system of equations (A.1), (A.4), and (A.7) was solved using MATLAB (The MathWorks, Natick, MA) by means of the finite volume method. Every channel was discretized in the axial and radial directions.

Table A.1: Model Parameters, the Related Symbols, the Values Used in Simulations, and the Reference Values

Parameter	*Symbol*	*Value*	*Reference*
Cell growth kinetic constant	k_{cell}	$2.55 \times 10^{-5}\,\mathrm{m^3\,mol^{-1}\,s^{-1}}$	27
Cell specific volume	v_{cell}	$4.19 \times 10^{-15}\,\mathrm{m^3\,/cell}$	28
Damping coefficient	k_{damp}	$10\,\mathrm{m^2\,/mol}$	11
Diffusion coefficient oxygen-cell	$D^{II}_{O_2}$	$2.0 \times 10^{-9}\,\mathrm{m^2\,/s}$	29
Diffusion coefficient oxygen-medium	$D^{I}_{O_2}$	$3.29 \times 10^{-9}\,\mathrm{m^2\,/s}$	30
Dissolved oxygen concentration in equilibrium with air	$c_{O_2,0}$	$2.1 \times 10^{-1}\,\mathrm{mol\,/m^3}$	31
Maximal oxygen consumption rate	Q_m	$2.5 \times 10^{-16}\,\mathrm{mol\,cell^{-1}\,s^{-1}}$	32
Medium viscosity	μ	$7.7 \times 10^{-4}\,\mathrm{Pa\,s}$	33
Oxygen concentration at half-maximal oxygen consumption	C_m	$6.9 \times 10^{-3}\,\mathrm{mol\,/m^3}$	32
Threshold oxygen concentration	$c^{lim}_{O_2}$	$5.26 \times 10^{-2}\,\mathrm{mol\,/m^3}$	34
Threshold shear stress	τ_{shear}	$0.50\,\mathrm{Pa}$	35

A.3.2 Cell culture and differentiation protocol

Human liver stem cells. These cells were isolated, purified, and characterized as described by Herrera *et al.*[10] Briefly, HLSCs were obtained by culturing cryopreserved hepatocytes obtained from Lonza Group Ltd., Basel, Switzerland (IRB approval is not required). The cryopreserved cell population was quickly thawed in a 37.1 °C water bath with gentle shaking, and then it was seeded in a flask for cell expansion. Cell viability was determined using Trypan blue exclusion staining. Characterization was done as described by Herrera *et al.*[10] Briefly, immunofluorescence was used to confirm HLSCs purity in cell culture on chamber slides. The absence of CD34, c-kit, and CK19 or markers for nonparenchymal liver cells (alpha-smooth muscle actin [SMA]) confirmed their purity. These assays were randomly performed in triplicate for the cryopreserved vials supplied. HLSCs purity was 98%. HLSCs were expanded in a flask in the presence of hepatic cell medium (HCm): α-minimum essential medium/endothelial cell basal medium-1 (3:1) (from Gibco, Carlsbad, CA/Cambrex, Charles City, IA) supplemented with l-glutamine (5 mM), Hepes (12 mM, pH 7.4), penicillin (50 IU /mL), streptomycin (50 µg /mL), dexamethasone 1 µM, glucagon 0.014 mg /mL, insulin 0.16 U /mL (all from Sigma, St. Louis, MO), fetal calf serum (10%), and horse serum (10%) (from Gibco). For the differentiation experiment, HLSCs were cultured differently with the aforementioned medium (HCm) or with stem cell medium (SCm) Amniomed® Plus (Euroclone, Milan, Italy).

ITO cells. These cells were isolated and characterized using a two-step collagenase perfusion as described by Paik and colleagues.[13] Briefly, ITO cells were obtained by culturing cryopreserved cells obtained from Dr. M. Pinzani's Lab, University of Florence, Florence, Italy (IRB approval is not required). Collected ITO cells were suspended at a concentration of 1×10^5 cells /mL in Dulbecco's modified Eagle's medium supplemented with fetal calf serum (20%), penicillin (50 IU /mL), and streptomycin (50 µg /mL) (all from Sigma) and cultured on well plates coated with collagen type I (10 µg /mL) (from Sigma) in a 5% CO_2 humidified atmosphere.

3D cultures. For all the differentiation experiments, 3D cultures were conducted in a perfusion bioreactor according to the protocol published elsewhere.[14] Briefly, cells between passages 3 and 8 were detached from the flask surface with trypsin-EDTA, washed, and counted; then 5×10^5 cells were seeded onto a collagen sponge[15,16] (Avitene® Ultrafoam™Collagen Hemostat; Davol, Inc.) with diameter 5 mm and thickness 3 mm. Up to eight sponges were seeded for each experiment. On the day after seeding, the sponges were placed, one in each separate chamber, in the bioreactor, which assured a perfusion medium flow rate of 0.5 mL /min through each scaffold.[14] The differentiated conditions used in the bioreactor are shown in Table A.2. All cultures were performed in triplicate; the scaffolds were analyzed at fixed time points, in terms of their biochemical parameters on days 1, 3, 5 and 7, and their morphological features on days 3 and 7.

Table A.2: The Differentiated Conditions Used for Cell Culture in the Perfusion Bioreactor

	Perfusion medium		
	Hepatic cell medium (HCm)	*Stem cell medium (SCm)*	*HCm + SCm (1:1)*
Cell	HLSCs[a]	HLSCs	HLSCs
	ITO[b]	ITO	ITO
	HLSCs + ITO (3:1)	HLSCs + ITO (3:1)	HLSCs + ITO (3:1)

[a] HLSCs, human liver stem cells.
[b] ITO, hepatic stellate cells.

A.3.3 MTT assay

Cell proliferation rates were analyzed by the MTT (3-4,5-dimethylthiazol-2yl-2,5-diphenyltetrazolium bromide)-based cytotoxicity test using the Denizot and Lang method with minor modifications.[17] 3D cell cultures removed from the bioreactor were placed on a culture plate with 1 mL of MTT solution (0.8 mg /mL in phosphate-buffered saline). Cultures were returned to the incubator and the supernatant was discarded after 3 h. Each scaffold was then transferred to an Eppendorf microtube, and 1 mL of extraction solution (0.01 N of HCl in isopropanol) was added. The Eppendorf microtubes were vortexed for 5 min to enable total color release from the scaffolds and then centrifuged at 15.000 g for 5 min, and the optical density of the supernatants was read at 540 nm.

A.3.4 Albumin ELISA assay

Albumin secretion from the HLSCs was determined using ELISA. Samples were harvested daily from the circulating medium and frozen at −20 °C. The albumin concentration was measured using the human albumin AssayMax Human Albumin ELISA (Gentaur, Brussels, Belgium). The minimum detectable dose of albumin with this kit is typically 100 ng /mL.

A.3.5 Histological and morphological analyses

Specimens were fixed in formalin, embedded in paraffin, and stained with hematoxylin and eosin. Cryostatic sections of 7 µm were used for morphological and immunohistochemical analyses. They were layered over gelatine-coated glass slides, fixed with absolute acetone for 10 min at room temperature, and cryopreserved at −20 °C until use. Ck19 on HLSCs was identified using the acid phosphatase anti-acid phosphatase procedure. Reactions were all conducted in humid chambers at room temperature. Briefly, after saturating nonspecific antigen sites with 1:20 rabbit serum in 0.05 M Maleate TRIZMA (pH 7.6; Sigma) for 20 min, the first antibody was added to samples (1:20 mouse anti-human CK19; Dako, Milano, Italy). After incubation for 2 h, the samples were rinsed with buffer solution, and the second antibody was added for 30 min (Link Ab [Dako], rabbit anti mouse). After rinsing again, the sections were incubated for 30 min with 1:50 mouse acid phosphatase anti-acid phosphatase Ab (Dako), then rinsed once more, and finally, reacted for 20 min with Fast Red Substrate (Sigma). Counter staining was done with hematoxylin (Sigma).

A.3.6 Statistical analyses

Values are given as means ± standard deviation. The one-way analysis of variance in the Excel software package was used for data analyses. Statistical significance was assumed when $p < 0.05$.

A.4 Results

A.4.1 Bioreactor model

The bioreactor model was developed as reported in the Material and Methods section (Fig. A.1). We considered the time-dependent profile of cell volume and oxygen concentration along each channel as the main output of the system. Different flow rates have been used in the model: Figures A.2 and A.3 show the results for three of them, that is, 0.1, 0.5, and 2.5 mL /min. The results obtained with the model confirmed that cell growth depends on the flow rate of the medium. Using the lowest flow rate (0.1 mL /min) would enable a rapid cell growth at the channel inlet (Fig. A.2, continuous line) where the oxygen concentration remains higher than 80% of the saturation value. On the other hand, a flow rate of 0.1 mL /min would not be able to avoid an oxygen gradient forming along the length of the channel: the O_2 concentration would decrease moving from the inlet to the outlet of the channel. The concentration at the outlet of the channel (dotted and dashed line in Fig. A.2) would drop to the near-critical level of 5.26×10^{-2} mol /m^3 after 7 days of culture. This oxygen gradient would lead to a slower cell growth rate in the central and bottom portions of the scaffold (dashed lines, and dotted and dashed lines) and consequently to an uneven distribution of the cell volume in the z-direction. A flow rate of 0.5 mL /min would be able to maintain the oxygen concentration above 80% of the saturation value through the channel. However, the oxygen gradient would be still present since few days of culture and it would correlate closely with

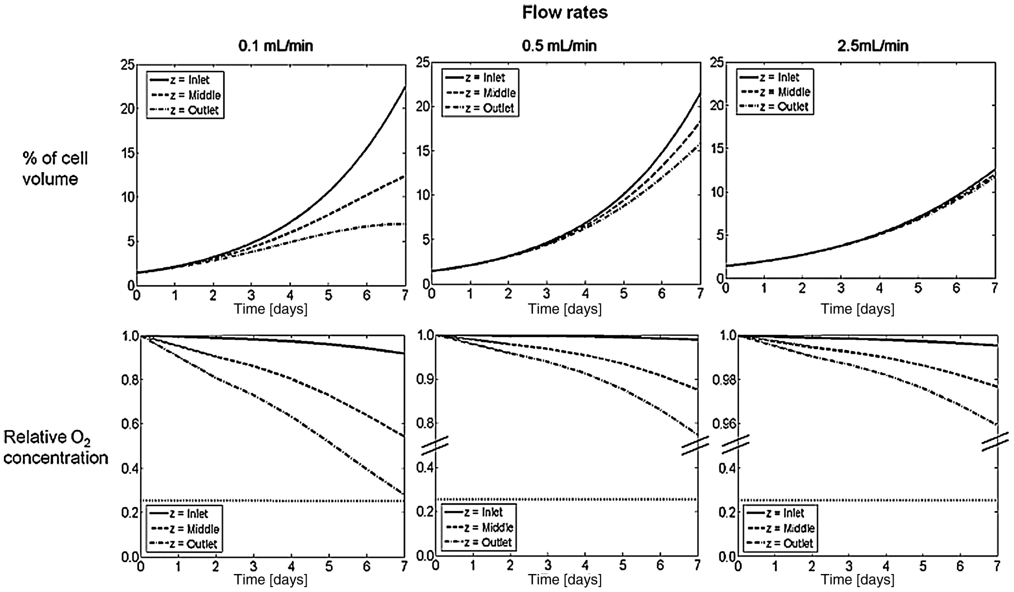

Figure A.2: Time variation of the percentage of volume occupied by the cell (upper line) and the O_2 concentration related to the saturation value (bottom line). Data are given for three flow rates, that is, 0.1 mL /min (left), 0.5 mL /min (center), and 2.5 mL /min (right). Each graph shows the data for three z-coordinates, that is, at each channel's inlet (continuous line), midline (dashed line), and outlet (dashed and dotted line). The horizontal dotted line in the O_2 graphs corresponds to the threshold oxygen concentration of 5.26×10^{-2} mol /m^3.

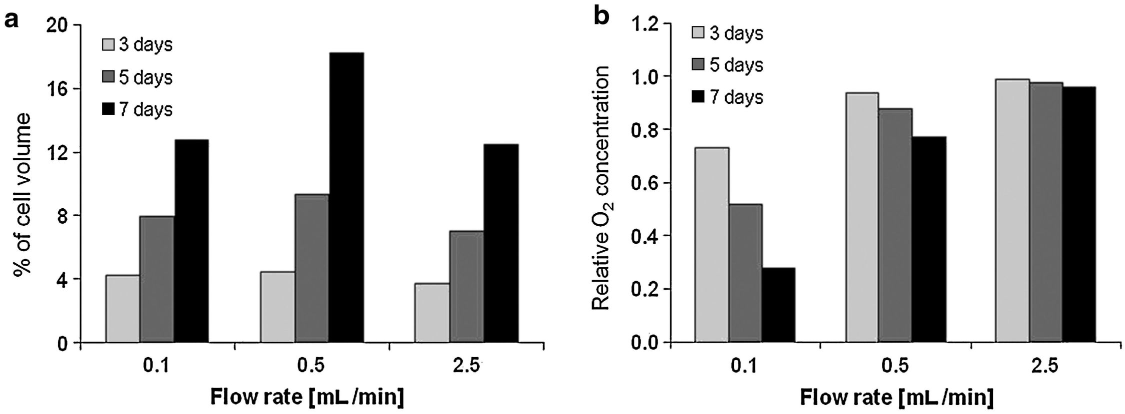

Figure A.3: Percentage of mean cell volume (**a**) and minimum O_2 concentration reached in relation to the saturation value (**b**) for three flow rates, that is, 0.1, 0.5, and 2.5 mL /min. Data are given at three time points, after 3 days (light gray), 5 days (dark gray), and 7 days (black).

a gradient in the percentage cell volume. Increasing the flow rate would lead to a more homogeneous cell volume and oxygen concentration along the z-direction (Fig. A.2). However, it also induced a high shear stress on the cell surface, which could reduce the cell growth rate (Fig. A.3). Figure A.3 shows the prediction model for the mean percentage of volume occupied by the cells in the whole scaffold for three time points and the three flow rates. For short-term hepatocyte culture, a low flow rate (around 0.5 mL /min and below) could give rise to the highest percentage cell volume because the mean oxygen concentration does not strongly depend on the flow rate when the cell volume is low. For longer-term culture (5 days or more), an optimal flow rate (around 0.5 mL /min) achieved the highest mean percentage cell volume. Still, as shown in Figure A.2, a uniform cell growth in the z-direction can only be obtained with a flow rate of 2.5 mL /min or more. We considered a flow rate of 0.5 mL /min as the best choice for maintaining high cell growth rate with moderate heterogeneity in the cell distribution.

A.4.2 Morphological analyses

Figure A.4 (left column) shows the morphological features of the HLSCs cultivated in the presence of HCm on day 3, in the previously described dynamic cell culture conditions (0.5 mL /min). In these conditions, the cells have clearly become organized into clusters inside the small compartments of the sponge. The cells are able to retain their phenotype, as confirmed by the red staining (showing positivity) for the biliary marker (CK19) and by the presence of double-nucleated cells (cells inside the circle). The direction of the flow of medium is indicated by white arrows, while the presence of biomaterial fibers (horizontal black arrows) indicates the organization of the small compartments in which the HLSCs could become organized into liver-like tissue. Figure A.4 (right column) shows the 7-day cell cultures. Here again, the cells were stained with classic hematoxylin and eosin and immunostained for biliary markers (CK19; red cells). The cultured cells initially seeded on the surface coinciding with the inlet for the flow of medium (white arrows) soon started to become organized into multiple layers, migrating through the collagen sponge (horizontal arrows). By day 7 (Fig. A.4), some clusters appeared to be trapped inside the

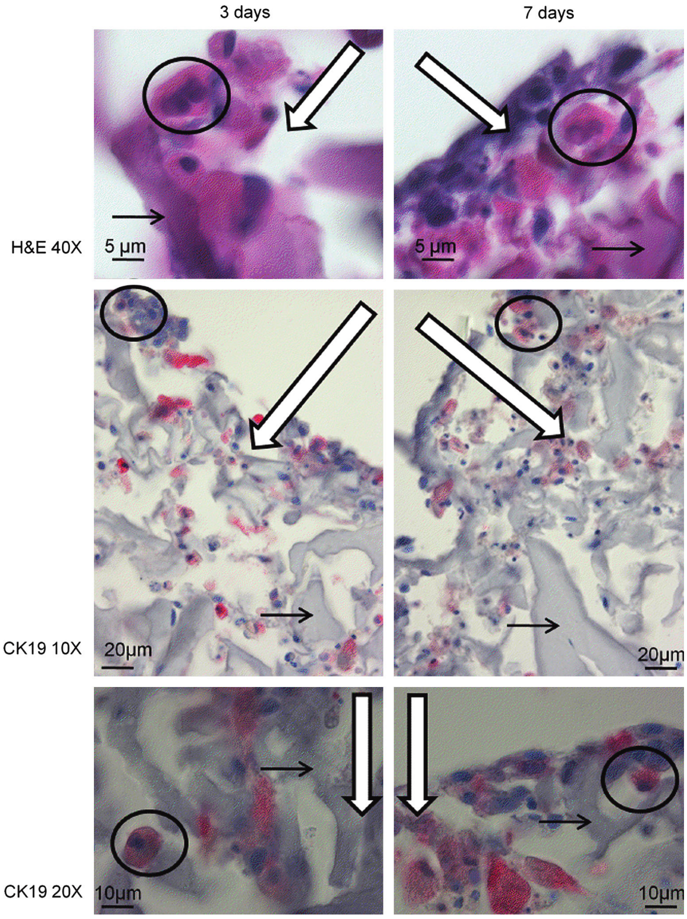

Figure A.4: Morphological analyses of HLSCs on a three-dimensional scaffold in different flow conditions on days 3 (left) and 7 (right). Cells are stained with classical H&E and biliary markers (CK19) (red cells). White arrows: direction of flow of medium; horizontal black arrows: collagen fibers. Circles: double nucleated cells. HLSC, human liver stem cell; H&E, hematoxylin and eosin. Color images available online at www.liebertonline.com/ten.

sponge (red cluster), showing layered cells in the holes in the sponge. The differentiated phenotype showed a "hexagonal shape" often associated with double nuclei (cells inside the circle) in contrast to the flat shape initially seen, characteristic of monolayer cultures (data not shown).

A.4.3 Proliferation test

Cells seeded onto the sponge were cultivated inside the bioreactor for up to 7 days under different conditions, based on the type of medium (hepatic cell selective, stem cell selective, or both), the type of cell (HLSC, ITO, or both), and combinations of the two (see Material and Methods section). Biological parameters were tested on days 1, 3, 5, and 7, for example, the MTT was used to detect the proliferation rate and albumin was quantified to establish differentiation status. The proliferation rate (as detected with the MTT) is shown in Figure A.5a, where it is clear that cells survived up to day 7 in all culture conditions (i.e., there was no drop in MTT values), confirming the good functionality of the bioreactor. In more detailed analyses, we found there was no detectable increase in the MTT value during the days of culture when HLSCs were cultured alone; a slight increase was only visible when SCm was used. A higher increase in MTT values over time was observable in scaffolds containing ITO cells alone or HLSC and ITO cocultures, irrespective of the combination of perfusion media used. The greatest improvement in cell proliferation rate was obtained when HLSC and ITO cocultures were run in the presence of SCm. The proliferation rate of ITO cultures showed a marked increase in the MTT result, characteristic of the biology of nonparenchymal cell types.

A.4.4 Albumin production

Having established that a continuous flow of medium through the bioreactor is able to sustain cell viability, we investigated liver functionality. Secreted albumin levels for each of the above-described culture conditions were determined by ELISA in samples of medium. Extracted DNA values from the cellularized scaffolds in the different culture conditions were used to normalize all functional results. Results in Figure A.5b confirm that albumin was synthesized by the liver cells grown in the bioreactors throughout the experiment. We compared the ability of HLSCs to maintain protein synthesis in the different culture conditions in the perfusion bioreactors (Fig. A.5b). HLSCs cultured alone showed an albumin production strongly related to the medium involved, the presence of SCm giving rise to a higher production. The same trend was evident in coculture, where a higher albumin secretion again coincided with the presence of SCm medium. There was naturally no albumin production detectable in the culture containing ITO (nonparenchymal cells) alone.

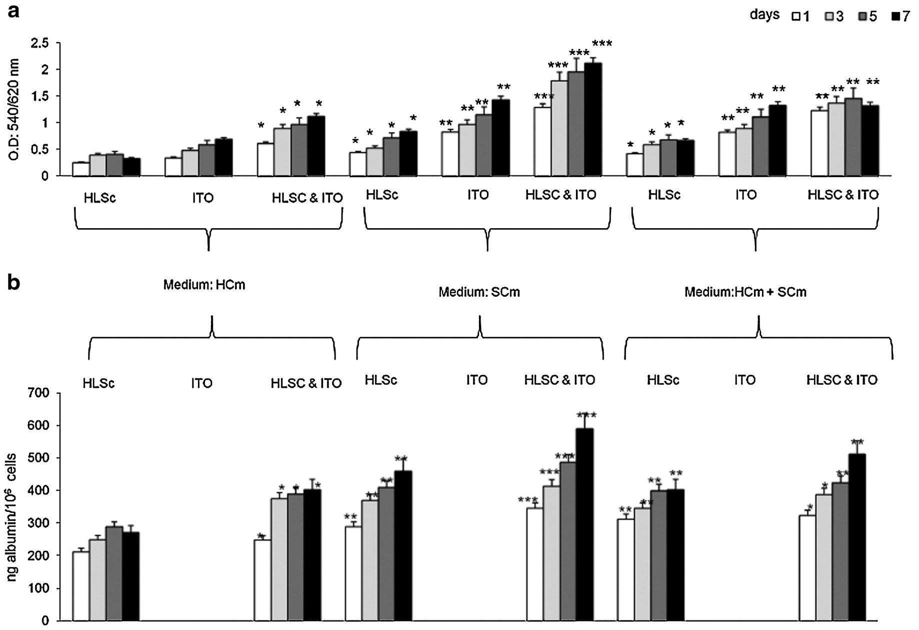

Figure A.5: (**a**) MTT tests for proliferative activity was performed on days 1, 3, 5, and 7 in HCm (hepatic cell medium), SCm (stem cell medium), and HCm + SCm (hepatic cell + stem cell media). Using analysis of variance, data were compared with HLSCs in HCm on the same day ($*p < 0.05$, $**p < 0.01$, $***p < 0.001$). (**b**) Albumin secretion was assayed for HLSCs alone, ITO cells alone, and HLSC + ITO cell cultures in the bioreactor (no albumin secretion was detected in ITO cell cultures). Using analysis of variance, data were compared with HLSCs in HCm on the same day ($*p < 0.05$, $**p < 0.01$, $***p < 0.001$).

A.5 Discussion

With a view to develop an efficient differentiation method to improve the commitment of adult precursor liver cells to mature hepatic cells, we optimized the culture method by using a 3D culture system in a perfusion bioreactor and testing several combinations of cell cultures (HLSC, ITO, and both) and media (HCm, SCm, and both). The first issue to consider was the well-known biological behavior of primary hepatocytes[18]: because of their high metabolic activity *in vivo*, their survival relies on an extensive vascularization to ensure an adequate nutrient and waste exchange.[19–21] With this in mind, our experiments were conducted in dynamic culture conditions using a perfusion bioreactor. This system enabled us to simultaneously and separately culture eight porous scaffolds, ensuring an accurate control of the flow rate of medium through each scaffold.[14] The results obtained with the mathematical model were used to decide a flow rate *a priori*, which was set to

0.5 mL /min for up to 7 days. In these conditions, HLSCs in the presence of HCm not only showed a good proliferation rate (Fig. A.5a, first histogram group from the left) and a marked clustering within the collagen scaffolds (horizontal black arrows in Fig. A.4), but also a good phenotype resembling mature hepatocytes, confirmed by positivity for a biliary marker such as CK19 (red cells in Fig. A.4), the presence of double-nucleated cells (cells inside the circle in Fig. A.4), and albumin secretion (Fig. A.5b). Encouraged by these results, we focused on developing a system to improve the proliferation rate and differentiated status of the HLSC population. Our strategy was based on using a commercial SCm capable of influencing the stem cell biology of the undifferentiated cells in the HLSC population and cocultivating the HLSCs with a supporting cell population (ITO); the latter solution was prompted by evidence that 3D coculture models involving parenchymal and nonparenchymal cells can mimic the plate organization of the liver parenchyma, holding promise for the reconstitution of the structure and matrix geometry of the hepatic microenvironment. Interaction between HLSCs and ITO cells may have an important role, for instance, in modulating cell growth, migration, and differentiation.[22–26] The cultures obtained with different combinations of cells and media were analyzed according to their proliferation rate and their ability to secrete albumin (Fig. A.5). In detail, our results could be explained in the following text.

A.5.1 Hepatic cell medium

This medium induces a lower proliferation rate and smaller albumin production in all cell cultures. No albumin production is detectable on ITO cultures (Fig. A.5b), which shows that there are no hepatic progenitors in the ITO cell population. The coculture system with HLSCs and ITO cells showed the highest proliferation rate and greatest albumin production ($p < 0.05$ compared with HLSCs alone at the same time point). This might be due to a positive interaction between the stem cell population inside the HLSCs and the ITO cells.

A.5.2 Stem cell medium

In HLSC cultures, this medium induced a small increase in the MTT value by comparison both with different time points in the same culture and with the same time points in culture with HCm ($p < 0.05$; Fig. A.5a). The same trend was seen in the effect on albumin production, but the differences were much more evident ($p < 0.01$ compared with HLSCs in HCm; Fig. A.5b); this could be due to the activation of the undifferentiated stem cell population in the HLSCs. There was a clearly evident, considerable increase in the MTT value for the ITO cultures ($p < 0.01$); as mentioned previously, ITO cells are unable to produce albumin. In cocultures (HLSC and ITO), the presence of SCm induced a higher proliferation rate and a greater albumin production ($p < 0.001$ compared with HLSCs alone in HCm), probably because of a positive interaction between HLSCs and ITO cells.

A.5.3 Stem cell and hepatic media

This medium had a better effect on differentiation than on proliferation: the HLSC proliferation rate in the coculture stopped around day 5, whereas albumin was also produced during the last days of culture, with rising albumin concentrations. As in the other two cases, when this medium was used the best results in terms of MTT value and albumin production were obtained with the HLSC and ITO coculture. In this particular case, ITO cells proved capable of enhancing the differentiation of precursor hepatic progenitors. Our data showed that the hepatocytes exhibited a differentiated morphology and much higher levels of mature functions, such as albumin secretion, when compared with the monoculture system (in which only hepatocytes were cultured) in the same condition. In addition, the higher values of the MTT test (Fig. A.5a) of cocultures compared with the results of hepatocytes or ITO cells alone, independent of the medium, indirectly support our hypothesis. However, as revealed by proliferation rate, it is evident that cells survived up to day 7 in every culture condition; then a tendency for the initial tissue-like structures to degrade started. This event could be likely related to the progressive death of ITO cells, unable to further support hepatocytes. Thus, we came to the conclusion that ITO cells are initially able to modulate the differentiation of HLSCs in cocultures either by direct cell contacts or via soluble factors in the medium. In the light of these results, we can confirm that a combination of the SCm with a coculture including ITO cells definitely increased both cell proliferation and cell maturation. In conclusion, HLSCs were induced to proliferate as cells with hepatic characteristics by creating and enhancing a mutual synergism with the medium and with neighboring nonparenchymal cells. Our findings demonstrate the feasibility of this protocol for the differentiation and amplification of HLSCs as a useful source for cell transplantation as well as for use in pharmaceutical and toxicological investigations.

A.6 Acknowledgments

This study received partial funding from the University of Padova, Italy, and a grant from Fresenius Medical Care. The authors thank Professor Massimo Pinzani for kindly providing ITO cells.

A.7 Disclosure Statement

M.B. Herrera is the named inventor on a related patent application concerning liver stem cells. C. Tetta is a full-time employee of Fresenius Medical Care (Deutschland). U. Cillo has a financial interest in Fresenius Medical Care.

A.8 References

1. Lee, W.M., Squires, R.H., Jr., Nyberg, S.L., Doo, E., and Hoofnagle, J.H. Acute liver failure: summary of a workshop. Hepatology **47**, 1401, 2008.

2. Yu, C.B., Pan, X.P., and Li, L.J. Progress in bioreactors of bioartificial livers review. Hepatobiliary Pancreat Dis Int **8**, 134, 2009.

3. van de Kerkhove, M.P., Poyck, P.P., Deurholt, T., Hoekstra, R., Chamuleau, R.A., and van Gulik, T.M. Liver support therapy: an overview of the AMC-bioartificial liver research. Dig Surg **22**, 254, 2005.

4. Morsiani, E., Brogli, M., Galavotti, D., Pazzi, P., Puviani, A.C., and Azzena, G.F. Biologic liver support: optimal cell source and mass. Int J Artif Organs **25**, 985, 2002.

5. van de Kerkhove, M.P., Hoekstra, R., Chamuleau, R.A., and van Gulik, T.M. Clinical application of bioartificial liver support systems. Review. Ann Surg **240**, 216, 2004.

6. Chamuleau, R.A., Poyck, P.P., and van de Kerkhove, M.P. Bioartificial liver: its pros and cons. Review. Ther Apher Dial **10**, 168, 2006.

7. Rozga, J. Liver support technology—an update. Review. Xenotransplantation **13**, 380, 2006.

8. Catapano, G., Patzer, J.F., 2nd, and Gerlach, J.C. Transport advances in disposable bioreactors for liver tissue engineering. Adv Biochem Eng Biotechnol **115**, 117, 2010.

9. Tilles, A.W., Berthiaume, F., Yarmush, M.L., and Toner, M. Critical issues in bioartificial liver development. Review. Technol Health Care **10**, 177, 2002.

10. Herrera, M.B., Bruno, S., Buttiglieri, S., Tetta, C., Gatti, S., Deregibus, M.C., Bussolati, B., and Camussi, G. Isolation and characterization of a stem cell population from adult human liver. Stem Cells **24**, 2840, 2006.

11. Flaibani, M., Magrofuoco, E., and Elvassore, N. Computational modeling of cell growth heterogeneity in a perfused 3D scaffold. IECR **49**, 859, 2010.

12. Lewis, M., MacArthur, B., Malda, J., Pettet, G., and Please, C. Heterogeneous proliferation within engineered cartilaginous tissue: the role of oxygen tension. Biotechnol Bioeng **91**, 607, 2005.

13. Paik, Y.H., Schwabe, R.F., Bataller, R., Russo, C., Jobin, C., and Brenner, D.A. Toll-like receptor 4 mediates inflammatory signalling by bacterial lipopolysaccharide in human hepatic stellate cells. Hepatology **37**, 1043, 2003.

14. Flaibani, M., Luni, C., Sbalchiero, E., and Elvassore, N. Flow cytometric cell cycle analysis of muscle precursor cells cultured within 3D scaffolds in a perfusion bioreactor. Biotechnol Prog **25**, 286, 2009.

15. Cannizzaro, C., Tandon, N., Figallo, E., Park, H., Gerecht, S., Radisic, M., Elvassore, N., and Vunjak-Novakovic, G. Practical aspects of cardiac tissue engineering with electrical stimulation. Methods Mol Med **140**, 291, 2007.

16. Cimetta, E., Flaibani, M., Mella, M., Serena, E., Boldrin, L., Coppi, P.D., and Elvassore, N. Enhancement of viability of muscle precursor cells on 3D scaffold in a perfusion bioreactor. Int J Artif Organs **30**, 415, 2007.

17. Denizot, F., and Lang, R. Rapid colorimetric assay for cell growth and survival. J Immunol Methods 89, 271, 1986. 18. Allen, J.W., and Bhatia, S.N. Engineering Liver therapies for the future. Review. Tissue Eng **8**, 725, 2002.

19. Eschbach, E., Chatterjee, S.S., Nöldner, M., Gottwald, E., Dertinger, H., Weibezahn, K.F.,

and Knedlitschek, G. Microstructured scaffolds for liver tissue cultures of high cell density: morphological and biochemical characterization of tissue aggregates. J Cell Biochem **95**, 243, 2005.

20. Mith, M.K., Riddle, K.W., and Mooney, D.J. Delivery of hepatotrophic factors fails to enhance longer-term survival of subcutaneously transplanted hepatocytes. Tissue Eng **12**, 235, 2006.

21. Chan, C., Berthiaume, F., and Nath, B.D. Hepatic tissue engineering for andjunct and temporary liver support: critical technologies. Review. Liver Transplant **10**, 1331, 2004.

22. Zavan, B., Brun, P., Vindigni, V., Amadori, A., Habeler, W., Pontisso, P., Montemurro, D., Abatangelo, G., and Cortivo, R. Extracellular matrix-enriched polymeric scaffolds as a substrate for hepatocyte cultures: *in vitro* and *in vivo* studies. Biomaterials **26**, 7038, 2005.

23. Sugimoto, S., Mitaka, T., and Ikeda, S. Morphological changes induced by extra-cellular matrix are correlated with maturation of rat small hepatocytes J Cell Biochem **87**, 16, 2002.

24. Harada, K., Mitaka, T., Miyamoto, S., *et al.* Rapid formation of hepatic sinusoid in collagen sponge by rat small hepatocytes and hepatic non parenchymal cells. J Hepatol **39**, 716, 2003.

25. Sudo, R., Iked, S., and Sugimoto, S. Bile canalicular formation in hepatic organoid reconstructed by rat small hepatocytes and nonparenchymal cells. J Cell Physiol **199**, 252, 2004.

26. Benten, D., Kumaran, V., Joseph, B., Schattenberg, J., Popov, Y., Schuppan, D., and Gupta, S. Hepatocyte transplantation activates hepatic stellate cells with beneficial modulation of cell engraftment in the rat. Hepatology **42**, 1072, 2005.

27. Schmelzer, E., Zhang, L., Bruce, A., Wauthier, E., Ludlow, J., Yao, H., Moss, N., Melhem, A., McClelland, R., Turner, W., Kulik, M., Sherwood, S., Tallheden, T., Cheng, N., Furth, M.E., and Reid, L.M. Human hepatic stem cells from fetal and postnatal donors. J Exp Med **204**, 1973, 2009.

28. De Bartolo, L., Morelli, S., Rende, M., Campana, C., Salerno, S., Quintiero, N., and Drioli, E. Human hepatocyte morphology and functions in a multibore fiber bioreactor. Macromol Biosci **7**, 671, 2007.

29. MacPherson, J., O'Hare, D., Unwin, P., and Winlove, C. Quantitative spatially resolved measurements of mass transfer through laryngeal cartilage. Biophys J **73**, 11, 1997.

30. Chow, D., Wenning, L., Miller, W., and Papoutsakis, E. Modeling pO2 distributions in the bone marrow hematopoietic compartment. I. Krogh's model. Biophys J **81**, 10, 2001.

31. Zhao, F., Pathi, P., Grayson, W., Xing, Q., Locke, B.R., and Ma, T. Effects of oxygen transport on 3-D human mesenchymal stem cell metabolic activity in perfusion and static cultures: experiments and mathematical model. Biotechnol Prog **21**, 1269, 2005.

32. Ledezma, G.A., Folch, A., Bhatia, S.N., Balis, U.J., Yarmush, M.L., and Toner, M. Numerical

model of fluid flow and oxygen transport in a radial-flow microchannel containing hepatocytes. J Biomech Eng **121**, 58, 1999.

33. Moreira, J., Santana, P., Feliciano, A., Cruz, P., Racher, A., Griffiths, J., and Carrondo, M. Effect of viscosity upon hydrodynamically controlled natural aggregates of animal cells grown in stirred vessels. Biotechnol Prog **11**, 9, 1995.

34. Mehta, G., Mehta, K., Sud, D., Song, J.W., Bersano-Begey, T., Futai, N., Heo, Y.S., Mycek, M.-A., Linderman, J.J., and Takayama, S. Quantitative measurement and control of oxygen levels in microfluidic poly(dimethylsiloxane) bioreactors during cell culture. Biomed Microdevices **9**, 123, 2007.

35. Tanaka, Y., Yamato, M., Okano, T., Kitamori, T., and Sato, K. Evaluation of effects of shear stress on hepatocytes by a microchip-based system. Meas Sci Technol **17**, 3167, 2006.

Appendix B

Computational Modeling of Cell Growth Heterogeneity in a Perfused 3D Scaffold

Marina Flaibani, Enrico Magrofuoco, and Nicola Elvassore*

Department of Chemical Engineering Principles and Practice, Università degli Studi di Padova,
Via Marzolo, 9, I-35131 Padua, Italy
*Corresponding author

Industrial & Engineering Chemistry Research
Volume 49, Number 2, 2010

DOI: 10.1021/ie900418g

B.1 Abstract

Our goal was to develop a computational model describing the spatiotemporal evolution of cell heterogeneity within a three-dimensional porous scaffold during cell growth in a perfusion bioreactor. The scaffold was assumed formed by an ensemble of independent parallel cylindrical channels with a defined diameter distribution. The total flow rate partitioning in each channel depends on the effective diameter, which is reduced by the cell growth on the channel wall. The mass balance for one metabolite and the cell volume balance were solved. For each channel diameter, the model simulation provide the spatiotemporal evolution of velocity, shear stress, metabolite concentration, and cell volume growth. In particular, all of these outcomes can be analyzed as a function of channel diameter providing an evaluation of cell property heterogeneity. The model describes that the cell growth can be substantially different in each channel diameter. For instance, in the small diameter channel, cell growth is limited by metabolite mass transport, whereas in the larger diameter channel, shear stress inhibits cell growth. This mathematical model could be an important tool for a priori estimation of the time variation of the cell volume fraction and its degree of heterogeneity as a function of operational parameters and scaffold pore size distribution.

B.2 Introduction

In vivo, cells are part of a three-dimensional (3D) complex multiscale organization that starts from small cell clusters, and extends to tissues, and to large volume organs. The correct operation of an organ depends on the single cell behavior that is affected by the cell microenvironment defined by mass transport phenomena of biochemical species, mechanical and hydrodynamic stimuli, biochemical and electrical signals, and physical interaction with the neighboring cells.[1] On the other hand, conventional *in vitro* cell culture is based on a two-dimensional (2D) cell culture system where many of the complex *in vivo* stimuli and interactions can be altered or not properly reproduced. Therefore, there is a pressing need of scaling cell culture systems from the 2D to 3D environment to more closely recreate the behavior of the tissue *in vivo*, which may better simulate *in vivo* biology, physiology, or physiopathology.[2–4] The main challenge of 3D cultures is the accomplishment of a controllable and homogeneous cell behavior within the entire 3D volume. The cell behavior is characterized by both an intrinsic variability correlated with the properties of the cell itself and an extrinsic variability related to the microenvironmental properties.[5,6] These two sources of variability can both induce heterogeneity of cell fate within the 3D domain, leading to an undesired nonhomogeneous 3D culture structure. The intrinsic variability depends only on the cell source and cannot be controlled during the culture, whereas the extrinsic variability can be minimized by strictly controlling the microenvironmental properties that depend on the experimental setup used for culturing the cells. *In vitro* 3D culture systems are characterized by two main components that distinguish from 2D culture: the 3D-like substrates, named scaffolds, where the cells grow, and the technological devices, bioreactors, designed for dynamic cultures. Scaffolds of different shapes, structures, and materials have been realized and studied.[7,8] Among the different types, the polymeric porous scaffolds are usually preferred for long-term culture of adherent cells. The cells adhere to the internal wall of the scaffold channel; therefore, the scaffold structure, morphology, and porosity at macro- and microscale are important parameters that contribute to define the cell microenvironment, that is, the metabolic and regulatory cell activity. Bioreactors with different characteristics and functionality have been developed for the 3D cell culture in the past years.[9,10] One of the most promising systems for cell culture in 3D porous scaffolds is the direct perfusion bioreactor; in this experimental setup, the medium flows through the scaffold channels.[11,12] The medium perfusion influences mass transport, hydrodynamic, and mechanical stimuli, defining cell microenvironment properties. As a consequence, the properties of the cell microenvironment could be modified by tuning operative variable, such as total flow rate. Moreover, the scaffold geometry and the bioreactor flow rate affect the microenvironment properties and their homogeneity because: (a) the total flow splits between channels of different diameters depending on the pore size distribution, which is subject to changes with cell growth; and (b) concentration gradients of metabolites and growth factors result from the combination between cell uptake and mass transport limitations.[13] A rational understanding of the correlation between scaffold geometry, operative variables, and culture conditions at microscale level is extremely relevant for the 3D culture optimization. The knowledge of this correlation would allow one to control the influence of these parameters on the cell volume, the cell behavior, and the cell homogeneity within the entire 3D domain. Mathematical models are useful tools for correlating measurable macroscopic variables to the microscale properties and therefore for interpreting experimental results, identifying the dominating mechanisms, and understanding the biological phenomena. Over the last years, an increasing number of mathematical models focused on cell growth and nutrient transport and consumption in 3D constructs have been developed.[13] They have a fundamental role in helping people to understand mass transport[14−19] and fluid dynamics in biological systems,[10,20] in developing imaging techniques,[21,22] and in optimizing culture by design of experiments.[23] Furthermore, predictive modeling offers huge potential in the optimization of culture conditions and the design of experimental protocols.[13] The models described above have limits of either analyzing the steady-state condition (thus neglecting cell growth)[16,19,24] or neglecting some mass transport phenomena[14,16,17,25] or not considering the geometrical heterogeneousness of the system, which can lead to heterogeneous culture conditions.[14,15,26] The purpose of this Article is to develop a computational model able to describe not only the cell growth but also the cell heterogeneity by simulating the spatiotemporal evolution of microenvironment properties within the 3D scaffold domain. In particular, we aimed to take into account the heterogeneity of the scaffold pore diameters, which is defined through an average pore size and an associated pore size distribution. Using our mathematical model, we investigated the time-evolution of cell volume heterogeneity as a function of scaffold geometry such as the channel diameter distribution and operational parameters such as the volumetric flow rate.

B.3 Methods

Theoretical Framework. Typical experimental setup of a perfusion bioreactor is composed of four units: peristaltic pump, gas exchanger, medium reservoir, and culture chamber. The peristaltic pump is a volumetric pump that allows us to control the medium flow rate through the scaffold independently from the pressure drop. The gas exchanger is required to saturate the oxygen and carbon dioxide concentration in the medium. The culture chamber holds the scaffold used for the 3D cell culture. In this 3D configuration, the medium is constrained to flow through the scaffold. The scaffold is normally formed by porous materials with defined porosity, pore size dimension, and distribution; these pores are usually interconnected to form channels with different size and length. We are mainly interested in studying the effect of local mass transport properties on cell growth heterogeneity; consequently, in our model we assumed that the scaffold is formed by an ensemble of independent parallel oriented channels with defined diameter size distribution as shown in Figure B.1A. Under this assumption, the flow rate entering the scaffold is partitioned according to the principle that the pressure drop must be the same for all channels (iso-headloss condition). Hence, the specific flow rate in each single channel of the scaffold is established by the effective channel diameter shown in Figure B.1B. The cell layer growth adhering to the wall of the scaffold channels, as a result the region where the medium flows, is reduced. In our model, the effective channel diameter represents the difference between the scaffold channel diameter and the thickness of the cell layer. We defined two domains: domain I, the medium region, and domain II, the cell layer. The effective diameter changes due to the cell growth, and the flow is repartitioned according to the iso-pressure drop principle. In a single channel, the cell growth is regulated by the local metabolite availability or hydrodynamic stresses. Among different biochemical and mechanical stimuli, our work assumes that the oxygen plays a major role in influencing the cell growth. This biological hypothesis is supported by many contributions reporting oxygen influence in cell growth in perfusion bioreactors.[27] On the other hand, we assumed that the hydrodynamic shear stress must be taken into account for high medium velocity that is likely to appear for high cell density; in this case, the reduction of the effective diameter leads to higher medium flow under the constriction of constant overall flow rate imposed by the peristaltic volumetric pump. This latter phenomena is particular relevant in inhibiting the cell growth;[28] for this reason, we assumed that local shear stress values greater than a defined threshold value strongly reduce the cell growth.[29] Figure B.1C summarizes all phenomena our model takes into account, all of the variables and the relations between each of them distinguishing among the two domains and their interface. The total flow rate Q_{tot} is partitioned between all channels, resulting in specific channel flow rate Q_{ch}. The medium having oxygen concentration, $c^{I}_{O_2}\left(r,z,t\right)$, flows inside the channel with velocity field, $v_z\left(r,z,t\right)$. The oxygen diffuses along

B. COMPUTATIONAL MODELING OF CELL GROWTH HETEROGENEITY IN A PERFUSED 3D SCAFFOLD

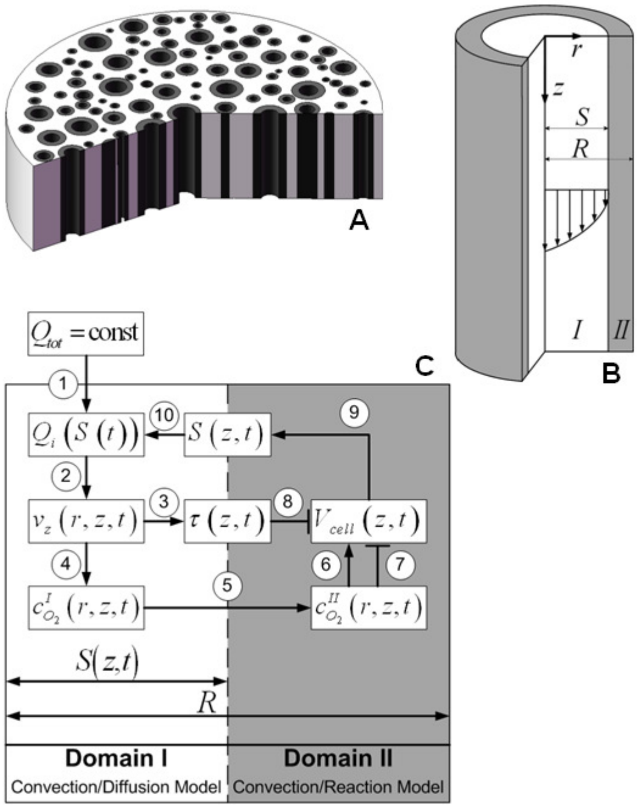

Figure B.1: Representation of the geometry and the phenomena considered in the model. (A) The scaffold structure is a cylinder crossed by several cylindrical parallel channels with a Gaussian distribution of diameters. (B) Every single channel is characterized by an external radius R. It is composed of two regions, the medium domain (domain I, white) with radius $S(z,t)$, and the cellular domain (domain II, gray). The arrows show the parabolic profile of medium velocity in domain I. (C) Bidimensional representation of the phenomena, the variables, and their relations that our model takes into account; domain I is on the left (convection diffusion model, white), while domain II is on the right (diffusion reaction model, gray). The total volumetric flow rate, Q_{tot}, is partitioned between all channels (1) creating a convective flux with axial velocity v_z (2). It generates both a shear stress on the cell surface (3) and an oxygen concentration profile in domain I (4). Oxygen diffusion in the cell domain (5) is induced by the gradient generated by the cell metabolism (6). Oxygen concentration in domain II affects the cell growth that modifies the thickness of both domain (9), causing the redistribution of the total flow rate between all channels (10). The cell growth can be stopped by an oxygen concentration under the physiological value (7) and/or by a high shear stress value on the cell surface (8).

the radial direction toward the domain II where cell uptake decreases the oxygen concentration in domain II ($c^{II}_{O_2}(r,z,t)$). Oxygen depletion causes reduction of the cell growth rate. However, the cell volume, $V_{cell}(z,t)$, modifies the effective channel diameter ($2S(z,t)$), altering the specific channel flow rate and, consequently, the oxygen mass transport and the hydrodynamic shear stress, $\tau(z,t)$.

Mathematical Model. The diameter distribution of the channels is described by a Gaussian distribution. The Fanning equation[30] provides the flow rate in a single channel, Q_{ch}, as a function of the pressure drop, ΔP:

$$Q_{ch} = \frac{\pi D_{ch}^4 \Delta P}{128 \mu L_{ch}}, \tag{B.1}$$

where μ is the medium viscosity, and L_{ch} and D_{ch} are the channel length (which corresponds to the height of the scaffold) and channel diameter. The partitioning of the flow rate between channel with different diameters must satisfy the overall mass balance:

$$Q_{tot} = \sum_k p(D_k) Q_k, \tag{B.2}$$

p_k is the probability from Gaussian distribution for the $k-th$ channel diameter (D_k). Combining eqs (B.1) and (B.2), the volumetric flow rate distribution is obtained. The following section describes the development of the single channel model, which was solved for each channel diameter. The governing equation for domain I was solved in the range $0 < r < S(z,t)$, while the governing equations for domain II were solved in the range $S(z,t) < r < R$, where R is the channel radius and $S(z,t)$ is the effective channel radius (Figure B.1B); $R - S(z,t)$ is the cell layer thickness. For both domains, the governing equations are derived for cylindrical geometry, and they are expressed in terms of radial and axial coordinate; we assumed that all phenomena are angular coordinate independent. For domain I, assuming that the convective flux is relevant only in axial direction and the diffusive flux in the axial direction is negligible as compared to the convective flux (Peclet number ¿ 1), the oxygen mass balance follows:

$$\frac{\partial c^I_{O_2}}{\partial t} = -\left[\frac{1}{r}\frac{\partial}{\partial r}\left(r N^I_{O_2,r}\right)\right] - v_z(r,t)\frac{\partial c^I_{O_2}}{\partial z}, \tag{B.3}$$

where $N^{I}_{O_2,r}$ is the diffusive molar flux in the radial direction. For domain II, assuming diffusion only along radial coordinate, the oxygen mass balance follows:

$$\frac{\partial c^{I}_{O_2}}{\partial t} = -\left[\frac{1}{r}\frac{\partial}{\partial r}\left(rN^{I}_{O_2,r}\right)\right] + R_{O_2}, \tag{B.4}$$

where R_{O_2} is the oxygen uptake rate. The previous eqs (B.3) and (B.4) must be coupled with the constitutive equations for the oxygen flux in both domains, for the medium velocity, and for the oxygen uptake rate. Oxygen flux is expressed by Fick's law:[30]

$$N^{I}_{O_2,r} = -D^{I}_{O_2}\frac{\partial c^{I}_{O_2}}{\partial r}, \tag{B.5}$$

$$N^{II}_{O_2,r} = -D^{II}_{O_2}\frac{\partial c^{II}_{O_2}}{\partial r}, \tag{B.6}$$

where $D^{I}_{O_2}$ and $D^{II}_{O_2}$ are the diffusion coefficients of the oxygen, respectively, in domains I and II. The medium velocity is expressed by Poiseuille's equation consistent in the limit at low Reynolds number:

$$v_z\left(r,t\right) = \frac{2Q_{ch}}{\pi S(z,t)^2}\left[1-\left(\frac{r}{S\left(z,t\right)}\right)^2\right]. \tag{B.7}$$

The oxygen uptake rate was assumed to follow the Michaelis-Menten kinetics; it is proportional to the local oxygen concentration and to the specific cell volume:[15,18,31]

$$R_{O_2} = -\frac{1}{\tilde{v}_{cell}}\frac{Q_m c^{II}_{O_2}}{C_m + c^{II}_{O_2}} \tag{B.8}$$

In the above equations, $\tilde{v}_{cell}$ is the cell specific volume, Q_m is the maximal oxygen consumption rate, and C_m is the oxygen concentration at half-maximal oxygen consumption. Equations (B.3) and (B.4) were solved with respect to the variables $c^{I}_{O_2}$,

$c_{O_2}^{II}$. Boundary conditions required for eqs (B.3) and (B.4) are:

$$c_{O_2}^{I}(r,z,t) = c_{O_2,0} \qquad z = 0, \tag{B.9}$$

$$\frac{\partial c_{O_2}^{I}(r,z,t)}{\partial r} = 0 \qquad r = 0, \tag{B.10}$$

$$\frac{\partial c_{O_2}^{I} II(r,z,t)}{\partial r} = 0 \qquad r = R, \tag{B.11}$$

$$N_{O_2,r}^{I}(r,z,t) = N_{O_2,r}^{II}(r,z,t) \qquad r = S(z,t)\,. \tag{B.12}$$

$c_{O_2,0}$ is the dissolved oxygen concentration at the inlet of the channel, eqs (B.10) and (B.11) show, respectively, a symmetry and insulation condition in the center and at the wall of the channel, and eq (B.12) denotes that the molar fluxes at the interface are the same for both domains. Equations (B.13) and (B.14) are the initial condition of uniform value of the oxygen concentration ($c_{O_2,0}$) in both domains.

$$c_{O_2}^{I}(r,z,t) = c_{O_2,0} \qquad t = t_{in}, \tag{B.13}$$

$$c_{O_2}^{II}(r,z,t) = c_{O_2,0} \qquad t = t_{in}. \tag{B.14}$$

The size of domains I and II depends on the effective channel radius, $S(z,t)$, according to the cell growth. The solution of the mass balance eqs (B.3) and (B.4) requires an expression for effective channel radius as function of time and the axial coordinate for each channel. Assuming a constant specific cell volume, the cell volume balance equation follows:

$$\frac{d}{dt}\left[\delta V_{cell}(z,t)\right] = R_{cell}(z,t)\,, \tag{B.15}$$

δV_{cell} is the cell volume for a δz section, and R_{cell} is the cell growth rate. The cell volume, δV_{cell}, is defined as:

$$\delta V_{cell}(z,t) = 2\pi \int_{z}^{z+\delta z} \int_{S(z,t)}^{R} r\, dz dr. \tag{B.16}$$

The specific cell growth rate was simplified to a first-order kinetics, proportional to the local oxygen concentration and to the cell volume, which is similar to that used by others in the literature:[14,27,32,33]

$$R_{cell}\left(z,t\right) = k_{cell} F_{damp} c_{O_2}^{II} \delta V_{cell}, \tag{B.17}$$

k_{cell} is the cell growth kinetic constant, and F_{damp} is the damping function. It is worth mentioning that eq (B.17) is a fair linear approximation of Monod-type equation only for low oxygen concentration. To be consistent, we verified that the results of simulation show negligible difference when eq (B.17) or Monod-type equation[34] was used. The damping function takes into account the inhibition for low oxygen level and high shear stress. The cell growth rate decreases once the oxygen concentration approaches to the minimum oxygen concentration and/or when the effective channel radius approaches to the minimum value, which is determined by the maximum shear stress that cells can tolerate. It is defined as:

$$F = \frac{1}{\pi}\left\{\frac{\pi}{2} + \arctan\left[k_{damp}\left(c_{O_2}^{II} - c_{O_2}^{lim}\right)\left(S\left(z,t\right) - S^{lim}\right)\right]\right\}, \tag{B.18}$$

k_{damp} is the tunable damping coefficient, which determines the steepness of F variation from 1 to 0, $c_{O_2}^{lim}$ is the minimum threshold of oxygen concentration necessary for the cell growth, and S^{lim} is the effective channel radius below which the shear stress inhibits the cell growth or induces cell detachment at a rate equal to cell growth rate:[35]

$$S^{lim} = \left(\frac{4\mu Q_{ch}}{\pi \tau_{shear}}\right)^{1/3}, \tag{B.19}$$

τ_{shear} is the threshold shear stress, and Q_{ch} is the volumetric flow rate in the $k-th$ channel. Combining eqs (B.15)-(B.17), the rate of displacement of the effective channel radius, dS/dt, is obtained:

$$\frac{dS}{dt} = -\frac{k_{cell}}{S\left(z,t\right)} \int_{S(z,t)}^{R} F c_{O_2}^{II} r \, dr, \tag{B.20}$$

The initial condition of eq (B.20) is given by:

$$S\left(z,t\right) = S_0 \qquad t = t_{in}, \tag{B.21}$$

S_0 is the initial medium/cell interface position. The resolution of the system of eqs (B.3), (B.4), and (B.20) at the same time for each channel k, coupled with eqs (B.1) and (B.2), gives: the temporal evolution of the volumetric flow rate partitioning in all channels; the spatiotemporal evolution of the cell volume, the oxygen concentration, and the effective channel radius; and the shear stress on the cell layer for each channel of the Gaussian distribution. To analyze the model results, the average channel properties are defined. The average cell volume fraction $\langle\chi\rangle$ is defined as:

$$\langle\chi\rangle = \frac{1}{R^2}\frac{\displaystyle\int_0^{L_{ch}}\int_{S(z,t)}^{R} r\,dr dz}{\displaystyle\int_0^{L_{ch}}\int_0^{R} r\,dr dz}, \tag{B.22}$$

The average effective diameter is defined as:

$$\langle D\rangle = \frac{\displaystyle\int_0^{L_{ch}} 2S\,dz}{\displaystyle\int_0^{L_{ch}} dz}. \tag{B.23}$$

The average oxygen concentration at the outlet of the channel was evaluated by the following expression:

$$\langle c_{O_2}\rangle = \frac{\displaystyle\int_0^{S(t)} c^I_{O_2} r\,dr}{\displaystyle\int_0^{S(t)} r\,dr}. \tag{B.24}$$

Parameter Estimation. All model parameters are listed in Table B.1. The cell growth kinetic constant, k_{cell}, was evaluated by the cell doubling time of cells cultured in our laboratory (data not shown), the damping coefficient, k_{damp}, was set to have a sharp profile of the damping function (i.e., a quickly inhibition of the cell growth) without discontinuities, and the cell specific volume, $\tilde{v}_{cell}$, was determined measuring the size of cells cultured in our laboratory.

Numerical Solution. The model equations were rewritten in dimensionless

Table B.1: Model Parameters: Their Symbol, the Respective Values Used in Simulations, and the Reference

Parameter	Symbol	Value	Reference
cell growth kinetic constant	k_{cell}	$7.64 \times 10^{-5}\,\mathrm{m^3\,mol^{-1}\,s^{-1}}$	this work
cell specific volume	$\tilde{v}_{cell}$	$1.44 \times 10^{-15}\,\mathrm{m^3\,/cell}$	experimental evaluated
damping coefficient	k_{damp}	$10\,\mathrm{m^2\,/mol}$	this work
diffusion coefficient oxygen, cell	$D^{II}_{O_2}$	$2.0 \times 10^{-9}\,\mathrm{m^2\,/s}$	40
diffusion coefficient oxygen, medium	$D^{I}_{O_2}$	$3.29 \times 10^{-9}\,\mathrm{m^2\,/s}$	41
dissolved oxygen concentration in equilibrium with air	$c_{O_2,0}$	$2.1 \times 10^{-1}\,\mathrm{mol\,/m^3}$	42
maximal oxygen consumption rate	Q_m	$1.86 \times 10^{-18}\,\mathrm{mol\,cell^{-1}\,s^{-1}}$	31
medium viscosity	μ	$7.7 \times 10^{-4}\,\mathrm{Pa\,s}$	43
oxygen concentration at half-maximal oxygen consumption	C_m	$6 \times 10^{-3}\,\mathrm{mol\,/m^3}$	31
threshold oxygen concentration	$c^{lim}_{O_2}$	$5.26 \times 10^{-2}\,\mathrm{mol\,/m^3}$	44
threshold shear stress	τ_{shear}	$0.10\,\mathrm{Pa}$	45,46

form using the following scaling factors:

$$\tilde{r} = \frac{r}{R}; \quad \tilde{z} = \frac{z}{L_{ch}}; \quad \tilde{s}\left(\tilde{z}, \tau\right) = \frac{S\left(z, t\right)}{R}; \quad \tau = \frac{D^{I}_{O_2}}{L^2_{ch}} t, \tag{B.25}$$

$$c^{I}\left(\tilde{r}, \tilde{z}, tau\right) = \frac{c^{I}_{O_2}\left(r, z, t\right)}{c_{O_2,0}}; \quad c^{II}\left(\tilde{r}, \tilde{z}, tau\right) = \frac{c^{II}_{O_2}\left(r, z, t\right)}{c_{O_2,0}}. \tag{B.26}$$

Moving boundary conditions (eq (B.20)) have been solved by the front fixing method. The following coordinate transformations were applied in domains I and II, to solve this moving boundary problem:

$$\xi_I = \frac{\tilde{r}}{\tilde{s}\left(\tilde{z}, \tau\right)}, \tag{B.27}$$

$$\xi_{II} = \frac{\tilde{r} - 1}{\tilde{s}\left(\tilde{z}, \tau\right) - 1}. \tag{B.28}$$

In this way, both coordinates ξ_I and ξ_{II} range from 0 to 1. Dimensionless equations obtained from eqs (B.3), (B.4), and (B.20) were discretized using the finite volumes technique. The discretization of the mathematical model leads to an ordinary differential equation (ODE) system, which was numerically solved using MATLAB (The MathWorks, Natick, MA), and the function *ode15s* was utilized to compute the equations. Along the axial direction, a linear discretization was used, while in the radial direction, a geometrical discretization was used starting from the interface and applying the following expression:

$$\tilde{h}_{i+1} = 2^q \tilde{h}_i, \tag{B.29}$$

$$\tilde{h}_1 = \frac{(1 - 2^q)}{\left(1 - 2^{qN_r}\right)}. \tag{B.30}$$

In these two equations, $\tilde{h}_i$ is the dimensionless width of the mesh i, q is a discretization parameter equals to 0.5 in domains I and II, and N_r is the number of meshes; it is necessary to set the width of the first one utilizing eq (B.30). When the gradient of oxygen concentration is steep at the interface, a higher value of q can be chosen to better describe the oxygen profile. Optimal mesh size condition was achieved varying the number of mesh in both directions (radial and axial) until a difference less than 0.5% between the simulation's results was reached; we used 10 meshes in the z coordinate and 20 meshes in each domain in the r coordinate. The implementation of the moving boundary by means of the front fixing method was validated, and the numerical solution was compared to the analytical solution of the Stefan problem.[36] To check the mass conservativity of the model, several tests were done at every time step simulation and between the initial and the final time. The values of all numerical parameters are shown in Table B.2.

Table B.2: Parameters of the Numerical Solutions: Symbol and Respective Values

Parameter	Symbol	Value
discretization parameter	q	0.5
mesh in the z coordinate	N_z	10
mesh in the domain I	N_r^I	20
mesh in the domain II	N_r^{II}	20
absolute tolerance in *ode15s* function		1×10^{-7}

B.4 Results

The results are presented in two sections: (i) the spatiotemporal evolution of a single channel properties; and (ii) the temporal evolution of the averaged properties of every class of channel for a Gaussian distribution of channel diameters.

Spatiotemporal Evolution in a Single Channel. Figure B.2 shows the spatiotemporal evolution of the cell volume (domain II) as variation of the position of the domain I/II interface ($\tilde{s}$) and the oxygen concentration profiles (c) for a 300 µm diameter channel. The dimensionless effective diameter, $2\tilde{s}$, decreases from the initial condition of $\tilde{s}_0 = 0.91$, which is constant along the axial coordinate and corresponds to a thickness of domain II equal to 9% of the channel diameter. The model highlights different cell growth rates at different axial positions, resulting in the time-variation of the slope of the interfacial line in Figure B.2A. The cell domain at the channel inlet ($\tilde{z} = 0$) grows faster than at the channel outlet ($\tilde{z} = 1$). At the steady state, s reaches a uniform value along the z-direction equal to 0.30, which

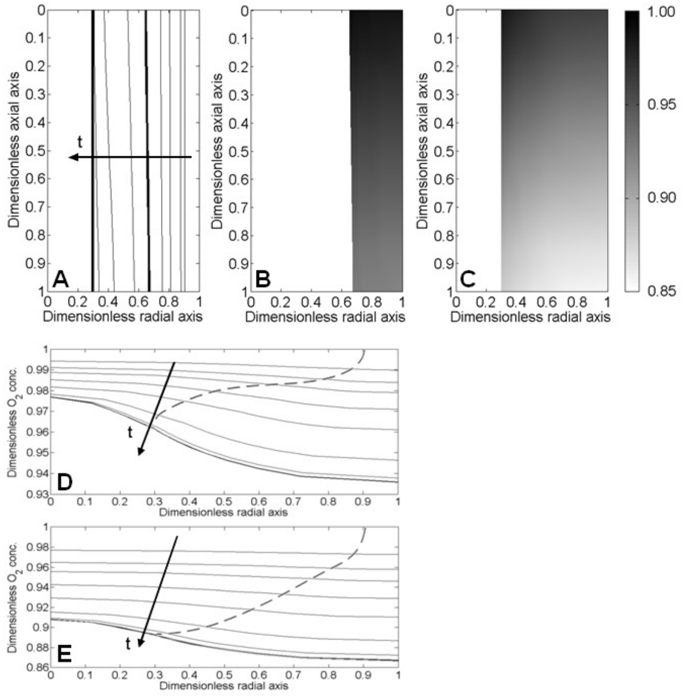

Figure B.2: Results obtained for a 300 µm diameter channel. (A) Position of domain I/II interface along the channel parametric in time. The thicker lines show the interface at $t = 1$ day and $t = t_{fin}$ (11 days), the same times reported in (B) and (C). (B,C) Color maps of oxygen concentration in domain II (cell domain) at $t = 1$ day (B) and at $t = t_{fin}$ (11 days, C); the legend on the right is the same for both figures. (D,E) Temporal evolution of the dimensionless oxygen concentration streamline along the radial axis at $\tilde{z} = 0.25$ (D) and at $\tilde{z} = 0.9$ (E). The dashed lines in both figures evidence the position of domain I/II interface. All of the values of the parameters and operative variables are illustrated in Tables B.1 and B.3.

Table B.3: Symbols and Values of the Operative Variable Used in Single-Channel and Multichannel Simulations

Single channel			Multichannel		
Operative variables	*Symbol*	*Value*	*Operative variables*	*Symbol*	*Value*
volumetric flow rate	Q_{ch}	$1.0 \times 10^{-11}\,\mathrm{m}^3/\mathrm{s}$	volumetric flow rate	Q_{tot}	$1.67 \times 10^{-8}\,\mathrm{m}^3/\mathrm{s}$
final time	t_{fin}	11 days	final time	t_{fin}	11 days
channel length	L	$3.0 \times 10^{-3}\,\mathrm{m}$	channel length	L	$3.0 \times 10^{-3}\,\mathrm{m}$
channel diameter	D	$3.0 \times 10^{-4}\,\mathrm{m}$	number of channel simulated	N_D	77
			variance	σ^2	$2.5 \times 10^{-9}\,\mathrm{m}^2$
			mean diameter	D_{mean}	$2.78 \times 10^{-4}\,\mathrm{m}$

corresponds to a cell thickness of 0.70. The color maps (Figure B.2B and C) represent the dimensionless oxygen concentration within the domain II, respectively, after 1 and 11 days. c^{II} is higher near the inlet of the channel, and it decreases along the axial and radial coordinates; c^{II} decreases more as domain II is thicker. In the case reported, after 1 day the cell thickness is different between the inlet and the outlet section and the minimum dimensionless oxygen value is about 0.95, while, after 11 days, the cell thickness is uniform and equals 0.70, and the lower oxygen value is about 0.85. Figures B.2D and E shows the time evolution of the radial profiles of oxygen concentration for $\tilde{z} = 0.25$ and $\tilde{z} = 0.9$, respectively. The dashed line in Figures B.2D and E denotes the position of domain interface at different time for the two z-sections. The oxygen consumption by the cells in the domain II reduces the oxygen concentration inside it. The thicker cell domain means lower concentrations not only in the cell domain but also in the center of the channel. Figures B.2D and E show how the oxygen concentration decreases with time during cell volume growth. Moreover, at the outlet of the channel (Figure B.2E), the concentration is lower than at the inlet (Figure B.2D), and the different shape of the dashed lines underlines the difference in cell volume growth as observed in Figures B.2A-C. In the case reported, the oxygen concentration is always much higher than the critical value of 0.25, which means the factor limiting the cell growth is the shear stress. Analogue simulations were carried out modifying the flow rate by 10% for a two-channel diameter (300 and 150 µm)(data not shown). A change in the flow rate value influences the cell volume fraction at stationary: reducing the flow rate by 10%, the s value increments of 3.5%, while increasing the flow rate by 10%, s decreases by 3.2%. The homogeneity and the duration of the transitory state are not affected by this operative variable. On the other hand, a decrement of the channel diameter led to a reduction of both the duration of the transitory and the final cell volume fraction. Simulation for 300 and 150 µm gave a uniform cell volume fraction at steady state. In any case, the oxygen concentration did not reach the critical value of 0.25, and the factor limiting the cell growth was the shear stress. Understanding the results of a single channel is the basis to comprehending the more complex data given by simulation of a 3D scaffold with a Gaussian distribution of the channel diameters.

Temporal Evolution for a Gaussian Channel Distribution. Typical examples of the outputs that can be obtained using this model are shown in Figures B.3 and B.4. In this particular case, a scaffold characterized by a Gaussian distribution of channel diameters with mean diameter and variance equal, respectively, to 2.8×10^{-4} and $2.5 \times 10^{-9}\,\mathrm{m}^{2}$,[37] was considered. Figure B.3 shows the temporal evolution of the distribution of the channel effective diameters and the flow rate per channel. In particular, the probability function of the effective channel diameter ($2\tilde{s}$) (Figure B.3A) has an initial symmetric Gaussian shape (thick dashed line

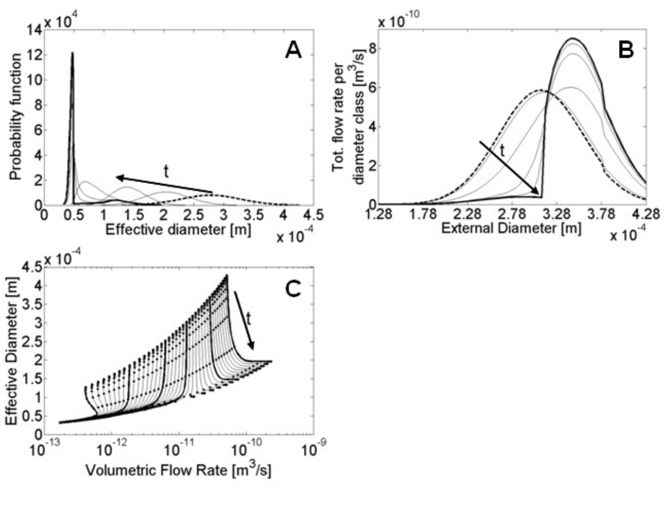

Figure B.3: Temporal evolution of effective channel diameters and volumetric flow rates in a multichannel scaffold. (A) Probability function of the effective diameters at different time points. Thicker dashed line is the initial distribution, and the thicker solid line is the final distribution. (B) Evolution of the volumetric flow rate distribution per each channel. Thicker dashed line corresponds to the initial distribution, and the thicker solid line is the final distribution. (C) Temporal evolution of the effective channel diameter versus the volumetric flow rate of that channel. Each line corresponds to a class of channel defined by the external diameter; the top part of the figure denotes the initial condition, while the bottom one denotes the condition at the final time; the points on the lines indicate time steps of 12 h. All of the values of the parameters and operative variables are summarized in Tables B.1 and B.3.

centered in 2.78×10^{-4} m) that becomes narrower, then log-normal, and finally it becomes similar to a bimodal distribution (thick line on the left). The intermediate values of diameter approach zero probability after 7 days. At the end of the simulated 11 days, the bimodal distribution has one high peak at 4.7×10^{-5} m and a second smaller and larger peak centered at 1.2×10^{-4} m. Likewise, for the channel diameter distribution, it is also possible to analyze the temporal evolution of the distribution of the total volumetric flow rate between the different channels (Figure B.3B). The initial distribution (thick dashed line on the left) is not symmetric because the flow rate is related to the diameter through a four power law (Fanning equation). The discontinuity that can be seen for a diameter of 3.8×10^{-4} m in each profile is due to a change of diameter sampling. In the channels with the external diameter smaller than 3.1×10^{-4} m, the medium flow rate decreases in time, and it comes closer to zero, while above this threshold value the flow rate increases. The presence of this threshold value is visible also in Figure B.3C, which summarizes the information of the previous two plots. Here, the effective diameters versus the relative channel flow rate are reported at different time. Each line refers to a class of channels defined by the value of the external diameter ($2R$). For the first 4 days, the flow rates are constant in almost all of the classes, while the effective diameters decrease; after that the curves follow two trends: for a first group of channels, the effective diameter approaches to a unique value (about 4.7×10^{-5} m) as discussed above for Figure B.3A, and the flow rates come closer to zero, as shown in Figure B.3B. While for a second group of channels, the effective diameters remain higher (they create the second distribution of the final channel diameter distribution centered at 1.2×10^{-4} m, as discussed above for Figure B.3A) and the volume flow rates increase, as seen in Figure B.3B. The threshold between these two groups is the external diameter equal to 3.1×10^{-4} m. Figure B.4 reports data of the average cell volume fraction for each channel (Figure B.4A), the uniformity of cell growth along the z-direction for every channels (Figure B.4B), the shear stress on the cells at the channel inlet (Figure B.4C), and the oxygen concentration at each channel outlet (Figure B.4D). In this simulated case, the model shows that the cell volume fraction increases in every channel up to a value higher than 0.8 (Figure B.4A). The cell volume grows at the same rate in all of the channels up to a cell volume fraction of about 0.45 (the points on the line indicate time step of 12 h), after that in

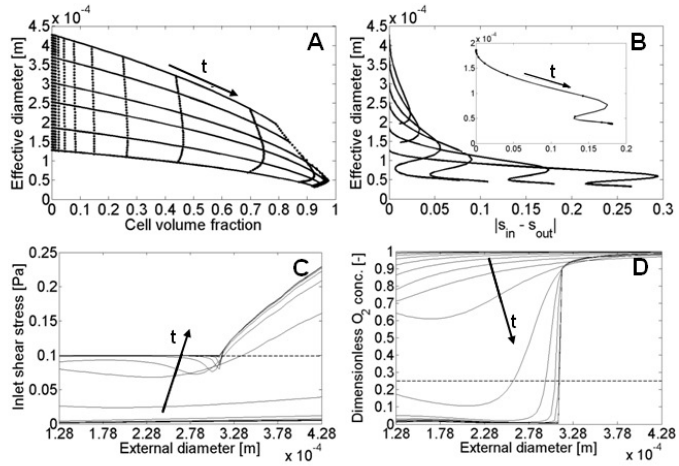

Figure B.4: Outputs of a simulation of a multichannel scaffold. The temporal evolution of the effective diameter of different classes of channels is reported versus the cell volume fraction in that channel (A) or versus the absolute value of the difference between S at the inlet and at the outlet of every channel (B). Each line corresponds to a class of channel defined by the external diameter; the left side corresponds to the initial Gaussian distribution, and the points on the lines indicate time steps of 12 h. Inset in (B) shows the temporal evolution of the effective diameter for a channel with small diameter value. Shear stress evaluated at the inlet of the channels as a function of the external channel diameter and parametric in time; the dashed line shows the threshold shear stress value above which it inhibits cell growth (0.1 Pa) (C). Dimensionless oxygen concentration evaluated at the outlet of the channels versus the external diameter and parametric in time; the dashed line indicates the minimum dimensionless oxygen concentration necessary for cell growth (5.26×10^{-2} mol/m^3) (D).

the channels with external diameters around 2.5×10^{-4} m the growth rate becomes higher; the stationary state is reached earlier and at lower final cell volume fraction in the larger channels. Figure B.4A shows once more how the effective diameters of the smaller channels approach to the same value. The effective diameters in Figure B.4A, such as in Figure B.3, are the average value along the z-direction. Figure B.4B shows the variance of the s value along the z-direction in each channel, which is the heterogeneity along this direction. In this graph, the effective average diameter is reported versus the absolute value of the difference of s at the inlet and at the outlet of each channel. The difference between the inlet and the outlet increases at the beginning, with the inlet value lower than the outlet one. This difference reaches a maximum and then decreases. In the larger channels, the difference reaches almost the zero value at the stationary state; in the smaller channels (e.g., inset in Figure B.4B) after a decreasing phase, the difference starts to increase again up to 0.25 at the end of the culture in the smallest channel. The shear stress on the cells was evaluated at the inlet of the channels, because this is the zone where the s is always the minimum of the channel, and thus the shear stress reaches the higher values. The data parametric in time are reported in Figure B.4C. The shear stress depends on the flow rate distribution, its value increases with time, and it goes over shear stress limit (dashed line at 0.1 Pa) only in the channels with external diameter greater than 3.10×10^{-4} m. The shear stress is one factor that can limit cell growth; the other one we considered is the oxygen concentration. Figure B.4D reports the temporal evolution of the oxygen concentration at the outlet of each channel as a function of the external channel diameter. Starting from the initial value (eqs (B.13) and (B.14)), the oxygen concentration decreases with time. The decrement is almost negligible in channels greater than 3.10×10^{-4} m, while in the smaller channel the oxygen concentration goes below the minimum oxygen concentration necessary for the cell growth (dashed line at 0.25 of dimensionless oxygen concentration), reaching values close to zero. It is worth observing that these results are quite insensitive to the model parameters. For instance, a 100% variation of the cell growth kinetic constant k_{cell} or the maximal oxygen consumption rate Q_m induces a change in the mean cell volume fraction of about 4% and 1%, respectively, without modifying the general trend. Simulations were performed modifying the two most important operative variables: the distribution of channel diameters and the total volumetric flow rate. Figure B.5 shows the time evolution of the cell volume fraction for four different scaffold geometry. Figure B.5A refers to the case of scaffolds with equal channels of the diameter of 2.78×10^{-4} m, while the other graphs are related to scaffolds with a Gaussian distribution of the channel diameters with the mean value equal to 2.78×10^{-4} m and increasing variance value (1.56×10^{-10} m^2 (Figure B.5B), 6.25×10^{-10} m^2 (Figure B.5C), 2.5×10^{-09} m^2 (Figure B.5D)). The case of Figure B.5D is the same as in Figures B.3 and B.4. The four graphs show a similar cell growth rate until the fourth day of culture (highlighted points); after that only in Figure B.5D the smaller channels are not anymore the ones with the highest cell volume fraction. In Figure B.5B and C, the cell volume growth is uniform over a longer period of time, and the larger channels never have a higher cell volume fraction than the smaller ones. At the steady-state condition (inset in each graph), the mean cell volume fraction does not have sensible difference (Table B.4), but the difference

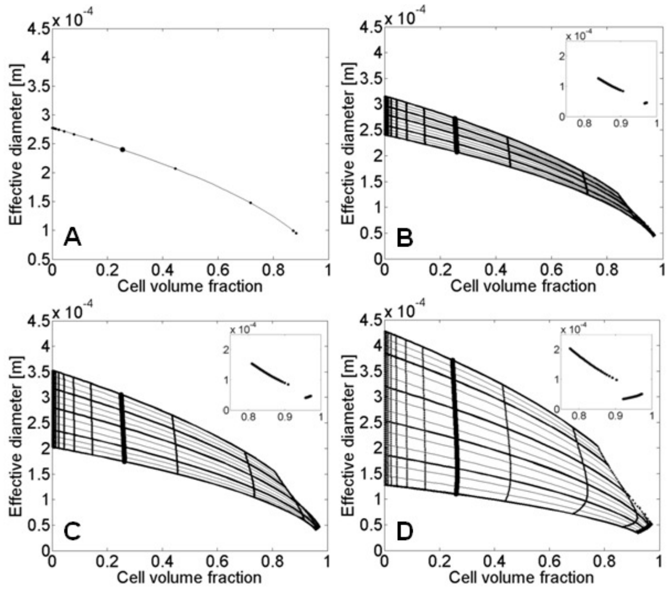

Figure B.5: Effect of the channel diameter distribution on the cell growth. In the four cases, the channel diameter distributions have the same mean value (Table B.3), but different variance: $0\,\mathrm{m}^2$ (A), $1.56 \times 10^{-10}\,\mathrm{m}^2$ (B), $6.25 \times 10^{-10}\,\mathrm{m}^2$ (C), and $2.5 \times 10^{-09}\,\mathrm{m}^2$ (D). The smaller points on the lines indicate time steps of 12 h; the highlighted points denote the cell volume fraction in channels after 4 days of culture. The magnifications at the top right in each figure represent the cell volume fraction profile at the final time.

between the highest and the lowest cell volume is enhanced, increasing the variance value of the Gaussian distribution. The investigation of the effects of a change in the total volumetric flow rate led to Table B.5 and Figure B.6 where the time evolution of the cell volume fraction is reported in the cases of $1.67 \times 10^{-10}\,\mathrm{m}^3/\mathrm{s}$ (Figure B.6A), $1.67 \times 10^{-09}\,\mathrm{m}^3/\mathrm{s}$ (Figure B.6B), $1.67 \times 10^{-08}\,\mathrm{m}^3/\mathrm{s}$ (Figure B.6C), and $1.67 \times 10^{-07}\,\mathrm{m}^3/\mathrm{s}$ (Figure B.6D). In Figure B.6A, the growth of cell volume fraction is slower than the other cases and reaches the lowest mean value at the

Table B.4: Mean, Lowest, and Highest Cell Volume Fraction Obtained from Simulations of 11 Days of Culture Using Different Variance Values of the Gaussian Distribution of Channel Diameters

Variance	Mean cell volume fraction	Lowest cell volume fraction	Highest cell volume fraction
$0\,\mathrm{m}^2$	0.88	0.88	0.88
$1.56 \times 10^{-10}\,\mathrm{m}^2$	0.91	0.84	0.97
$6.25 \times 10^{-10}\,\mathrm{m}^2$	0.92	0.81	0.97
$2.5 \times 10^{-09}\,\mathrm{m}^2$	0.93	0.78	0.97

Table B.5: Mean, Lowest, and Highest Cell Volume Fraction Obtained from Simulations of 11 Days of Culture Using Different Values of Total Volumetric Flow Rate

Total volumetric	Mean cell flow rate	Lowest cell volume fraction	Highest cell volume fraction
$1.67 \times 10^{-10}\,\mathrm{m}^3/\mathrm{s}$	0.88	0.88	0.88
$1.67 \times 10^{-09}\,\mathrm{m}^3/\mathrm{s}$	0.91	0.84	0.97
$1.67 \times 10^{-08}\,\mathrm{m}^3/\mathrm{s}$	0.92	0.81	0.97
$1.67 \times 10^{-07}\,\mathrm{m}^3/\mathrm{s}$	0.93	0.78	0.97

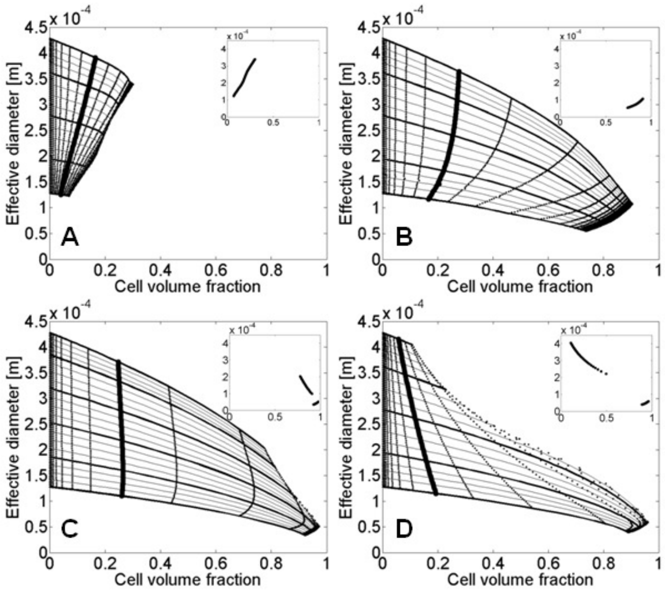

Figure B.6: Effect of the total volumetric flow rate on the cell growth. The figures are shown with an increasing flow rate value: $1.67 \times 10^{-10}\,\mathrm{m}^3/\mathrm{s}$ (A), $1.67 \times 10^{-09}\,\mathrm{m}^3/\mathrm{s}$ (B), $1.67 \times 10^{-08}\,\mathrm{m}^3/\mathrm{s}$ (C), and $1.67 \times 10^{-07}\,\mathrm{m}^3/\mathrm{s}$ (D). The smaller points on the lines indicate time steps of 12 h; the highlighted points denote the cell volume fraction in channels after 4 days of culture. The magnifications at the top right in each figure represent the cell volume fraction profile at the final time.

final time. Higher mean value is reached in the second considered case, and Figure B.6B shows a good uniformity between the different class of channel diameters. A discontinuity between cell volume values in the smaller and larger channels can be observed using 1 ml/min (Figure B.6C) and is highlighted by a further increase in the flow rate. A flow rate of 10 ml/min leads to a final mean cell volume fraction of 0.705, which is lower than both cases B and C; furthermore, the heterogeneity is the highest observed.

B.5 Discussion

In this work, we focused on the mathematical description of the cell growth inside a 3D porous scaffold that is perfused by the culture media. In particular, we developed a mathematical model that can be a useful tool for an a priori estimation of the time variation of the cell volume fraction and its degree of heterogeneity in a scaffold with a known distribution of pore diameters. It is known that the properties of the cell microenvironment influence the cell metabolic regime and therefore the cell growth rate.[4,6] To ensure the uniformity of 3D culture condition, the microenvironmental properties should be measured and controlled; however, techniques for experimentally monitoring these properties are still missing. Mathematical models can help to overcome these difficulties, simulating the time variation of the properties of the cell microenvironment and evaluating their degree of heterogeneity. We developed a model that allows the prediction of the cell volume growth within pores of different diameters, showing the heterogeneity of the cell volume fraction not only between different pores (Figure B.4A) but also between different axial positions for a single pore (Figures B.2A and B.4B). The results obtained from a simulation of a single channel (Figure B.2) can be compared to available literature. In particular, our data, in agreement with previous work,[26] show a gradient of oxygen concentration along both directions parallel and perpendicular to the medium flow with a profile that changes with time as the cells grow. Moreover, our model considers a cell growth inhibition due to chemical and/or mechanical stimuli, that is, the oxygen concentration and the shear stress imposed on the cell layer. Our model predicts the heterogeneity of cell volume fraction because it takes into account the existing correlations between the macroscopic operative variables and the microenvironment fluid dynamics and transport regimes, and between these regimes and the cell metabolism. In particular, the medium flow rate and the pore diameters of the scaffold are two important operative variables easy to monitor and control. They influence the oxygen transport and the shear stress at microscopic level, which thereby are known to affect the cell growth of many cell types. To our knowledge, the previous mathematical models of 3D cell culture did not discuss the heterogeneity sources of the cell microenvironment properties. Moreover, they either neglected the cell growth (steady-state condition model)[16,18,19] or they utilized averaged values of the properties of the scaffold such as the porosity or the pore diameters, without considering its geometrical heterogeneousness,[14,15,26] or they considered static culture with no medium convection.[14,17,25] The addition of the cell growth contribution allows the simulation of the time course of the cell volume fraction (CVF). This can lead to important observations such as the absence of influence of the variance of channel diameter on the average CVF and on the CVF homogeneity for a period of time lower than a critical value (96 h for the cases in Figure B.5). For some specific cell types, such as chondrocytes or osteocytes, it could be worth it to introduce in the balance a term describing the production of extracellular matrix that can occupy a relevant volume fraction. The scaffold geometry is an important parameter when looking into cell culture heterogeneity. Figure B.5 demonstrates that the larger is the distribution of the channel diameter, the higher is the difference in cell volume fraction at the stationary state, while the average cell volume fraction is almost invariant. This suggests the use of scaffolds with channels of a single diameter value, but this type of scaffold requires sophisticate and expensive technique for their production. Because the model is solved using dimensionless variables, the contribution of channel tortuosity can be simply considered by normalizing the axial coordinate by the effective channel length. Concerning scaffold geometry, one relevant improvement can be done by introducing a rational description of the interconnection between channels. The interconnectivity affects the homogeneity of medium composition by increasing it with increasing degree of interconnection. Our model can be considered as the limiting case of zero interconnectivity and thus maximum medium heterogeneity. By introducing the interconnection, the absolute value of heterogeneity will be modified, but the considerations done with this model when comparing different flow rate or channel diameter distribution will remain valid. The medium convection term is fundamental for simulating a perfusion system where the flow rate is the most important operative variable. Figure B.6 shows how drastically the choice of the flow rate can affect the result of a cell culture. For very low flow rate, the perfused system acts as a static culture where the oxygen transport is governed by diffusion, which provides enough oxygen only for an approximately 100 µm layer of cells. Within a 3D culture the diffusion is not sufficient to allow a relevant cell growth inside the scaffold because it is inhibited by the lacking of oxygen.[38] Our model shows how in the case of low flow rate for every channel diameter the inhibitory mechanism is the hypoxia (Figure B.6A), and there are no channels with high shear stress. Experimental data on dynamic culture refer that medium perfusion promotes the cell growth because it enhances oxygen transport, but an excessive increment of the flow rate induces high value of shear stress and then inhibition of cell growth or cell detachment.[39] The cell detachment can be compensated by the duplication of other cells resulting in a global null cell volume growth. In a complex 3D scaffold, it is hard to understand experimentally if the inhibitory mechanism is the same in the whole scaffold or if there are areas in hypoxic condition and others with too high shear stress. Data obtained with the model and reported in Figure B.6 not only confirm the experimental observation but allow also further considerations. An optimum flow rate for reaching the maximum mean CVF at the stationary state exists, but it may be not coincident with the optimum one at early time point or to the optimum for the point of view of the homogeneity. At the lower flow rate, the inhibitory phenomenon is always and in every channel not a sufficient oxygen transport (Figure B.6A and B), while by increasing the flow rate also the shear stress becomes a non negligible variable. This is a cause of heterogeneity because the growth of cell volume in the smallest channels is always governed by the oxygen transport, while in the largest channels the cells feel the effect of high values of shear stress (Figures B.4 and B.6C and D). The non homogeneity of CVF can be drastically evident as in the case shown in Figure B.6D. An a priori estimation of the optimal flow rate is important not only during the use of a bioreactor but also during the design and development of a dynamic culture system. The knowledge of the range of flow rate and the precision required is fundamental for a correct definition of the pumping, the tubing, and the control system characteristics, which thereby determine the cost of the dynamic culture equipment. The same principles applied to correlate fluid dynamics and transport regimes to oxygen concentration in the cell microenvironment can be used to involve other basic metabolites (i.e., glucose) for studying their influence on the metabolic regime. Moreover, the model is easily extendible to investigate also the heterogeneity of the cell regulatory regime, taking into account the concentration of endogenous and exogenous factors in the microenvironment.

B.6 Literature Cited

(1) Scadden, D. T. The stem-cell niche as an entity of action. *Nature* **2006**, *441*, 1075–79.

(2) Khetani, S. R.; Bhatia, S. N. Engineering tissues for *in vitro* applications. *Curr. Opin. Biotechnol.* **2006**, *17*, 524–531.

(3) Anon. Goodbye, flat biology? *Nature* **2003**, *424*, 861.

(4) Smalley, K. S. M.; Lioni, M.; Herlyn, M. Life isn't flat: Taking cancer biology to the next dimension. *In Vitro Cell. Dev. Biol.* **2006**, *42*, 242–247.

(5) O'Neill, A.; Schaffer, D. V. The biology and engineering of stem cell control. *Biotechnol. Appl. Biochem.* **2004**, *40*, 5–16.

(6) Li, L.; Xie, T. Stem cell niche: structure and function. *Annu. Rev. Cell Dev. Biol.* **2005**, *21*, 605–631.

(7) Patel, M.; Fisher, J. P. Biomaterial scaffolds in pediatric tissue engineering. *Pediatr. Res.* **2008**, *63*, 497–501.

(8) Eisenbarth, E. Biomaterials for tissue engineering. *Adv. Eng. Mater.* **2007**, *9*, 1051–1060.

(9) Martin, Y.; Vermette, P. Bioreactors for tissue mass culture: Design, characterization, and recent advances. *Biomaterials* **2005**, *26*, 7481–7503.

(10) Porter, B.; Zauel, R.; Stockman, H.; Guldberg, R.; Fyhrie, D. 3-D computational modeling of media flow through scaffolds in a perfusion bioreactor. *J. Biomechanics* **2005**, *38*, 7.

(11) Cimetta, E.; Flaibani, M.; Mella, M.; Serena, E.; Boldrin, L.; DeCoppi, P.; Elvassore, N. Enhancement of viability of muscle precursor cells on 3D scaffold in a perfusion bioreactor. *Int. J. Artif. Organs* **2007**, *30*, 415–428.

(12) King, J.; Miller, W. Bioreactor development for stem cell expansion and controlled differentiation. *Curr. Opin. Chem. Biol.* **2007**, *11*, 5.

(13) Sengers, B. G.; Taylor, M.; Please, C. P.; Oreffo, R. O. C. Computational modelling of cell spreading and tissue regeneration in porous scaffolds. *Biomaterials* **2007**, *28*, 1926–1940.

(14) Dunn, J. C. Y.; Chan, W.-Y.; Cristini, V.; Kim, J. S.; Lowengrub, J.; Singh, S.; Wu, B. M. Analysis of cell growth in three-dimensional scaffolds. *Tissue Eng.* **2006**, *12*, 705–716.

(15) Coletti, F.; Macchietto, S.; Elvassore, N. Mathematical modeling of three-dimensional cell cultures in perfusion bioreactors. *Ind. Eng. Chem. Res.* **2006**, *45*, 8158–8169.

(16) Dulong, J.-L.; Legallais, C. A theoretical study of oxygen transfer including cell necrosis for the design of a bioartificial pancreas. *Biotechnol. Bioeng.* **2007**, *96*, 990–998.

(17) Gross, J. D.; Constantinidis, I.; Sambanis, A. Modeling of encapsulated cell systems. *J. Theor.*

Biol. **2007**, *244*, 500–510.

(18) Radisic, M.; Malda, J.; Epping, E.; Geng, W.; Langer, R.; Vunjak-Novakovic, G. Oxygen gradients correlate with cell density and cell viabilityin engineered cardiac tissue. *Biotechnol. Bioeng.* **2006**, *93*, 332–343.

(19) Ye, H.; Das, D. B.; Triffitt, J. T.; Cui, Z. Modelling nutrient transport in hollow fibre membrane bioreactors for growing three-dimensional bone tissue. *J. Membr. Sci.* **2006**, *272*, 169–178.

(20) Cioffi, M.; Boschetti, F.; Raimondi, M. T.; Dubini, G. Modeling evaluation of the fluid-dynamic microenvironment in tissue-engineered constructs: A micro-CT based model. *Biotechnol. Bioeng.* **2006**, *93*, 500– 510.

(21) Sawyer, N.; Worrall, L.; Crowe, J.; Waters, S.; Shakesheff, K.; Rose, F.; Morgan, S. In situ monitoring of 3D *in vitro* cell aggregation using an optical imaging system. *Biotechnol. Bioeng.* **2008**, *100*, 159–167.

(22) Thelwall, P.; Neves, A.; Brindle, K. Measurement of bioreactor perfusion using dynamic contrast agent-enhanced magnetic resonance imaging. *Biotechnol. Bioeng.* **2001**, *75*, 682–690.

(23) Lee, K.-M.; Gilmore, D. F. Statistical experimental design for bioprocess modeling and optimization analysis: repeated-measures method for dynamic biotechnology process. *Appl. Biochem. Biotechnol.* **2006**, *135*, 101–115.

(24) Radisic, M.; Deen, W.; Langer, R.; Vunjak-Novakovic, G. Mathematical model of oxygen distribution in engineered cardiac tissue with parallel channel array perfused with culture medium containing oxygen carriers. *Am. J. Physiol. Heart Circ. Physiol.* **2005**, *288*, H1278–H1289.

(25) Galbusera, F.; Cioffi, M.; Raimondi, M. An in silico bioreactor for simulating laboratory experiments in tissue engineering. *Biomed. Microdevices* **2008**, *10*, 547–554.

(26) Galbusera, F.; Cioffi, M.; Raimondi, M.; Pietrabissa, R. Computational modeling of combined cell population dynamics and oxygen transport in engineered tissue subject to interstitial perfusion. *Comput. Methods Biomechanics Biomed. Eng.* **2007**, *10*, 279–287.

(27) Lewis, M.; MacArthur, B.; Malda, J.; Pettet, G.; Please, C. Heterogeneous proliferation within engineered cartilaginous tissue: the role of oxygen tension. *Biotechnol. Bioeng.* **2005**, *91*, 607–615.

(28) Mollet, M.; Godoy-Silva, R.; Berdugo, C.; Chalmers, J. Acute hydrodynamic forces and apoptosis: A complex question. *Biotechnol. Bioeng.* **2007**, *98*, 772–788.

(29) Hathcock, J.; Hall, C.; Turitto, V. Active tissue factor shed from human arterial smooth muscle cells adheres to artificial surfaces. *J. Biomater. Sci.* **2000**, *11*, 1211–1225.

(30) Bird, R.; Stewart, W.; Lightfoot, E. *Transport Phenomena*; John Wiley & Sons, Inc.: New

York, **2002**.

(31) Obradovic, B.; Meldon, J. H.; Freed, L. E.; Vunjak-Novakovic, G. Glycosaminoglycan deposition in engineered cartilage: Experiments and mathematical model. *AIChE J.* **2000**, *46*, 1860–1871.

(32) Galban, C. J.; Locke, B. R. Effects of spatial variation of cells and nutrient and product concentrations coupled with product inhibition on cell growth in a polymer scaffold. *Biotechnol. Bioeng.* **1999**, *64*, 633– 643.

(33) Galban, C. J.; Locke, B. R. Analysis of cell growth kinetics and substrate diffusion in a polymer scaffold. *Biotechnol. Bioeng.* **1999**, *65*, 121–132.

(34) Acevedo, C. A.; Weinstein-Oppenheimer, C.; Brown, D. I.; Huebner, H.; Buchholz, R.; Young, M. E. A mathematical model for the design of fibrin microcapsules with skin cells. *Bioprocess Biosyst. Eng.* **2009**, *32*, 341–351.

(35) Perry, R.; Green, D. *Perry's Chemical Engineers' Handbook*; McGraw-Hill: New York, **1997**.

(36) Crank, J. *Free and Moving Boundary*; Clarendon Press: Oxford, **1984**.

(37) van Lenthe, G. H.; Hagenmüller, H.; Bohner, M.; Hollister, S. J.; Meinel, L.; Müller, R. Nondestructive micro-computed tomography for biological imaging and quantification of scaffold-bone interaction *in vivo*. *Biomaterials* **2007**, *28*, 12.

(38) Freed, L. E.; Guilak, F.; Guo, X. E.; Gray, M. L.; Tranquillo, R.; Holmes, J. W.; Radisic, M.; Sefton, M. V.; Kaplan, D.; Vunjak-Novakovic, G. Advanced tools for tissue engineering: Scaffolds, bioreactors, and signaling. *Tissue Eng.* **2006**, *12*, 3285–3305.

(39) Tanaka, Y.; Yamato, M.; Okano, T.; Kitamori, T.; Sato, K. Evaluation of effects of shear stress on hepatocytes by a microchip-based system. *Meas. Sci. Technol.* **2006**, *17*, 4.

(40) MacPherson, J.; O'Hare, D.; Unwin, P.; Winlove, C. Quantitative spatially resolved measurements of mass transfer through laryngeal cartilage. *Biophys. J.* **1997**, *73*, 11.

(41) Chow, D.; Wenning, L.; Miller, W.; Papoutsakis, E. Modeling pO2 distributions in the bone marrow hematopoietic compartment. I. Krogh's model. *Biophys. J.* **2001**, *81*, 10.

(42) Zhao, F.; Pathi, P.; Grayson, W.; Xing, Q.; Locke, B. R.; Ma, T. Effects of oxygen transport on 3-D human mesenchymal stem cell metabolic activity in perfusion and static cultures: Experiments and mathematical model. *Biotechnol. Prog.* **2005**, *21*, 1269–1280.

(43) Moreira, J.; Santana, P.; Feliciano, A.; Cruz, P.; Racher, A.; Griffiths, J.; Carrondo, M. Effect of viscosity upon hydrodynamically controlled natural aggregates of animal cells grown in stirred vessels. *Biotechnol. Prog.* **1995**, *11*, 9.

(44) Mehta, G.; Mehta, K.; Sud, D.; Song, J. W.; Bersano-Begey, T.; Futai, N.; Heo, Y. S.; Mycek,

M.-A.; Linderman, J. J.; Takayama, S. Quantitative measurement and control of oxygen levels in microfluidic poly(dimethylsiloxane) bioreactors during cell culture. *Biomed. Microdevices* **2007**, *9*, 123–134.

(45) Keane, J.; Ryan, D.; Gray, P. Effect of shear stress on expression of a recombinant protein by Chinese hamster ovary cells. *Biotechnol. Bioeng.* **2002**, *81*, 10.

(46) Akimoto, S.; Mitsumata, M.; Sasaguri, T.; Yoshida, Y. Laminar shear stress inhibits vascular endothelial cell proliferation by inducing cyclindependent kinase inhibitor p21(Sdi1/Cip1/Waf1). *Circ. Res.* **2000**, *86*, 185–190.

Appendix C

Reduced insulin signaling pathways model

In this section the simplified insulin signaling pathways model obtained in chapter 5 from the original version [15] will be presented. All the details on the model reduction are described in chapter 5. The state variables with their description are reported in Tab. C.1.

Table C.1: State variables of the simplified insulin signaling pathways model.

Variable symbol	Description
Ins	Insulin input
Y_1	Concentration of unbound surface insulin receptors
Y_2	Concentration of phosphorylated twice-bound surface receptors
Y_3	Concentration of phosphorylated once-bound surface receptors
Y_4	Concentration of unbound unphosphorylated intracellular receptors
Y_5	Concentration of phosphorylated twice-bound intracellular receptors
Y_6	Concentration of phosphorylated once-bound intracellular receptors
Y_7	Concentration of tyrosine-phosphorylated IRS-1
Y_8	Concentration of tyrosine-phosphorylated IRS-1/activated PI 3-kinase complex
Y_9	Percentage of PI(3,4,5)P3 out of the total lipid population
Y_{10}	Percentage of PI(4,5)P2 out of the total lipid population
Y_{11}	Percentage of activated Akt
Y_{12}	Percentage of activated PKC-ζ
Y_{13}	Percentage of cell surface GLUT4
$C1$	Concentration of unphosphorylated once-bound surface receptors
$C2$	Concentration of unphosphorylated IRS-1
$C3$	Concentration of inactivated PI 3-kinase
$C4$	Percentage of PI(3,4)P2 out of the total lipid population
$C5$	Percentage of inactivated Akt
$C6$	Percentage of inactivated PKC-ζ
$C7$	Percentage of intracellular GLUT4

The differential equations implemented in the model (see chapter 5 and chapter 6) to describe the mass balance of each component are as follows:

$$dY_1/dt = k_{-1}C_1 + k_{-3}[PTP]Y_3 - k_1 InsY_1 + k_{-4}Y_4 - k_4Y_1, \tag{C.1}$$

$$dY_2/dt = k_2 InsY_3 - k_{-2}Y_2 + k_{-5}Y_5 - k_5Y_2, \tag{C.2}$$

$$dY_3/dt = k_3C_1 + k_{-2}Y_2 - k_2 InsY_3 - k_{-3}[PTP]Y_3 + k_{-5}Y_6 - k_5Y_3, \tag{C.3}$$

$$dY_4/dt = k_6[PTP]\left(Y_5 + Y_6\right) + k_4Y_1 - k_{-4}Y_4, \tag{C.4}$$

$$dY_5/dt = k_5Y_2 - k_{-5}Y_5 - k_6[PTP]Y_5, \tag{C.5}$$

$$dY_6/dt = k_5Y_3 - k_{-5}Y_6 - k_6[PTP]Y_6, \tag{C.6}$$

$$dY_7/dt = k_7C_2\left(Y_2 + Y_3\right)/IR_p + k_{-8}Y_8 - \left(k_{-7}[PTP] + k_8C_3\right)Y_7, \tag{C.7}$$

$$dY_8/dt = k_8C_3Y_7 - k_{-8}Y_8, \tag{C.8}$$

$$dY_9/dt = k_{9,1}Y_8Y_{10} + k_{9,2}Y_{10} + k_{10}C_4 - \left(k_{-9}[PTEN] + k_{-10}[SHIP]\right)Y_9, \tag{C.9}$$

$$dY_{10}/dt = k_{-9}[PTEN]Y_9 - \left(k_{9,1}Y_8Y_{10} + k_{9,2}Y_{10}\right), \tag{C.10}$$

$$dY_{11}/dt = k_{11,1}Y_9C_5 - k_{11,2}C_5 - k_{-11}Y_{11}, \tag{C.11}$$

$$dY_{12}/dt = k_{12,1}Y_9C_6 - k_{12,2}C_6 - k_{-12}Y_{12}, \tag{C.12}$$

$$dY_{13}/dt = \left(k_{13} + k_{14,1}Y_{11} + k_{14,2}Y_{12}\right)C_7 - k_{-13}Y_{13}. \tag{C.13}$$

Initial conditions are as follows, all the other state variables initial condition are equal to zero:

$$Y_1\left(t\right) = 9.0 \times 10^{-13}\,\mathrm{M} \qquad t = t_{in}, \tag{C.14}$$

$$Y_4\left(t\right) = 1.0 \times 10^{-13}\,\mathrm{M} \qquad t = t_{in}, \tag{C.15}$$

$$Y_9\left(t\right) = 0.31\,\% \qquad t = t_{in}, \tag{C.16}$$

$$Y_{10}\left(t\right) = 99.4\,\% \qquad t = t_{in}, \tag{C.17}$$

$$Y_{13}\left(t\right) = 4\,\% \qquad t = t_{in}. \tag{C.18}$$

The algebraic equations implemented in the model along with the ordinary differential equations are:

$$C_1 = IR_{tot} - \sum_{i=1}^{6} Y_i, \tag{C.19}$$

$$C_2 = IRS\text{-}1_{tot} - \left(Y_7 + Y_8\right), \tag{C.20}$$

$$C_3 = PI3\text{-}K_{tot} - Y_8, \tag{C.21}$$

$$C_4 = PIP_{tot} - \left(Y_9 + Y_{10}\right), \tag{C.22}$$

$$C_5 = Akt_{tot} - Y_{11}, \tag{C.23}$$

$$C_6 = PKC\text{-}\zeta_{tot} - Y_{12}, \tag{C.24}$$

$$C_7 = GLUT4_{tot} - Y_{13}. \tag{C.25}$$

The simplified model parameters are listed in Tab. C.2.

Table C.2: Kinetic parameters of the simplified insulin signaling pathways model.

Parameter symbol	Value
k_1	$1.0 \times 10^{6}\,\mathrm{M}^{-1}\,\mathrm{s}^{-1}$
k_{-1}	$3.33 \times 10^{-3}\,\mathrm{s}^{-1}$
k_2	$1.0 \times 10^{6}\,\mathrm{M}^{-1}\,\mathrm{s}^{-1}$
k_{-2}	$3.33 \times 10^{-1}\,\mathrm{s}^{-1}$
k_3	$4.17 \times 10^{1}\,\mathrm{s}^{-1}$
k_{-3}	$3.33 \times 10^{-3}\,\mathrm{s}^{-1}$
k_4	$5.56 \times 10^{-6}\,\mathrm{s}^{-1}$
k_{-4}	$5.0 \times 10^{-5}\,\mathrm{s}^{-1}$
k_5	$3.5 \times 10^{-5}\,\mathrm{s}^{-1}$
k_{-5}	$3.5 \times 10^{-6}\,\mathrm{s}^{-1}$
k_6	$7.68 \times 10^{-3}\,\mathrm{s}^{-1}$
k_7	$6.93 \times 10^{-2}\,\mathrm{s}^{-1}$
k_{-7}	$2.33 \times 10^{-2}\,\mathrm{s}^{-1}$
k_8	$1.18 \times 10^{10}\,\mathrm{s}^{-1}$
k_{-8}	$1.67 \times 10^{-1}\,\mathrm{s}^{-1}$
$k_{9,1}$	$4.20 \times 10^{12}\,\mathrm{M}^{-1}\,\mathrm{s}^{-1}$
$k_{9,2}$	$2.19 \times 10^{-3}\,\mathrm{s}^{-1}$
k_{-9}	$7.02 \times 10^{-1}\,\mathrm{s}^{-1}$
k_{10}	$4.94 \times 10^{-2}\,\mathrm{s}^{-1}$
k_{-10}	$4.62 \times 10^{-2}\,\mathrm{s}^{-1}$
$k_{11,1}$	$4.14 \times 10^{-3}\,\mathrm{M}^{-1}\,\mathrm{s}^{-1}$
$k_{11,2}$	$1.28 \times 10^{-3}\,\mathrm{s}^{-1}$
k_{-11}	$1.16 \times 10^{-1}\,\mathrm{s}^{-1}$
$k_{12,1}$	$4.14 \times 10^{-3}\,\mathrm{M}^{-1}\,\mathrm{s}^{-1}$
$k_{12,2}$	$1.28 \times 10^{-3}\,\mathrm{s}^{-1}$
k_{-12}	$1.16 \times 10^{-1}\,\mathrm{s}^{-1}$
k_{13}	$1.16 \times 10^{-4}\,\mathrm{s}^{-1}$
k_{-13}	$2.78 \times 10^{-3}\,\mathrm{s}^{-1}$
$k_{14,1}$	$3.83 \times 10^{-5}\,\mathrm{M}^{-1}\,\mathrm{s}^{-1}$
$k_{14,2}$	$1.53 \times 10^{-4}\,\mathrm{M}^{-1}\,\mathrm{s}^{-1}$

References

[1] R Langer and JP Vacanti. **Tissue Engineering**. *Science*, **260**(5110):920–926, May 1993. 3

[2] LG Griffith and G Naughton. **Tissue engineering - Current challenges and expanding opportunities**. *Science*, **295**(5557):1009–1014, February 2002. 3

[3] JA Burdick and G Vunjak-Novakovic. **Engineered microenvironments for controlled stem cell differentiation**. *Tissue Engineering Part A*, **15**(2):205–219, 2009. 3, 29, 46, 47

[4] M Radisic, LM Yang, J Boublik, RJ Cohen, R Langer, LE Freed, and G Vunjak-Novakovic. **Medium perfusion enables engineering of compact and contractile cardiac tissue**. *American Journal of Physiology-Heart and Circulatory Physiology*, **286**(2):H507–H516, February 2004. 4, 12

[5] M Radisic, J Malda, E Epping, W Geng, R Langer, and G Vunjak-Novakovic. **Oxygen gradients correlate with cell density and cell viability in engineered cardiac tissue**. *Biotechnology and Bioengineering*, **93**(2):332–343, 2006. 4, 6, 12, 52

[6] DA Lauffenburger and J Linderman. *Receptors: Models for Binding, Trafficking, and Signaling*. Oxford University Press, USA, January 1996. 4, 11

[7] RCP Kerckhoffs, SN Healy, TP Usyk, and AD McCulloch. **Computational methods for cardiac electromechanics**. *Proceedings of the IEEE*, **94**(4):769–783, April 2006. 5

[8] N Le Novere. **The long journey to a systems biology of neuronal function**. *BMC Systems Biology*, **1**, June 2007. 5

[9] M Meier-Schellersheim, IDC Fraser, and F Klauschen. **Multiscale modeling for biologists**. *Wiley Interdisciplinary Reviews-Systems Biology and Medicine*, **1**(1):4–14, August 2009. 5

[10] S Schnell, R Grima, and PK Maini. **Multiscale modeling in biology - New insights into cancer illustrate how mathematical tools are enhancing the understanding of life from the smallest scale to the grandest**. *American Scientist*, **95**(2):134–142, April 2007. 5, 11

[11] ZH Wang and TS Deisboeck. **Computational modeling of brain tumors: discrete, continuum or hybrid?** *Scientific Modeling and Simulations*, **15**(1-3):381–393, April 2008. 5

[12] GE Kapellos, TS Alexiou, and AC Payatakes. **A multiscale theoretical model for diffusive mass transfer in cellular biological media**. *Mathematical Biosciences*, **210**(1):177–237, November 2007. 5

[13] C Luni, JE Shoemaker, KR Sanft, LR Petzold, and FJ Doyle. **Confidence from uncertainty - A multi-target drug screening method from robust control theory**. *BMC Systems Biology*, **4**, November 2010. 6

[14] DS Wishart, R Yang, D Arndt, P Tang, and J Cruz. **Dynamic cellular automata: an alternative approach to cellular simulation**. *In Silico Biology*, **5**(2):139–161, 2005. PMID: 15972011. 6

[15] AR Sedaghat, A Sherman, and MJ Quon. **A mathematical model of metabolic insulin signaling pathways**. *American Journal of Physiology- Endocrinology And Metabolism*, **283**(5):E1084–E1101, 2002. 6, 70, 72, 75, 76, 77, 78, 79, 90, 97, 98, 157

[16] JJ Saucerman and AD McCulloch. **Mechanistic systems models of cell signaling networks: a case study of myocyte adrenergic regulation**. *Progress in Biophysics & Molecular Biology*, **85**(2-3):261–278, July 2004.

[17] F Posta and T Chou. **A mathematical model of intercellular signaling during epithelial wound healing**. *Journal of Theoretical Biology*, **266**(1):70–78, September 2010.

[18] R Cheong, A Hoffmann, and A Levchenko. **Understanding NF-κB signaling via mathematical modeling**. *Molecular Systems Biology*, **4**, May 2008.

[19] S Basak, H Kim, JD Kearns, V Tergaonkar, E O'Dea, SL Werner, CA Benedict, CF Ware, G Ghosh, IM Verma, and A Hoffmann. **A Fourth IκB Protein within the NF-κB Signaling Module**. *Cell*, **128**(2):369–381, January 2007. 6

[20] NJ Armstrong, KJ Painter, and JA Sherratt. **A continuum approach to modelling cell-cell adhesion**. *Journal of Theoretical Biology*, **243**(1):98–113, 2006. 6

[21] G Cheng, BB Youssef, P Markenscoff, and K Zygourakis. **Cell population dynamics modulate the rates of tissue growth processes**. *Biophysical Journal*, **90**(3):713–724, 2006. 6

[22] L Mancuso, M Scanu, M Pisu, A Concas, and G Cao. **Experimental analysis and modelling of *in vitro* HUVECs proliferation in the presence of various types of drugs**. *Cell Proliferation*, **43**(6):617–628, 2010.

[23] L Mancuso, MI Liuzzo, S Fadda, A Cincotti, M Pisu, A Concas, and G Cao. **Experimental analysis and modeling of bone marrow mesenchymal stem cells proliferation**. *Chemical Engineering Science*, **65**(1):562–568, 2010. 6

[24] KA Williams, S Saini, and TM Wick. **Computational fluid dynamics modeling of steady-state momentum and mass transport in a bioreactor for cartilage tissue engineering**. *Biotechnology progress*, **18**(5):951–963, October 2002. 6

[25] EA Botchwey, MA Dupree, SR Pollack, EM Levine, and CT Laurencin. **Tissue engineered bone: Measurement of nutrient transport in three-dimensional matrices**. *Journal of Biomedical Materials Research Part A*, **67A**(1):357–367, October 2003.

[26] RE McClelland, JM MacDonald, and RN Coger. **Modeling O_2 transport within engineered hepatic devices**. *Biotechnology and Bioengineering*, **82**(1):12–27, April 2003. PMID: 12569620.

[27] J Malda, J Rouwkema, DE Martens, EP le Comte, FK Kooy, J Tramper, CA van Blitterswijk, and J Riesle. **Oxygen gradients in tissue-engineered PEGT/PBT cartilaginous constructs: Measurement and modeling**. *Biotechnology and Bioengineering*, **86**(1):9–18, April 2004. 6, 20

[28] M Radisic, W Deen, R Langer, and G Vunjak-Novakovic. **Mathematical model of oxygen distribution in engineered cardiac tissue with parallel channel array**

perfused with culture medium containing oxygen carriers. *American Journal of Physiology-Heart and Circulatory Physiology*, **288**(3):H1278–H1289, March 2005. 20

[29] Diganta Bhusan Das. **Multiscale simulation of nutrient transport in hollow fibre membrane bioreactor for growing bone tissue: Sub-cellular scale and beyond**. *Chemical Engineering Science*, **62**(13):3627–3639, July 2007. 6

[30] D Nehring, P Adamietz, NM Meenen, and R Portner. **Perfusion cultures and modelling of oxygen uptake with three-dimensional chondrocyte pellets**. *Biotechnology Techniques*, **13**(10):701–706, October 1999. 6

[31] BG Sengers, HK Heywood, DA Lee, CWJ Oomens, and DL Bader. **Nutrient utilization by bovine articular chondrocytes: A combined experimental and theoretical approach**. *Journal of Biomechanical Engineering – Transactions of the ASME*, **127**(5):758–766, October 2005.

[32] DA Brown, WR MacLellan, H Laks, JCY Dunn, BM Wu, and RE Beygui. **Analysis of oxygen transport in a diffusion-limited model of engineered heart tissue**. *Biotechnology and Bioengineering*, **97**(4):962–975, 2007. 73

[33] M Pisu, N Lai, A Concas, and G Cao. **A Novel Simulation Model for Engineered Cartilage Growth in Static Systems**. *Tissue Engineering*, **12**(8):2311–2320, 2006. 6

[34] B Obradovic, JH Meldon, LE Freed, and G Vunjak-Novakovic. **Glycosaminoglycan deposition in engineered cartilage: Experiments and mathematical model**. *AIChE Journal*, **46**(9):1860–1871, September 2000. 6, 7, 52

[35] M Lappa. **Organic tissues in rotating bioreactors: fluid-mechanical aspects, dynamic growth models, and morphological evolution**. *Biotechnology and Bioengineering*, **84**(5):518–532, December 2003. 7, 13

[36] M Pisu, N Lai, A Cincotti, A Concas, and GC Cao. **Modeling of engineered cartilage growth in rotating bioreactors**. *Chemical Engineering Science*, **59**(22-23):5035–5040, December 2004. 7

[37] CYJ Ma, R Kumar, XY Xu, and A Mantalaris. **A combined fluid dynamics, mass transport and cell growth model for a three-dimensional perfused biorec-**

tor for tissue engineering of haematopoietic cells. *Biochemical Engineering Journal*, **35**(1):1–11, 2007.

[38] P. Yu, T. S Lee, Y. Zeng, and H. T Low. **Fluid dynamics and oxygen transport in a micro-bioreactor with a tissue engineering scaffold**. *International Journal of Heat and Mass Transfer*, **52**(1-2):316–327, 2009. 6

[39] MC Lewis, BD MacArthur, J Malda, G Pettet, and CP Please. **Heterogeneous proliferation within engineered cartilaginous tissue: the role of oxygen tension**. *Biotechnology and Bioengineering*, **91**(5):607–615, 2005. 6, 47, 53, 67

[40] Tristan I. Croll, Silke Gentz, Kilian Mueller, Malcolm Davidson, Andrea J. O'Connor, Geoffrey W. Stevens, and Justin J. Cooper-White. **Modelling oxygen diffusion and cell growth in a porous, vascularising scaffold for soft tissue engineering applications**. *Chemical Engineering Science*, **60**(17):4924–4934, September 2005. 6, 7

[41] M Flaibani, E Magrofuoco, and N Elvassore. **Computational Modeling of Cell Growth Heterogeneity in a Perfused 3D Scaffold**. *Industrial & Engineering Chemistry Research*, **49**(2):859–869, January 2010. 7, 66

[42] R Sacco, P Causin, P Zunino, and MT Raimondi. **A multiphysics/multiscale 2D numerical simulation of scaffold-based cartilage regeneration under interstitial perfusion in a bioreactor**. *Biomechanics and Modeling in Mechanobiology*, September 2010. PMID: 20865436.

[43] F Zhao, P Pathi, W Grayson, Q Xing, BR Locke, and T Ma. **Effects of oxygen transport on 3-D human mesenchymal stem cell metabolic activity in perfusion and static cultures: Experiments and mathematical model**. *Biotechnology progress*, **21**(4):1269–1280, August 2005.

[44] P Pathi, T Ma, and BR Locke. **Role of nutrient supply on cell growth in bioreactor design for tissue engineering of hematopoietic cells**. *Biotechnology and Bioengineering*, **89**(7):743–758, March 2005. 7, 37

[45] P Sucosky, DF Osorio, JB Brown, and GP Neitzel. **Fluid mechanics of a spinner-flask bioreactor**. *Biotechnology and Bioengineering*, **85**(1):34–46, January 2004. 7, 12

[46] B Bilgen, K Uygun, EM Bueno, P Sucosky, and GA Barabino. **Tissue growth modeling in a wavy-walled bioreactor**. *Tissue Engineering Part A*, **15**(4):761–771, 2008. 7, 12

[47] MT Raimondi, F Boschetti, L Falcone, GB Fiore, A Remuzzi, E Marinoni, M Marazzi, and R Pietrabissa. **Mechanobiology of engineered cartilage cultured under a quantified fluid-dynamic environment**. *Biomechanics and Modeling in Mechanobiology*, **1**(1):69–82, June 2002. PMID: 14586708. 7

[48] M Cioffi, J Kuffer, S Strobel, G Dubini, I Martin, and D Wendt. **Computational evaluation of oxygen and shear stress distributions in 3D perfusion culture systems: Macro-scale and micro-structured models**. *Journal of Biomechanics*, **41**(14):2918–2925, October 2008. 7, 12

[49] CJ Galban and BR Locke. **Analysis of cell growth in a polymer scaffold using a moving boundary approach**. *Biotechnology and Bioengineering*, **56**(4):422–432, November 1997. 7

[50] CJ Galban and BR Locke. **Effects of spatial variation of cells and nutrient and product concentrations coupled with product inhibition on cell growth in a polymer scaffold**. *Biotechnology and Bioengineering*, **64**(6):633–643, September 1999. 53

[51] CJ Galban and BR Locke. **Analysis of cell growth kinetics and substrate diffusion in a polymer scaffold**. *Biotechnology and Bioengineering*, **65**(2):121–132, October 1999. 53

[52] G Lemon and JR King. **Multiphase modelling of cell behaviour on artificial scaffolds: effects of nutrient depletion and spatially nonuniform porosity**. *Mathematical Medicine and Biology*, **24**(1):57–83, March 2007. 7

[53] BG Sengers, CWJ Oomens, and FPT Baaijens. **An integrated finite-element approach to mechanics, transport and biosynthesis in tissue engineering**. *Journal of Biomechanical Engineering – Transactions of the ASME*, **126**(1):82–91, February 2004. 7

[54] BG Sengers, CWJ Oomens, TQD Nguyen, and DL Bader. **Computational modeling to predict the temporal regulation of chondrocyte metabolism in response**

to various dynamic compression regimens. *Biomechanics and Modeling in Mechanobiology*, **5**(2-3):111–122, June 2006. 7

[55] International Diabetes Federation. *IDF Diabetes Atlas.* Brussels, Belgium: International Diabetes Federation, 3rd edition, 2007. 8

[56] S Colagiuri and K Borch-Johnsen. **Detect-2: early detection of type 2 diabetes and IGT**. *Diabetes Voice*, **48**(4):11–13, December 2003. 8

[57] ES Allman and JA Rhodes. *Mathematical Models in Biology: An Introduction.* Cambridge University Press, 1 edition, October 2003. 11

[58] DC Chow, LA Wenning, WM Miller, and ET Papoutsakis. **Modeling pO2 distributions in the bone marrow hematopoietic compartment. I. Krogh's model**. *Biophysical journal*, **81**(2):675–684, 2001. 11, 74

[59] I Martin, D Wendt, and M Heberer. **The role of bioreactors in tissue engineering**. *Trends in Biotechnology*, **22**(2):80–86, February 2004. 12, 13, 29

[60] CE Holy, MS Shoichet, and JE Davies. **Engineering three-dimensional bone tissue *in vitro* using biodegradable scaffolds: Investigating initial cell-seeding density and culture period**. *Journal of Biomedical Materials Research*, **51**(3):376–382, September 2000. 12

[61] BS Kim, AJ Putnam, TJ Kulik, and DJ Mooney. **Optimizing seeding and culture methods to engineer smooth muscle tissue on biodegradable polymer matrices**. *Biotechnology and Bioengineering*, **57**(1):46–54, January 1998. 12, 13

[62] A Bruinink, D Siragusano, G Ettel, T Brandsberg, F Brandsberg, M Petitmermet, B Muller, J Mayer, and E Wintermantel. **The stiffness of bone marrow cell-knit composites is increased during mechanical load**. *Biomaterials*, **22**(23):3169–3178, December 2001.

[63] Y Li, T Ma, DA Kniss, LC Lasky, and ST Yang. **Effects of filtration seeding on cell density, spatial distribution, and proliferation in nonwoven fibrous matrices**. *Biotechnology progress*, **17**(5):935–944, October 2001. 12

[64] YL Xiao, J Riesle, and CA Van Blitterswijk. **Static and dynamic fibroblast seeding and cultivation in porous PEO/PBT scaffolds**. *Journal of Materials Science-Materials in Medicine*, **10**(12):773–777, December 1999. 12

[65] KJL Burg, M Delnomdedieu, RJ Beiler, CR Culberson, KG Greene, CR Halberstadt, WD Holder, AB Loebsack, WD Roland, and GA Johnson. **Application of magnetic resonance microscopy to tissue engineering: A polylactide model**. *Journal of Biomedical Materials Research*, **61**(3):380–390, September 2002. 12, 13

[66] G Vunjak-Novakovic, LE Freed, RJ Biron, and R Langer. **Effects of mixing on the composition and morphology of tissue-engineered cartilage**. *AIChE Journal*, **42**(3):850–860, March 1996. 12

[67] M. W. Glacken, R. J. Fleischaker, and A. J. Sinskey. **Mammalian cell culture: engineering principles and scale-up**. *Trends in Biotechnology*, **1**(4):102–108, September 1983. 12

[68] SNO Williams, RM Callies, and KM Brindle. **Mapping of oxygen tension and cell distribution in a hollow-fiber bioreactor using magnetic resonance imaging**. *Biotechnology and Bioengineering*, **56**(1):56–61, October 1997. 12, 13

[69] Y Martin and P Vermette. **Bioreactors for tissue mass culture: Design, characterization, and recent advances**. *Biomaterials*, **26**(35):7481–7503, December 2005. 12, 29

[70] RL Carrier, M Papadaki, M Rupnick, FJ Schoen, N Bursac, R Langer, LE Freed, and G Vunjak-Novakovic. **Cardiac tissue engineering: Cell seeding, cultivation parameters, and tissue construct characterization**. *Biotechnology and Bioengineering*, **64**(5):580–589, September 1999. 13

[71] G. Vunjak-Novakovic, B. Obradovic, I. Martin, P. M Bursac, R. Langer, and L. E Freed. **Dynamic cell seeding of polymer scaffolds for cartilage tissue engineering**. *Biotechnology progress*, **14**(2):193–202, 1998. 13

[72] BR Unsworth and PI Lelkes. **Growing tissues in microgravity**. *Nature Medicine*, **4**(8):901–907, August 1998. 13

[73] R P Schwarz, T J Goodwin, and D A Wolf. **Cell culture for three-dimensional modeling in rotating-wall vessels: an application of simulated microgravity**. *Journal of Tissue Culture Methods*, **14**(2):51–57, 1992. PMID: 11541102.

[74] CM Begley and SJ Kleis. **The fluid dynamic and shear environment in the NASA/JSC rotating-wall perfused-vessel bioreactor**. *Biotechnology and Bioengineering*, **70**(1):32–40, October 2000. 13

[75] D Wendt, A Marsano, M Jakob, M Heberer, and I Martin. **Oscillating perfusion of cell suspensions through three-dimensional scaffolds enhances cell seeding efficiency and uniformity**. *Biotechnology and Bioengineering*, **84**(2):205–214, October 2003. 13

[76] M Flaibani, C Luni, E Sbalchiero, and N Elvassore. **Flow Cytometric Cell Cycle Analysis of Muscle Precursor Cells Cultured Within 3D Scaffolds in a Perfusion Bioreactor**. *Biotechnology Progress*, **25**(1):286–295, February 2009. 14, 64

[77] M. Fröhlich, W. L Grayson, D. Marolt, J. M Gimble, N. Kregar-Velikonja, and G. Vunjak-Novakovic. **Bone grafts engineered from human adipose-derived stem cells in perfusion bioreactor culture**. *Tissue Engineering Part A*, **16**(1):179–189, January 2010.

[78] A. M Sailon, A. C Allori, E. H Davidson, D. D Reformat, R. J Allen Jr, and S. M Warren. **A novel flow-perfusion bioreactor supports 3D dynamic cell culture**. *J Biomed Biotechnol*, **2009**:873816, 2009. 14

[79] D Yaffe and O Saxel. **Serial passaging and differentiation of myogenic cells isolated from dystrophic mouse muscle**. *Nature*, **270**(5639):725–727, December 1977. 14

[80] G Mehta, K Mehta, D Sud, JW Song, T Bersano-Begey, N Futai, YS Heo, MA Mycek, JJ Linderman, and S Takayama. **Quantitative measurement and control of oxygen levels in microfluidic poly(dimethylsiloxane) bioreactors during cell culture**. *Biomedical Microdevices*, **9**(2):123–134, April 2007. 20

[81] SHG Khoo and M Al-Rubeai. **Metabolomics as a complementary tool in cell culture**. *Biotechnology and Applied Biochemistry*, **47**(2):71, 2007. 20

[82] EA Ottesen, JW Hong, SR Quake, and JR Leadbetter. **Microfluidic digital PCR enables multigene analysis of individual environmental bacteria**. *Science*, **314**(5804):1464–1467, December 2006. 29

[83] LF Kang, BG Chung, R Langer, and A Khademhosseini. **Microfluidics for drug discovery and development: From target selection to product lifecycle management**. *Drug Discovery Today*, **13**(1-2):1–13, January 2008. 29

[84] PS Dittrich and A Manz. **Lab-on-a-chip: microfluidics in drug discovery**. *Nature Reviews Drug Discovery*, **5**(3):210–218, March 2006. 29

[85] DG Spiller, CD Wood, DA Rand, and MRH White. **Measurement of single-cell dynamics**. *Nature*, **465**(7299):736–745, June 2010. 29

[86] E Cimetta, E Figallo, C Cannizzaro, N Elvassore, and G Vunjak-Novakovic. **Micro-bioreactor arrays for controlling cellular environments: Design principles for human embryonic stem cell applications**. *Methods*, **47**(2):81–89, February 2009. 29, 30

[87] KR King, S Wang, D Irimia, A Jayaraman, M Toner, and ML Yarmush. **A high-throughput microfluidic real-time gene expression living cell array**. *Lab on a Chip*, **7**(1):77, 2007. 30

[88] JH Sung and ML Shuler. ***In vitro* microscale systems for systematic drug toxicity study**. *Bioprocess and Biosystems Engineering*, **33**(1):5–19, 2009. 30

[89] TM Squires, RJ Messinger, and SR Manalis. **Making it stick: convection, reaction and diffusion in surface-based biosensors**. *Nature Biotechnology*, **26**(4):417–426, 2008. 30

[90] E Figallo, C Cannizzaro, S Gerecht, JA Burdick, R Langer, N Elvassore, and G Vunjak-Novakovic. **Micro-bioreactor array for controlling cellular microenvironments**. *Lab on a Chip*, **7**(6):710–719, June 2007. 30, 31, 32, 41, 43

[91] E Cimetta, C Cannizzaro, R James, T Biechele, RT Moon, N Elvassore, and G Vunjak-Novakovic. **Microfluidic device generating stable concentration gradients for long term cell culture: application to Wnt3a regulation of beta-catenin signaling**. *Lab on a Chip*, **10**(23):3277–3283, 2010. 30

[92] R Gómez-Sjöberg, AA Leyrat, DM Pirone, CS Chen, and SR Quake. **Versatile, Fully Automated, Microfluidic Cell Culture System**. *Analytical Chemistry*, **79**(22):8557–8563, November 2007. 30, 31, 32, 43

[93] E Cimetta, M Flaibani, M Mella, E Serena, L Boldrin, P De Coppi, and N Elvassore. **Enhancement of viability of muscle precursor cells on 3D scaffold in a perfusion bioreactor**. *International Journal of Artificial Organs*, **30**(5):415–428, May 2007. 35, 36

[94] J Brandrup, EH Immergut, and EA Grulke. *Polymer Handbook, 2 Volumes Set*. Wiley-Interscience, 4 edition, May 2003. 36

[95] DM Cochran, D Fukumura, M Ancukiewicz, P Carmeliet, and RK Jain. **Evolution of Oxygen and Glucose Concentration Profiles in a Tissue-Mimetic Culture System of Embryonic Stem Cells**. *Annals of Biomedical Engineering*, **34**(8):1247–1258, 2006. 36

[96] GT Oehrtman, HS Wiley, and DA Lauffenburger. **Escape of autocrine ligands into extracellular medium: Experimental test of theoretical model predictions**. *Biotechnology and Bioengineering*, **57**(5):571–582, March 1998. 36

[97] HS Wiley, SY Shvartsman, and DA Lauffenburger. **Computational modeling of the EGF-receptor system: a paradigm for systems biology**. *Trends in Cell Biology*, **13**(1):43–50, January 2003.

[98] K Mehta and JJ Linderman. **Model-based analysis and design of a microchannel reactor for tissue engineering**. *Biotechnology and Bioengineering*, **94**(3):596–609, 2006. 36

[99] CA Acevedo, C Weinstein-Oppenheimer, DI Brown, H Huebner, R Buchholz, and ME Young. **A mathematical model for the design of fibrin microcapsules with skin cells**. *Bioprocess and Biosystems Engineering*, **32**(3):341–351, 2009. 37, 76

[100] L Li and T Xie. **Stem cell niche: structure and function**. *Annual Review of Cell and Developmental Biology*, **21**(1):605–631, 2005. 42, 67

[101] DT Scadden. **The stem-cell niche as an entity of action**. *Nature*, **441**(7097):1075–1079, 2006. 46, 69

[102] SR Khetani and SN Bhatia. **Engineering tissues for *in vitro* applications**. *Current Opinion in Biotechnology*, **17**(5):524–531, 2006. 46

[103] **Goodbye, flat biology?** *Nature*, **424**(6951):861, 2003.

[104] KSM Smalley, M Lioni, and M Herlyn. **Life isn't flat: Taking cancer biology to the next dimension**. *IN VITRO CELLULAR & DEVELOPMENTAL BIOLOGY-ANIMAL*, **42**(8-9):242–247, October 2006. 46, 67

[105] A O'Neill and DV Schaffer. **The biology and engineering of stem-cell control**. *Biotechnology and Applied Biochemistry*, **40**(1):5–16, 2004. 46

[106] E Eisenbarth. **Biomaterials for Tissue Engineering**. *Advanced Engineering Materials*, **9**(12):1051–1060, 2007. 46

[107] WL Grayson, S Bhumiratana, C Cannizzaro, PHG Chao, DP Lennon, AI Caplan, and G Vunjak-Novakovic. **Effects of Initial Seeding Density and Fluid Perfusion Rate on Formation of Tissue-Engineered Bone**. *Tissue Engineering Part A*, **14**(11):1809–1820, 2008. 47

[108] RB Bird, WE Stewart, and EN Lightfoot. *Transport Phenomena, Revised 2nd Edition*. John Wiley & Sons, Inc., 2nd edition, December 2006. 52, 74

[109] F Coletti, S Macchietto, and N Elvassore. **Mathematical Modeling of Three-Dimensional Cell Cultures in Perfusion Bioreactors**. *Industrial & Engineering Chemistry Research*, **45**(24):8158–8169, 2006. 52

[110] JCY Dunn, WY Chan, V Cristini, JS Kim, J Lowengrub, S Singh, and BM Wu. **Analysis of cell growth in three-dimensional scaffolds**. *Tissue Engineering*, **12**(4):705–716, April 2006. 53

[111] J Crank. *Free and Moving Boundary Problems*. Oxford University Press, USA, February 1987. 54, 55

[112] GH van Lenthe, H Hagenmuller, M Bohner, SJ Hollister, L Meinel, and R Muller. **Nondestructive micro-computed tomography for biological imaging and quantification of scaffold-bone interaction *in vivo***. *Biomaterials*, **28**(15):2479–2490, May 2007. 58

[113] A Carraro, M Flaibani, U Cillo, L Michelotto, E Magrofuoco, M Buggio, G Abatangelo, R Cortivo, MB Herrera, C Tetta, N Elvassore, and B Zavan. **A Combining Method to Enhance the *In Vitro* Differentiation of Hepatic Precursor Cells**. *Tissue Engineering Part C – Methods*, **16**(6):1543–1551, December 2010. 64

[114] DL Kaplan, RT Moon, and G Vunjak-Novakovic. **It takes a village to grow a tissue**. *Nature Biotechnology*, **23**(10):1237–1239, October 2005. 70

[115] S Zhang. **Beyond the Petri dish**. *Nature Biotechnology*, **22**(2):151–152, February 2004. 70

[116] S Wanant and MJ Quon. **Insulin receptor binding kinetics: Modeling and simulation studies**. *Journal Of Theoretical Biology*, **205**(3):355–364, August 2000. 70

[117] L Schäffer. **A model for insulin binding to the insulin-receptor**. *European Journal of Biochemistry*, **221**(3):1127–1132, May 1994.

[118] VV Kiselyov, S Versteyhe, L Gauguin, and P De Meyts. **Harmonic oscillator model of the insulin and IGF1 receptors' allosteric binding and activation**. *Molecular Systems Biology*, **5**, 2009. 70, 90

[119] R Heinrich, BG Neel, and TA Rapoport. **Mathematical models of protein kinase signal transduction**. *Molecular Cell*, **9**(5):957–970, May 2002. 70

[120] L Bardwell, X Zou, Q Nie, and NL Komarova. **Mathematical models of specificity in cell signaling**. *Biophysical Journal*, **92**(10):3425–3441, May 2007. PMID: 17325015. 70

[121] GD Holman, LL Leggio, and SW Cushman. **Insulin-stimulated GLUT4 glucose transporter recycling. A problem in membrane protein subcellular trafficking through multiple pools**. *Journal of Biological Chemistry*, **269**(26):17516–17524, July 1994. 70

[122] L Giri, VK Mutalik, and KV Venkatesh. **A steady state analysis indicates that negative feedback regulation of PTP1B by Akt elicits bistability in insulin-stimulated GLUT4 translocation**. *Theoretical Biology & Medical Modelling*, **1**, August 2004. 70

[123] BN Kholodenko, GC Brown, and JB Hoek. **Diffusion control of protein phosphorylation in signal transduction pathways**. *Biochemical Journal*, **350**:901–907, September 2000. 70

[124] N Borisov, E Aksamitiene, A Kiyatkin, S Legewie, J Berkhout, T Maiwald, NP Kaimachnikov, J Timmer, JB Hoek, and BN Kholodenko. **Systems-level interactions between insulin-EGF networks amplify mitogenic signaling**. *Molecular Systems Biology*, **5**, April 2009. 70, 90

[125] R Zielinski, PF Przytycki, J Zheng, D Zhang, TM Przytycka, and J Capala. **The crosstalk between EGF, IGF, and Insulin cell signaling pathways- computational and experimental analysis**. *BMC Systems Biology*, **3**(1), 2009. 70

[126] Y. H Chew, Y. L Shia, C. T Lee, F. A.A Majid, L. S Chua, M. R Sarmidi, and R. A Aziz. **Modeling of glucose regulation and insulin-signaling pathways**. *Molecular and cellular endocrinology*, **303**(1-2):13–24, 2009. 70

[127] W Liu, CC Hsin, and F Tang. **A molecular mathematical model of glucose mobilization and uptake**. *Mathematical Biosciences*, **221**(2):121–129, 2009. 70, 74

[128] BC Martin, JH Warram, AS Krolewski, RN Bergman, JS Soeldner, and CR Kahn. **Role of glucose and insulin resistance in development of type 2 diabetes mellitus: results of a 25-year follow-up study**. *The Lancet*, **340**(8825):925–929, October 1992. 71, 93

[129] C Bouche, S Serdy, CR Kahn, and AB Goldfine. **The cellular fate of glucose and its relevance in type 2 diabetes**. *Endocrine Reviews*, **25**(5):807–830, October 2004. 71

[130] FW Murray. **On the Computation of Saturation Vapor Pressure**. *Journal of Applied Meteorology*, **6**(1):203–204, 1967. 73

[131] E Morsiani, M Brogli, D Galavotti, T Bellini, B Ricci, P Pazzi, and TC Puviani. **Long-term expression of highly differentiated functions by isolated porcine hepatocytes perfused in a radial-flow bioreactor**. *Artificial Organs*, **25**(9):740–748, September 2001. 73

[132] JM Olefsky. **The effects of spontaneous obesity on insulin binding, glucose transport, and glucose oxidation of isolated rat adipocytes**. *Journal of Clinical Investigation*, **57**(4):842–851, 1976. 74, 96

[133] LE Flynn, GD Prestwich, JL Semple, and KA Woodhouse. **Proliferation and differentiation of adipose-derived stem cells on naturally derived scaffolds**. *Biomaterials*, **29**(12):1862–1871, 2008. 77

[134] BN Kholodenko, OV Demin, G Moehren, and JB Hoek. **Quantification of short term signaling by the epidermal growth factor receptor**. *Journal of Biological Chemistry*, **274**(42):30169–30181, 1999. 78

[135] G Cedersund, J Roll, E Ulfhielm, A Danielsson, H Tidefelt, and P Strålfors. **Model-Based Hypothesis Testing of Key Mechanisms in Initial Phase of Insulin Signaling**. *PLoS Computational Biology*, **4**(6):e1000096, 2008. 90

[136] Håkan K. R. Karlsson and Juleen R. Zierath. **Insulin signaling and glucose transport in insulin resistant human skeletal muscle**. *Cell Biochemistry and Biophysics*, **48**(2-3):103–113, 2007. 92

[137] D LeRoith. **Beta-cell dysfunction and insulin resistance in type 2 diabetes: Role of metabolic and genetic abnormalities**. *American Journal of Medicine*, **113**:3S–11S, October 2002. 92

[138] RA DeFronzo. **The triumvirate: beta-cell, muscle, liver. A collusion responsible for NIDDM**. *Diabetes*, **37**(6):667–687, June 1988.

[139] P Cohen. **Timeline - The twentieth century struggle to decipher insulin signalling**. *Nature Reviews Molecular Cell Biology*, **7**(11):867–873, November 2006.

[140] SI Taylor. **Deconstructing type 2 diabetes**. *Cell*, **97**(1):9–12, April 1999. 92

[141] C Weyer, RL Hanson, PA Tataranni, C Bogardus, and RE Pratley. **A high fasting plasma insulin concentration predicts type 2 diabetes independent of insulin resistance - Evidence for a pathogenic role of relative hyperinsulinemia**. *Diabetes*, **49**(12):2094–2101, December 2000. 92

[142] C Weyer, PA Tataranni, C Bogardus, and RE Pratley. **Insulin Resistance and Insulin Secretory Dysfunction Are Independent Predictors of Worsening of Glucose Tolerance During Each Stage of Type 2 Diabetes Development**. *Diabetes Care*, **24**(1):89 –94, January 2001.

[143] GM Reaven, CB Hollenbeck, and YDI Chen. **Relationship between glucose tolerance, insulin secretion, and insulin action in non-obese individuals with varying degrees of glucose tolerance**. *Diabetologia*, **32**(1):52–55, January 1989. 92

[144] R A Sicree, P Z Zimmet, H O King, and J S Coventry. **Plasma insulin response among Nauruans. Prediction of deterioration in glucose tolerance over 6 yr**. *Diabetes*, **36**(2):179–186, February 1987. PMID: 3542644. 93

[145] SE Kahn. **Clinical review 135 - The importance of beta-cell failure in the development and progression of type 2 diabetes**. *Journal of Clinical Endocrinology & Metabolism*, **86**(9):4047–4058, September 2001.

[146] RN Bergman, DT Finegood, and SE Kahn. **The evolution of beta-cell dysfunction and insulin resistance in type 2 diabetes**. *European Journal of Clinical Investigation*, **32**:35–45, June 2002. 93

[147] S O'Rahilly, JS Wainscoat, and RC Turner. **Type 2 (non-insulin-dependent) diabetes mellitus. New genetics for old nightmares**. *Diabetologia*, **31**(7):407–414, July 1988. 93

[148] AH Barnett, C Eff, RD Leslie, and DA Pyke. **Diabetes in identical twins. A study of 200 pairs**. *Diabetologia*, **20**(2):87–93, 1981. 93

[149] SP Helmrich, DR Ragland, RW Leung, and RS Paffenbarger. **Physical activity and reduced occurrence of non-insulin-dependent diabetes mellitus**. *The New England Journal of Medicine*, **325**(3):147–152, July 1991. PMID: 2052059. 93

[150] JS Flier. **The adipocyte: storage depot or node on the energy information superhighway?** *Cell*, **80**(1):15–18, January 1995. 103

[151] V Mohamed-Ali, JH Pinkney, and SW Coppack. **Adipose tissue as an endocrine and paracrine organ**. *International Journal of Obesity*, **22**(12):1145–1158, December 1998. 103

[152] JK Sethi and GS Hotamisligil. **The role of TNFα in adipocyte metabolism**. *Seminars in Cell & Developmental Biology*, **10**(1):19–29, February 1999. 104

[153] JJ Nolan, B Ludvik, P Beerdsen, M Joyce, and J Olefsky. **Improvement in Glucose Tolerance and Insulin Resistance in Obese Subjects Treated with Troglitazone**. *New England Journal of Medicine*, **331**(18):1188–1193, November 1994. 104

[154] GS Hotamisligil, P Arner, JF Caro, RL Atkinson, and BM Spiegelman. **Increased Adipose Tissue Expression of Tumor Necrosis Factor-alpha in Human Obesity and Insulin Resistance**. *Journal of Clinical Investigation*, **95**(5):2409–2415, May 1995. 104

[155] GS Hotamisligil, NS Shargill, and BM Spiegelman. **Adipose expression of tumor necrosis factor-α: direct role in obesity-linked insulin resistance**. *Science*, **259**(5091):87–91, January 1993.

[156] SM Grundy, HB Brewer, JI Cleeman, SC Smith, and C Lenfant. **Definition of metabolic syndrome - Report of the National Heart, Lung, and Blood Institute/American Heart Association Conference on Scientific Issues Related to Definition**. *Circulation*, **109**(3):433–438, January 2004.

[157] B Zinman, AJG Hanley, SB Harris, J Kwan, and IG Fantus. **Circulating tumor necrosis factor-alpha concentrations in a native Canadian population with hgh rates of type 2 diabetes mellitus**. *Journal of Clinical Endocrinology & Metabolism*, **84**(1):272–278, January 1999.

[158] PA Kern, M Saghizadeh, JM Ong, RJ Bosch, R Deem, and RB Simsolo. **The expression of tumor necrosis factor in human adipose tissue – Regulation by obesity, weight-loss, and relationship to lipoprotein-lipase**. *Journal of Clinical Investigation*, **95**(5):2111–2119, May 1995. 104

[159] GS Hotamisligil, DL Murray, LN Choy, and BM Spiegelman. **Tumor necrosis factor α inhibits signaling from the insulin receptor**. *PROCEEDINGS of the National Academy of Sciences of the United States of America*, **91**(11):4854–4858, May 1994. 104

[160] H Kanety, R Feinstein, MZ Papa, R Hemi, and A Karasik. **Tumor necrosis factor α-induced phosphorylation of insulin receptor substrate-1 (IRS-1). Possi-**

ble mechanism for suppression of insulin-stimulated tyrosine phosphorylation of IRS-1. *Journal of Biological Chemistry*, **270**(40):23780–23784, October 1995. 104

[161] GS Hotamisligil, P Peraldi, A Budavari, R Ellis, MF White, and BM Spiegelman. **IRS-1-mediated inhibition of insulin receptor tyrosine kinase activity in TNF-alpha- and obesity-induced insulin resistance**. *Science*, **271**(5249):665–668, February 1996. 104

[162] R Feinstein, H Kanety, MZ Papa, B Lunenfeld, and A Karasik. **Tumor Necrosis Factor-α Suppresses Insulin-induced Tyrosine Phosphorylation of Insulin Receptor and Its Substrates**. *Journal of Biological Chemistry*, **268**(35):26055–26058, December 1993. 104

[163] LS Liu, M Spelleken, K Röhrig, H Hauner, and J Eckel. **Tumor necrosis factor-α acutely inhibits insulin signaling in human adipocytes - Implication of the p80 tumor necrosis factor receptor**. *Diabetes*, **47**(4):515–522, April 1998. 104